

# **Numerical Study of Repair Strategies for Earthquake-Damaged CFST Bridge Columns**

by

**James Bumstead**

BS, Civil Engineering, University of Pittsburgh, 2017

Submitted to the Graduate Faculty of  
the University of Pittsburgh in partial fulfillment  
of the requirements for the degree of  
Master of Science in Civil Engineering

University of Pittsburgh

2019

UNIVERSITY OF PITTSBURGH  
SWANSON SCHOOL OF ENGINEERING

This thesis was presented

by

**James Robert Bumstead**

It was defended on

November 15, 2019

and approved by

Dr. Julie Vandebossche, Ph.D., Professor, Department of Civil and Environmental Engineering

Dr. Lev Khazanovich, Ph.D., Professor, Department of Civil and Environmental Engineering

Dr. Max Stephens, Ph.D., Assistant Professor, Department of Civil and Environmental  
Engineering

Thesis Advisor: Dr. Max Stephens, Ph.D., Assistant Professor, Department of Civil and  
Environmental Engineering

Copyright © by James Robert Bumstead

2019

# **Numerical Study of Repair Strategies for Earthquake-Damaged CFST Bridge Columns**

James Robert Bumstead, M.S.

University of Pittsburgh, 2019

Concrete filled steel tubes (CFSTs) provide a unique, economical alternative to traditional reinforced concrete (RC) columns in highway bridges for their ease of construction and efficient structural properties. The steel tube provides optimal flexural resistance and continuous confinement to the infill concrete, while the concrete fill improves stiffness and strength of the column, and prevents inward local tube buckling of the steel tube. Recent research has developed a practical and structurally robust, column-to-foundation/cap-beam connection for use in mid-to-high seismic regions. This connection, referred to as the embedded ring (ER) connection, is a full-strength connection, where well-detailed, ER CFST columns exhibit local, outward tube buckling directly above the foundation/cap-beam when subjected to reverse-cyclic, lateral loadings. This typical ductile failure mode is readily identifiable post-earthquake events, and is uniquely advantageous compared to typical RC columns due to limited concrete spalling and the availability of the steel tube for welded connections.

The main objective of this research was to develop practical repair strategies for ER CFST columns which exhibit this ductile failure progression, with the goal of reestablishing the original column strength and stiffness. Two strategies were developed: (1) a traditional plastic hinge relocation method that utilizes an enlarged, CFST pedestal that surrounds the damaged region, and (2) a performance-based repair that implements external energy dissipators and column-rocking to limit damage. A non-linear, numerical analysis approach was adopted to assess the hysteretic response of these repair methods in comparison to that of an undamaged, CFST column. Results

indicated that both repair strategies successfully restored lost stiffness and strength, specifically peak strength values of  $1.26M_p$  and  $1.02M_p$  for the traditional and performance-based methods were observed, respectively, where  $M_p$  represents the plastic moment of the original column. Additionally, a limited experimental study was carried out on the proposed, buckling restrained, energy dissipator where, under cyclic-compressive loadings, compressive yielding ( $1.12F_y$ ) and inelastic strains ( $9.0\varepsilon_y$ ) were measured within the laterally-restrained, structural fuse of the dissipator.

## Table of Contents

<b>1.0 Introduction.....</b>	<b>1</b>
<b>1.1 Motivation for Research .....</b>	<b>1</b>
<b>1.2 Research Objective.....</b>	<b>2</b>
<b>1.2.1 Proposed Repair Strategies .....</b>	<b>2</b>
<b>1.3 Report Outline .....</b>	<b>4</b>
<b>2.0 Literature Review .....</b>	<b>6</b>
<b>2.1 CFST Column to Foundation/Cap-Beam Connections.....</b>	<b>6</b>
<b>2.1.1 Exposed CFST Connections .....</b>	<b>7</b>
<b>2.1.2 Embedded CFST Connections .....</b>	<b>8</b>
<b>2.1.3 The Embedded Ring (ER) Connection .....</b>	<b>10</b>
<b>2.2 Plastic Hinge Relocation Repairs .....</b>	<b>13</b>
<b>2.2.1 Fiber Reinforced Polymer (FRP) Wraps .....</b>	<b>14</b>
<b>2.2.2 Section Enlargement .....</b>	<b>17</b>
<b>2.3 Performance Based Repair Strategies .....</b>	<b>19</b>
<b>2.3.1 Available Energy Dissipators for Implementation in Bridge Structures .....</b>	<b>20</b>
<b>2.3.2 Column-Rocking and Self-Centering Techniques.....</b>	<b>22</b>
<b>2.3.3 Dissipative Controlled Rocking (DCR) Columns .....</b>	<b>24</b>
<b>3.0 Analytical Modeling of CFST Columns Under Seismic Loadings .....</b>	<b>28</b>
<b>3.1 Numerical Model Overview.....</b>	<b>28</b>
<b>3.1.1 Non-linear Material Properties and Interaction Definitions.....</b>	<b>31</b>
<b>3.2 Numerical Validation with Reference Specimen .....</b>	<b>35</b>

3.2.1 Modeling Initial Earthquake Damage .....	39
<b>4.0 Plastic Hinge Relocation Repair Strategy.....</b>	<b>40</b>
4.1 Repair Overview .....	40
4.1.1 Performance Objectives .....	42
4.2 Design Procedure .....	42
4.2.1 Estimating Flexural Demand and Pedestal Height .....	43
4.2.2 Estimating Flexural Capacity of the Repair Pedestal .....	45
4.3 Numerical Model .....	48
4.3.1 Parametric Analysis of the FTMs .....	50
4.4 Analytical Results .....	53
<b>5.0 Performance-Based Repair Strategy.....</b>	<b>67</b>
5.1 Performance-Based Repair Strategy Overview.....	67
5.2 Design of the Performance-Based Repair .....	69
5.3 Buckling Restrained Reinforcing Bar (BRBar).....	72
5.3.1 Subcomponent Design of the BRBar .....	74
5.4 Experimental Program for the BRBar Subcomponent .....	76
5.4.1 Fabrication of Specimens and Experimental Setup .....	77
5.4.2 Results and Discussion .....	81
5.4.3 General Comments and Recommendation .....	91
5.5 Numerical Modeling of Performance-Based Repair .....	92
5.5.1 BRBar Model .....	94
5.6 Results and Discussion of the Global Repair Response .....	96
<b>6.0 Summary, Conclusions and Future Work.....</b>	<b>109</b>

<b>6.1 Plastic Hinge Relocation Repair Findings.....</b>	<b>110</b>
<b>6.2 Performance-Based Repair Findings.....</b>	<b>112</b>
<b>6.3 Future Work .....</b>	<b>114</b>
<b>Appendix A : Design Calculations for Estimating Flexural Demand and Strength.....</b>	<b>116</b>
<b>Bibliography .....</b>	<b>130</b>

## List of Tables

<b>Table 1: Plasticity parameters for CDP model. ....</b>	<b>33</b>
<b>Table 2: Summary of the reference specimen geometry. ....</b>	<b>37</b>
<b>Table 3: Summary of the reference specimen material properties. ....</b>	<b>37</b>
<b>Table 4: Plastic hinge relocation repair geometry. ....</b>	<b>48</b>
<b>Table 5: Summary of ER parameters. ....</b>	<b>51</b>
<b>Table 6: Summary of SS parameters. ....</b>	<b>52</b>
<b>Table 7: Summary of WB parameters. ....</b>	<b>52</b>
<b>Table 8: Summary of FTM parameteric study ....</b>	<b>54</b>
<b>Table 9: Design results of the performance-based repair for numerical investigation. ....</b>	<b>93</b>
<b>Table 10: Summary of peak responses from numerical analysis of the performance-based repair. ....</b>	<b>97</b>

## List of Figures

<b>Figure 1-1: Proposed repair strategies using (a) section enlargement and (b) external energy dissipators.....</b>	<b>4</b>
<b>Figure 2-1: Exposed base plate connection with CRBs (Kadoya et al. 2004).....</b>	<b>8</b>
<b>Figure 2-2: Embedded CFST connection (a) without stiffeners and (b) with stiffeners (Hsu and Lin 2006).....</b>	<b>9</b>
<b>Figure 2-3: Hysteretic performance of a (a) stiffened connection at 0D and (b) 0.5D, and (c) an unstiffened connection at 0.5D (Hsu and Lin 2006). ....</b>	<b>10</b>
<b>Figure 2-4: Proposed grouted, ER connection. ....</b>	<b>11</b>
<b>Figure 2-5: Example of an (a) irreparable, brittle CFST foundation/cap-beam failure and (b) a reparable, ductile CFST tube failure (Lehaman and Roeder 2012; Stephens 2019).....</b>	<b>13</b>
<b>Figure 2-6: CFRP repair of (a) Specimen 1, (b) Specimen 2, and (c) Specimen 3 Rutledge et al. (2014).....</b>	<b>15</b>
<b>Figure 2-7: (a) Mechanical head to improve concrete bonding of repaired rupture bar and (b) its strain vs column displacement response (Krish et al. 2018b). ....</b>	<b>19</b>
<b>Figure 2-8: Idealized hysteretic response of Shape Memory Alloys (Abdulridha et al. 2013). ....</b>	<b>21</b>
<b>Figure 2-9: Bridge column with controlled rocking, and self-centering effects from an internal post-tension bar (White and Palermo 2016). ....</b>	<b>23</b>
<b>Figure 2-10: (a) Proposed repair connection, (b) experimentally tested repair, and (c) steel collar to connect external energy dissipators (White and Palermo 2016). ....</b>	<b>25</b>

<b>Figure 2-11: Hysteretic performance of the (a) undamaged connection and (b) the repaired connection (White and Palermo 2016).</b> .....	<b>25</b>
<b>Figure 2-12: The experimentally tested segmented, CFST bridge columns, fabricated either (a) without energy dissipators or (b) with dissipators (Chou and Chen 2006).</b> .....	<b>26</b>
<b>Figure 3-1: (a) Typical bridge containing CFST columns with a depiction of the (b) ABAQUS model overview and (c) varying mesh densities.</b> .....	<b>30</b>
<b>Figure 3-2: Non-linear stress-strain curves for (a) concrete, (b) the steel tube, and (c) reinforcing steel.</b> .....	<b>31</b>
<b>Figure 3-3: CDP stress-strain curve response of concrete subjected to uniaxial (a) tension and (b) compression (ABAQUS, 2017).</b> .....	<b>33</b>
<b>Figure 3-4: Depiction of the “pre-crack” approach implemented at the plastic hinge of the CFST column.</b> .....	<b>34</b>
<b>Figure 3-5: Geometric detailing of the CFST reference specimen.</b> .....	<b>37</b>
<b>Figure 3-6: Experimental vs numerical response of the reference specimen.</b> .....	<b>38</b>
<b>Figure 3-7: Typical buckling failure captured (a) experimentally and (b) numerically, and (c) its damage-simulation in ABAQUS.</b> .....	<b>39</b>
<b>Figure 4-1: Repair methodologies using (a) welded ring, (b) shear studs, and (c) weld beads</b> .....	<b>41</b>
<b>Figure 4-2: Flexural response of the CFST column repair using the plastic hinge relocation method.</b> .....	<b>43</b>
<b>Figure 4-3: Idealized stress-strain curves of the strain compatibility method.</b> .....	<b>46</b>
<b>Figure 4-4: Idealized stress-strain curves of the plastic stress distribution method.</b> .....	<b>47</b>
<b>Figure 4-5: Reference figure for the final design of the plastic hinge relocation repair.</b> .....	<b>48</b>

<b>Figure 4-6: (a) Numerical overview of the weld bead plastic hinge repair and (b) views of the pedestal.....</b>	<b>50</b>
<b>Figure 4-7: Idealized rigid body rotation of the plastic hinge repair strategy.....</b>	<b>53</b>
<b>Figure 4-8: Depiction of the (a) overview of ER, FTM repairs, (b) moment-drift response, and (c) rigid-body rotation.....</b>	<b>55</b>
<b>Figure 4-9: Concrete stress concentration at 4% drift for repair (a) ER-8t, (b) ER-4t, and (c) ER-2x4t. ....</b>	<b>55</b>
<b>Figure 4-10: Steel stress concentration at 4% drift for repair (a) ER-8t, (b) ER-4t, and (c) ER-2x4t where the concrete of the pedestal and CFST are not shown for clarity.....</b>	<b>56</b>
<b>Figure 4-11: (a) Overview of the shear stud repair method with depiction of its (b) moment-drift and (b) rigid-body rotation response.....</b>	<b>58</b>
<b>Figure 4-12: Concrete stress concentration at 4% drift for repair (a) SS-x2 and (b) SS-x4. ....</b>	<b>58</b>
<b>Figure 4-13: Steel stress concentration at 4% drift for repair (a) SS-x2 and (b) SS-x4 where the concrete of the pedestal and CFST are not shown for clarity. ....</b>	<b>59</b>
<b>Figure 4-14: Depiction of the (a) overview of the weld bead repair and its (b) moment-drift and (c) rigid-body rotation response.....</b>	<b>61</b>
<b>Figure 4-15: Concrete stress concentration at 4% drift for repair (a) WB-x2 and (b) WB-x3 and at 3.30% drift of (c) WB-x3-1.....</b>	<b>61</b>
<b>Figure 4-16: Steel stress concentration at 4% drift for repair (a) WB-x2 and (b) WB-x3 and at 3.30% drift of (c) WB-x3-1 where the concrete of the pedestal and CFST are not shown for clarity. ....</b>	<b>62</b>

<b>Figure 4-17: Comparison of the best performing repair methods, depicting the (a) moment-drift and (b) rigid-body rotation responses. ....</b>	<b>64</b>
<b>Figure 4-18: Hyteretic peformance of WB-x3 compared to the numerical results of the reference specimen.....</b>	<b>64</b>
<b>Figure 4-19: PEEQ vs %Drift of WB-x3 and WB-x3-1 repair methods of extreme fiber reinforcing in pedestal. ....</b>	<b>66</b>
<b>Figure 5-1: Peformance-based repair using external energy dissipators and column-rocking. ....</b>	<b>68</b>
<b>Figure 5-2: Idealized rigid-body rotation of the peformance-based repair.....</b>	<b>69</b>
<b>Figure 5-3: Strain compatability method idealized equilibrium diagram.....</b>	<b>71</b>
<b>Figure 5-4: Idealized plastic stress distriubtion method equilibrium diagram.....</b>	<b>71</b>
<b>Figure 5-5: Depiciton of the BRBar energy dissipator. ....</b>	<b>73</b>
<b>Figure 5-6: Idealized deformation demand of the BRBar at a given column-drift. ....</b>	<b>75</b>
<b>Figure 5-7: (a) Tested BRBar subcomponent with the (b) dimensions of each of its parts. ....</b>	<b>77</b>
<b>Figure 5-8: (a) Internal plugs for (b) pouring the BRM's grout, and (c) removing them after curing. ....</b>	<b>79</b>
<b>Figure 5-9: (a) The experimental testing apparatus and displacement-controlled loading protocols for the (b) BRBars and (c) unbraced speciemens.....</b>	<b>80</b>
<b>Figure 5-10: (a) Unbraced#6 deformation response compared to (b) BRBar#6.....</b>	<b>82</b>
<b>Figure 5-11: Force vs strain responses recorded by the (a) Northern and (b) Western strain gauges on the yielding core.....</b>	<b>83</b>
<b>Figure 5-12: Force vs strain responses recorded by the (a) hoop strain and (b) longitudinal strain gauges on the steel tube of the BRM. ....</b>	<b>83</b>

<b>Figure 5-13: Theoretical strain (in/in) vs force (kip) response of BRBar#6 and Unbraced#6.</b>	<b>84</b>
.....	
<b>Figure 5-14: The (a) idealized buckling profile of BRBar#6 and (b) experimental buckling profile.</b>	<b>85</b>
.....	
<b>Figure 5-15: (a) Bushing machined to be placed (b) between coupler and BRM to reduce lateral displacement.</b>	<b>86</b>
.....	
<b>Figure 5-16: Depiction of the buckling of the top, non-yielding bar which was replaced during testing.</b>	<b>88</b>
.....	
<b>Figure 5-17: Final deformed shape of (a) Unbraced#7 and (b) BRBar#7.</b>	<b>88</b>
.....	
<b>Figure 5-18: Force vs strain responses recorded by the (a) Northern and (b) Western strain gauges on the yielding core.</b>	<b>89</b>
.....	
<b>Figure 5-19: Force vs strain responses recorded by the (a) hoop and (b) longitudinal strain gauges on the steel tube of the BRM.</b>	<b>89</b>
.....	
<b>Figure 5-20: Force vs theoretical strain of BRBar#7 and Unbraced#7</b>	<b>90</b>
.....	
<b>Figure 5-21: The (a) idealized buckling profile of BRBar#7 and (b) experimental buckling profile.</b>	<b>91</b>
.....	
<b>Figure 5-22: (a) Overview of the performance-based repair model and a (b) detail of the pedestal.</b>	<b>93</b>
.....	
<b>Figure 5-23: Depiction of (a) the typical mesh density of (b) the NoGap and (c) Gap model cases</b>	<b>96</b>
.....	
<b>Figure 5-24: Monotonic, single-cycle, and hysteretic load responses compared to the reference specimen.</b>	<b>98</b>
.....	
<b>Figure 5-25: Pedestal and CFST rotation contribution versus total drift of column.</b>	<b>99</b>

<b>Figure 5-26: Depiction of the (a) concrete and (b) steel Von-Mises stress plots, and (c) the PEEQ strain.....</b>	<b>99</b>
<b>Figure 5-27: Monotonic, single-cycle, and hysteretic load responses compared to the reference specimen.....</b>	<b>102</b>
<b>Figure 5-28: Pedestal and CFST contribution total drift of column.....</b>	<b>102</b>
<b>Figure 5-29: Depiction of the (a) concrete and (b) steel Von-Mises stress plots, and (c) the PEEQ strain.....</b>	<b>103</b>
<b>Figure 5-30: Deformed shape of the Gap model under (a) monotonic and (b) hysteretic loads, and the NoGap model under (c) monotonic and (d) hysteretic loads .....</b>	<b>106</b>
<b>Figure 5-31: Displacement comparisons of the (a) NoGap and (b) Gap models along the BRBar height.....</b>	<b>106</b>
<b>Figure 5-32: Comparison of the displacement at mid-point of the BRBar for the Gap and NoGap models. ....</b>	<b>107</b>
<b>Figure A-1: Depiction of composite area method to determine the centroid of repair reinforcing. ....</b>	<b>122</b>

## **1.0 Introduction**

### **1.1 Motivation for Research**

Concrete filled steel tubes (CFSTs) have become an increasingly viable option for use in highway bridge columns, particularly where accelerated bridge construction (ABC) and seismic resiliency is required. CFSTs offer a unique advantage over conventional reinforced concrete (RC) bridge columns for their improved mechanical efficiency and constructability. The steel tube provides flexural resistance at the optimum location in the cross section as well as improved confinement relative to spiral reinforcement typically used in RC columns. The concrete infill provides increased stiffness and strength, and prevents inward local buckling of the steel tube. In addition, CFSTs inherently facilitate ABC, as the steel tube acts as both the transverse and longitudinal reinforcing as well as the formwork for the column. The incorporation of self-consolidating concrete, which eliminates the need for vibration, can further improve accelerated construction (Lehman and Roeder, 2012; Roeder et al., 2014).

The ductility and energy dissipation capabilities of CFSTs makes them attractive for use in regions with seismic hazards. Until recently, their widespread use in highway bridge construction has been limited, in part due to a lack of standard connection details. However, in recent years, extensive research has developed several CFST connections for use in highway bridge construction, particularly for use in moderate and high seismic regions. Among these connections is the embedded ring (ER) connection, which is a full-strength moment connection that consists solely of an annular ring welded to the base of the CFST and embedded in the adjacent concrete element. When appropriately designed, the failure mode of the ER connection is characterized by

hinging in the CFST column adjacent to the connecting concrete element consisting of tube buckling, followed by tube tearing for larger reversed cyclic drift demands (Stephens et al., 2016b). This readily identifiable and accessible failure mode presents a unique and advantageous opportunity for repair following seismic events. Compared to typical, seismically damaged RC columns, damaged CFSTs exhibit a significant reduction in the amount of concrete spalling from the continuous confinement of the steel tube. In addition, the steel tube provides an opportunity for welded or bolted connections at the steel interface which is not possible in excessively spalled, RC columns.

## **1.2 Research Objective**

The objective of this research is to develop a series of practical repair strategies for CFST bridge columns that can return strength and stiffness.

### **1.2.1 Proposed Repair Strategies**

Given the success of recent research in plastic hinge relocation (Krish et al., 2018a; Lehman et al., 2001) and performance-based repairs (Chou and Chen, 2006; White and Palermo, 2016) the two proposed repair methods are provided herein that incorporate (1) section enlargement via a surrounding CFST pedestal and (2) externally attached energy dissipators to improve seismic performance. A numerical analysis approach was adopted for assessment where the proposed strategies were evaluated on the basis of their ability to reestablish loss strength, stiffness, and

ductility as compared to previous, experimental research of CFSTs that utilize the ER connection (Stephens et al., 2016a, 2016b).

The first approach, depicted in Figure 1-1a, applies a CFST pedestal around the damaged region of the CFST column and is reinforced with rebar to provide resistance equivalent to the original plastic moment capacity of the column. The height and diameter of the pedestal was selected to ensure that adequate force transfer was provided by both natural bond as well as a series of force transfer mechanisms that are welded to the original CFST column. The latter was of particular interest in this study, where a suite of mechanisms was evaluated with varying geometry, quantity, and location.

Similarly, a performance-based design approach depicted in Figure 1-1b, was taken where a CFST pedestal encases the damaged section. Column-rocking is initiated along the damaged region of the CFST by introducing a welded, annular plate at the base of the CFST to limit damage and eliminate the need for reinforcement to pass between the CFST pedestal and foundation (Staton et al., 2014). Lateral force and moment resistance are provided by external energy dissipators, namely buckling restrained bars (BRBars), that are bolted to the outside of the repair pedestal. This simple bolted connection provides a unique opportunity to efficiently replace the damaged BRBars post-earthquake.

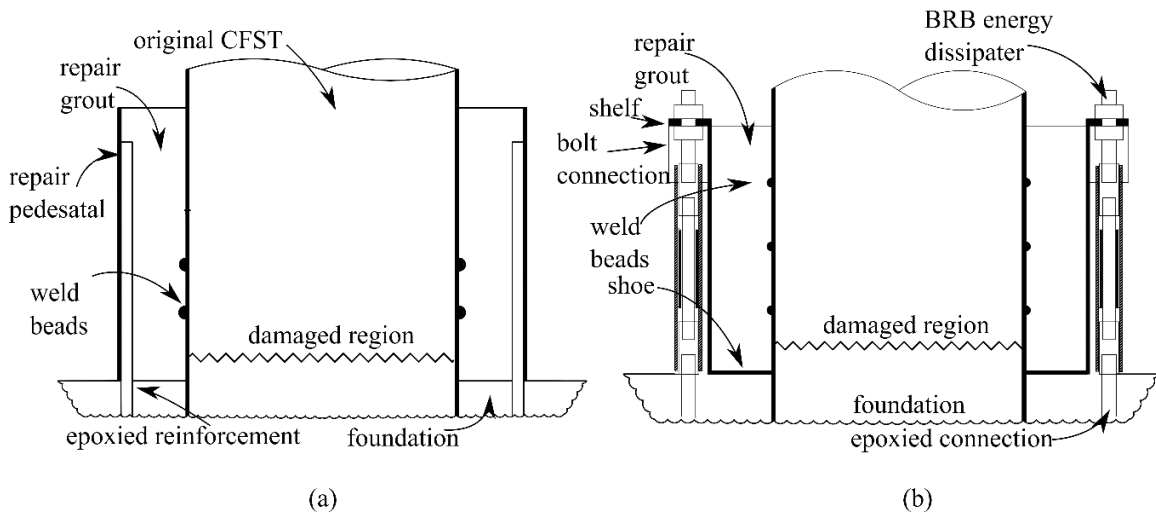


**Figure 1-1: Proposed repair strategies using (a) section enlargement and (b) external energy dissipators.**

### 1.3 Report Outline

This report will consist of six chapters that are summarized as follows.

Chapter 2 provides a literature overview of relevant research pertaining to the embedded ring connection and repair strategies of RC and CFST bridge columns.

Chapter 3 details the analytical approach for modelling undamaged and damaged CFST bridge columns that was used in this research program.

Chapter 4 introduces the plastic hinge relocation repair that utilizes section enlargement. A detailed overview is provided of its design strategy and numerical model as well as the monotonic, moment-drift responses of the various force transfer mechanisms investigated. A hysteretic response comparison is then made between the best repair strategy and an undamaged CFST column.

Chapter 5 covers the performance-based repair strategy where external energy dissipators (e.g. BRBars) are incorporated. First, the repair strategy is introduced and a design procedure is covered. Next, the BRBar is described, including an experimental testing procedure and its results. Next, the modelling and design procedure of the BRBar repair strategy is covered and the results of their hysteretic performances are provided.

Chapter 6 provides a summary of the significant conclusions derived from this research program and concludes with future research recommendations.

## **2.0 Literature Review**

The repair and retrofit of damaged reinforced concrete (RC) columns has been researched extensively (He et al., 2015, 2013; White and Palermo, 2016; Wu and Pantelides, 2017). In addition, repair strategies for damaged CFST columns in buildings have been previously evaluated due to their widespread use in building construction in Asia (Chou and Chen, 2006; Tao et al., 2008, 2007). This chapter summarizes these research trends to provide insight on developing a successful repair strategy for CFST bridge columns that utilize the ER connection. First, embedded and exposed CFST connection types are reviewed to determine typical connection failure modes, then plastic hinge relocation and performance-based repair strategies for RC and CFST columns are covered to provide a foundational understanding of current repairs that have been successful.

### **2.1 CFST Column to Foundation/Cap-Beam Connections**

CFST connections can be characterized as either exposed dowel type or embedded. Connection performance is assessed by the ability of the connection to develop the strength of the column and ductility capacity under monotonic and reverse cyclic loadings. The following sections provide a background exposed\dowel type versus embedded CFST connections and summarizes research on the two connection types.

### 2.1.1 Exposed CFST Connections

Extensive research has been conducted on exposed based-plate connections (Hitaka et al., 2003; Hsu and Lin, 2006; Jothimani and Umarani, 2019; Kadoya et al., 2004), which typically consist of a steel plate welded to the base of the CFST column, with steel bolts or dowels that connect to the base plate and anchor into the adjacent concrete component. These connections are usually easier to construct than embedded connections, however it can be difficult to develop the full plastic capacity of the CFST and achieve sufficient ductility, as the strength and ductility are controlled by the anchor bolts rather than the CFST column (Hsu and Lin, 2006; Kadoya et al., 2004). In the case of the 1995 Kobe Earthquake, it was found that exposed base-plate columns were significantly damaged and performed far more poorly relative to embedded type connections, due to fracture of the anchor bolts and crushing of the concrete core (Azizinamini and Ghosh, 1997).

Following the Kobe Earthquake, there was an effort to improve the structural performance of exposed base-plate CFST connections. Kadoya et al. (2004), addressed this concern by introducing additional central reinforcing bars (CRBs) into the exposed, base-plate connection detail, as illustrated in Figure 2-1. The connection is constructed by partially embedding several CRBs into the foundation prior to setting the CFST. The exposed portion of the CRBs are then passed through a concentric hole in the base-plate which is welded to the end of the CFST.

In this study, the hysteretic response of 10 specimens under combined axial and horizontal loading was evaluated. The primary parameters included: the loading condition (constant or varying magnitude axial load), the presence of CRBs, and the size CRBs. Results showed that the additional CRBs successfully improved the performance of base-plate CFST columns. The governing failure mode consisted of cone failure of the foundation concrete due to anchor bolt

pullout combined with compressive failure of the filler mortar beneath the base plate. More importantly, the failure of the base plate nor rupture of the anchor bolts were observed during testing. When compared to baseline columns without CRBs, the initial stiffness improved by 20% and the ultimate moment capacity increased 40% – 80% (Kadoya et al., 2004).

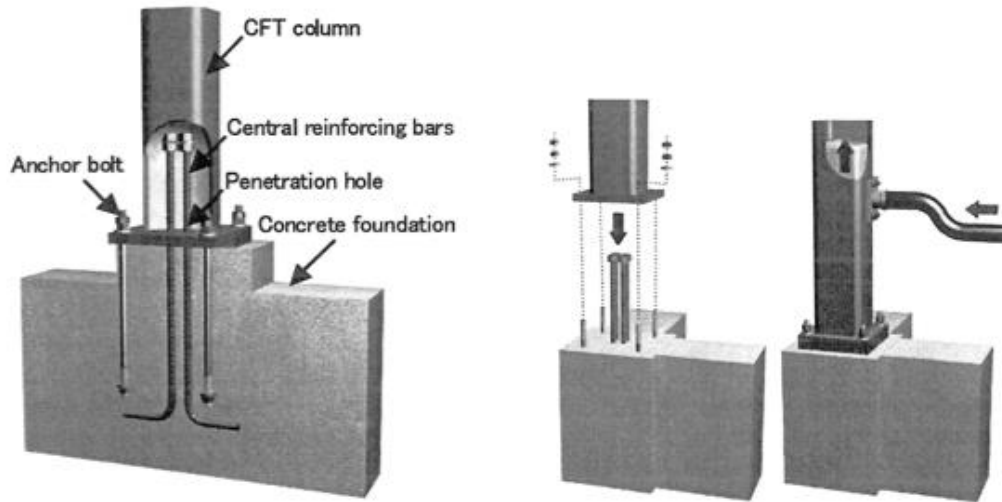


**Figure 2-1: Exposed base plate connection with CRBs (Kadoya et al. 2004).**

### **2.1.2 Embedded CFST Connections**

Embedded CFST connections are fixed into the foundation during construction through embedment of the steel tube and have been previously researched extensively (Hsu and Lin, 2006; Kappes et al., 2016; Marson and Bruneau, 2004; Stephens et al., 2016a) Though more difficult to construct, this type of connection tends to have superior rigidity over exposed connections. However, high concentrated stresses located at the interface of the embedded CFST and surrounding concrete leads to concrete bearing stress failures and degradation in the rigidity of the

connection, shown in Figure 2-2a (Hsu and Lin, 2006). Hsu and Lin (2006), proposed a new embedded connection detail, shown in Figure 2-2b, which introduces steel stiffeners welded to the base of the embedded CFST. The proposed detail, reduces crushing of the embedded, surrounding concrete, improves column rigidity, and shifts the critical damage of the connection from the base of the CFST, to the top of the adjoining concrete element.

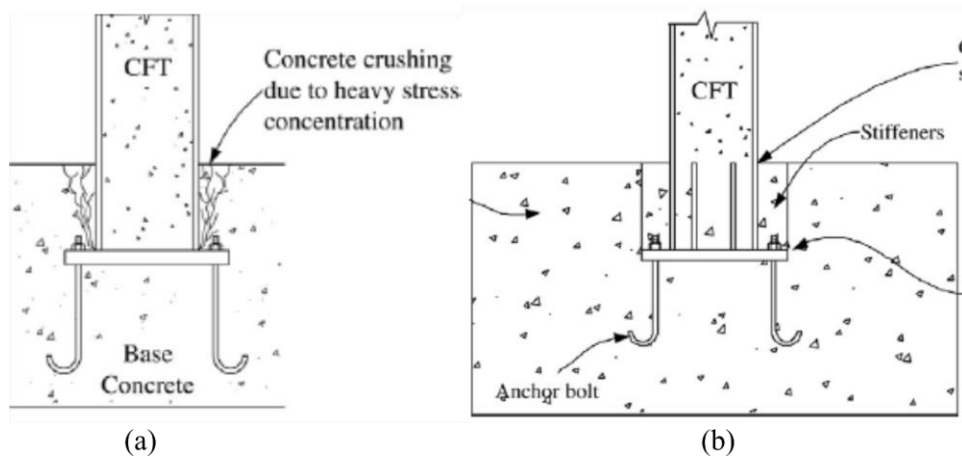


**Figure 2-2: Embedded CFST connection (a) without stiffeners and (b) with stiffeners (Hsu and Lin 2006).**

Seven square CFST specimens were tested with varying embedment depths and connection detailing. Three specimens without stiffeners were tested with depths varying from  $0.5D$ ,  $1.0D$ , and  $1.5D$  where  $D$  represents the width of the CFST. Similarly, four stiffener reinforced specimens were tested with the additional specimen having an embedment depth of  $0D$ . Columns were sized as approximately 14-inch square tubes with a 0.25-inch thick wall. The end plate was 1.25-inch thick and the reinforcing stiffeners were sized at 3-inch wide and 5/8-inch thick plates. Hydraulic jacks applied via a transverse loading beam applied an axial load to the column while a servo-controlled hydraulic actuator provided the lateral, reverse cyclic loading.

As shown in Figures 2-3a to 2-3c, the hysteretic performance is directly related to the embedment depth. Comparing Figures 2-3a and 2-3b, it can be seen that as embedment depth increases, the rigidity and energy dissipation capability greatly improve, however a plateau was observed when the embedment depth was equal to the depth of the section (1.0D). In a similar effect, by comparing Figure 2-3b with 2-3c, it is observed that additional stiffeners added to the base connection can improve energy dissipating and drift capabilities (Hsu and Lin, 2006).

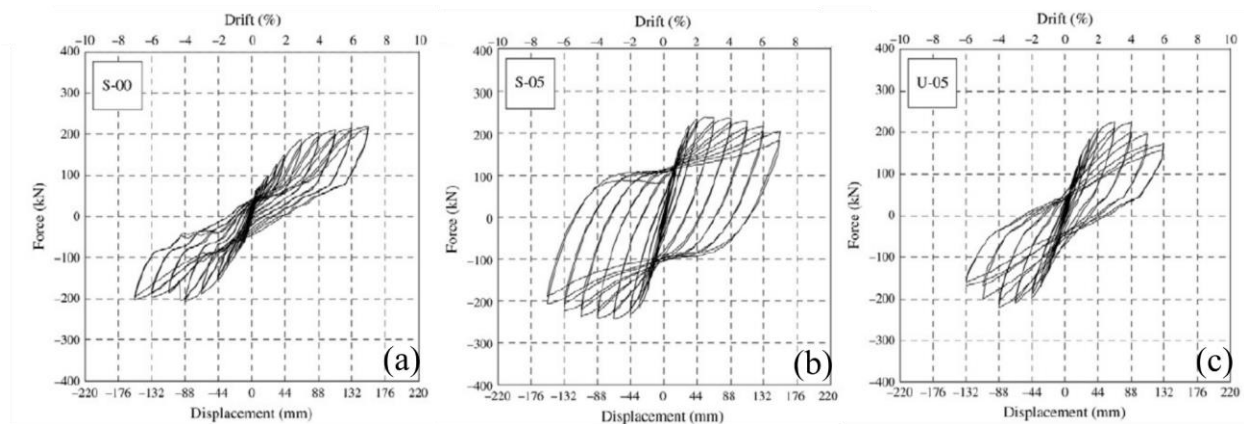


**Figure 2-3: Hysteretic performance of a (a) stiffened connection at 0D and (b) 0.5D, and (c) an unstiffened connection at 0.5D (Hsu and Lin 2006).**

### 2.1.3 The Embedded Ring (ER) Connection

Lehman and Roeder (2012), proposed an embedded CFST connection for the application of CFST bridge columns in moderate and high seismic regions. This connection, referred to as the embedded ring (ER) connection, consists of a steel, annular ring welded to the submerged end of the CFST column as shown in Figure 2-4. In contrast to the previously discussed exposed and embedded connections, the ER connection relies solely on the annular ring for force transfer and

moment development (i.e. no additional anchor bolts nor reinforcement are required to develop the connection), which in turn greatly facilitates construction. In addition to a monolithic construction procedure, a grouted connection was proposed for application in accelerated bridge construction and use of precast concrete elements as depicted in Figures 2-4a to 2-4d (Lehman and Roeder, 2012).

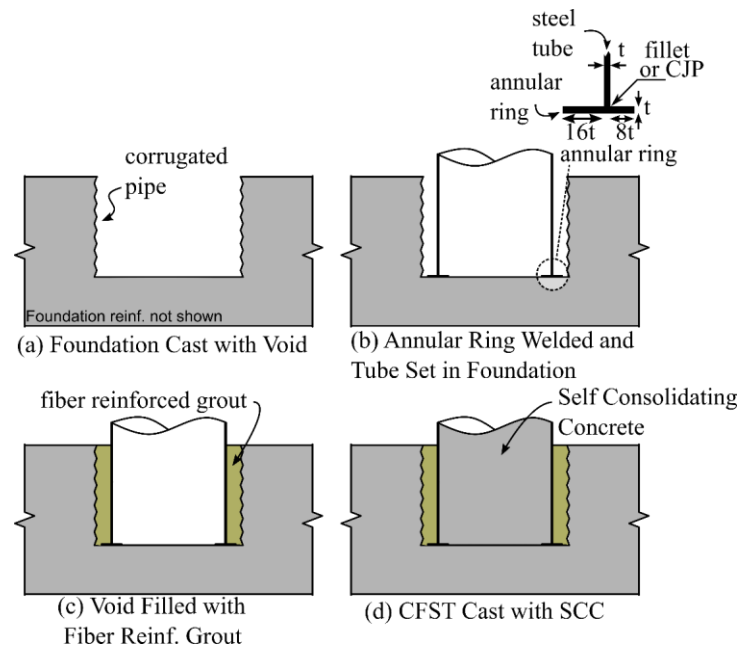


**Figure 2-4: Proposed grouted, ER connection.**

A large-scale experimental program was performed of the ER connection on 19 specimens to observe the effects of varying several design, geometric, and loading properties. Specifically, the behavior of the both the monolithic and grouted connection was of interest, as well as the effect of varying tube diameter, tube diameter over thickness ratio ( $D/t$ ), and embedment depth. Specimens were tested in a self-reaction frame using an axial load of approximately 10% the gross compressive strength of the CFST, in addition to a cyclic lateral load to simulate earthquake loading effects.

The results showed that larger embedment depths significantly improve drift and moment capacities, where seismic drift demands were far exceeded with minimal degradation and damage. Inadequate embedment resulted in premature failure before the plastic moment capacity was achieved due to significant concrete damage at the connection interface. (Lehman and Roeder, 2012). The ER connection has undergone extensive experimental, parametric investigations to assess the influence of various design parameters on connection performance. Stephens et al. (2016b), synthesized these findings and developed a series of design equations and provided optimal material properties for the ER, CFST for its use in mid-to-high seismic regions. Among these design parameters are (1) ER dimensions, (2) embedment depth, and (3) specific depth to resist punching shear (Stephens et al., 2016b).

Through research, it was found that a well-detailed ER, CFST column can effectively produce a very stiff and ductile response under lateral, cyclic loadings. Connections inadequately designed typically exhibited a premature, non-ductile failure response, depicted in Figure 6a, located at the interface of the embedded CFST. This failure mode is considered irreparable and full replacement of the CFST and foundation/cap-beam are required (Lehman and Roeder, 2012; Stephens, 2016). The damage progression of a well-designed connection with sufficient embedment depth (i.e. around  $0.9D$ ) is characterized by small, localized foundation/cap-beam cracking around the same time as an insufficiently embedded connection, however, cracks tend to remain contained with further lateral deflections. Furthermore, the failure mode of a well-detailed connection is centralized to the steel tube and is characterized by outward, tube buckling typically observed around 3-4% drift. Subsequent drift demands further deteriorate the steel tube where around 6-7% steel tube tearing is observed with concrete spalling. Until tearing occurs however, minimal concrete confinement loss is observed even after severe outward tube buckling. This

ductile tube buckling mode is considered to be a repairable damage state, and is shown in Figure 6b for clarity (Lehman and Roeder, 2012).

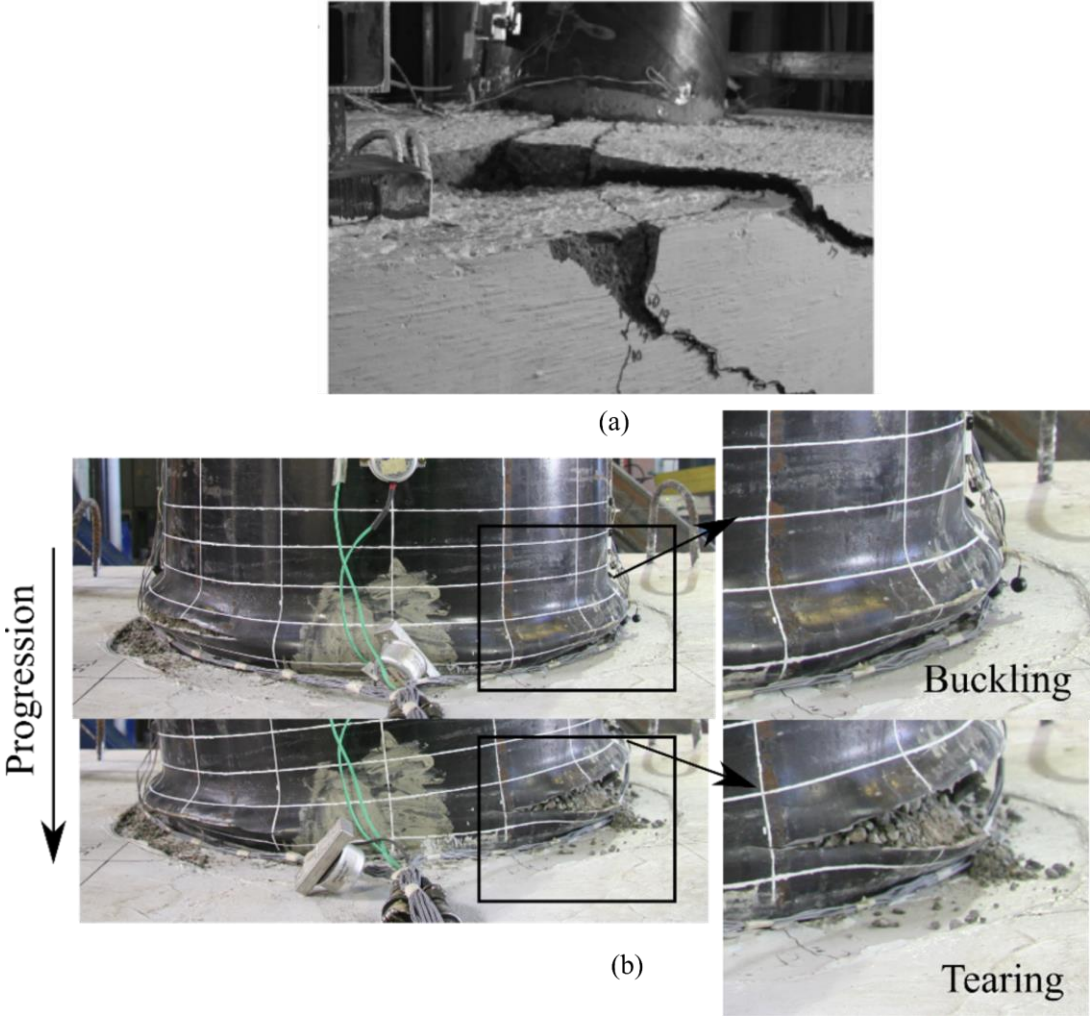


**Figure 2-5: Example of an (a) irreparable, brittle CFST foundation/cap-beam failure and (b) a repairable, ductile CFST tube failure (Lehman and Roeder 2012; Stephens 2019).**

### 2.2 Plastic Hinge Relocation Repairs

Damage in reinforced concrete columns subjected to seismic loading is commonly localized to the plastic hinge region. As such, a common solution for repair is plastic hinge

relocation which aims to redevelop the plastic hinge location away from the previous location. Generally, hinge relocation is achieved in two ways: (1) jacketing the repaired region using fiber reinforced polymer (FRP) wraps (Rutledge et al., 2014; Tao et al., 2008) and (2) enlarging the diameter of damaged location with concrete or grout (Krish et al., 2018a; Lehman et al., 2001). The following section provides an overview of these two methods as they are applied to both RC and CFST columns.

### **2.2.1 Fiber Reinforced Polymer (FRP) Wraps**

The use of FRP wraps has gained noticeable traction in previous years for its potential as a plastic hinge relocation solution for damaged columns (Alexander et al., 2008; He et al., 2013; Truong et al., 2017). FRP wrapping lends itself well as a rapid-repair solution where, once specimen surface preparation is sufficiently completed, jacketing can be readily applied to concrete using epoxy and/or anchors. Researchers have successfully demonstrated that FRPs can reestablish lost shear and flexural strength which is dictated by the orientation of the FRP; the flexural capacity is increased by orienting the fibers vertically, while the shear capacity is increased by orienting them horizontally. In addition, improving concrete confinement is also a primary objective of repair/retrofit strategies, and it has been shown that jacketing damaged concrete sections with FRPs, significantly improves confinement and structural response (He et al., 2013; Rutledge et al., 2014).

A number of research programs have been conducted to implement repair objectives to regain strength, stiffness, and concrete confinement in a wide damage range of concrete columns, and an extensive review can be found in He et al. (2015). Rutledge et al. (2014) sought to provide a rapid-repair solution of earthquake-damaged RC columns that have experienced severe spalling

and buckling, and/or rupture of longitudinal reinforcement. The proposed repair utilized carbon fiber reinforced polymer (CFRP) jackets that wrap the damage region, restoring flexural, shear, and ductile capacity. Jackets were developed by incorporating CFRP anchors that anchored into the foundation. Three large-scale experimental tests were performed at varying degrees of damage and repair objectives. For example, the first specimen experienced only bar buckling at the plastic hinge region and was repaired with CFRP sheets at the damaged region, and the new plastic hinge region, to improve its ductility response. The final two specimens were repaired solely in the original plastic hinge region; however, the second specimen experienced bar buckling, while the third specimen experienced both bar buckling and rupture in the damaged region. These repairs are depicted in Figures 2-6a to 2-6c, respectively (Rutledge et al., 2014).

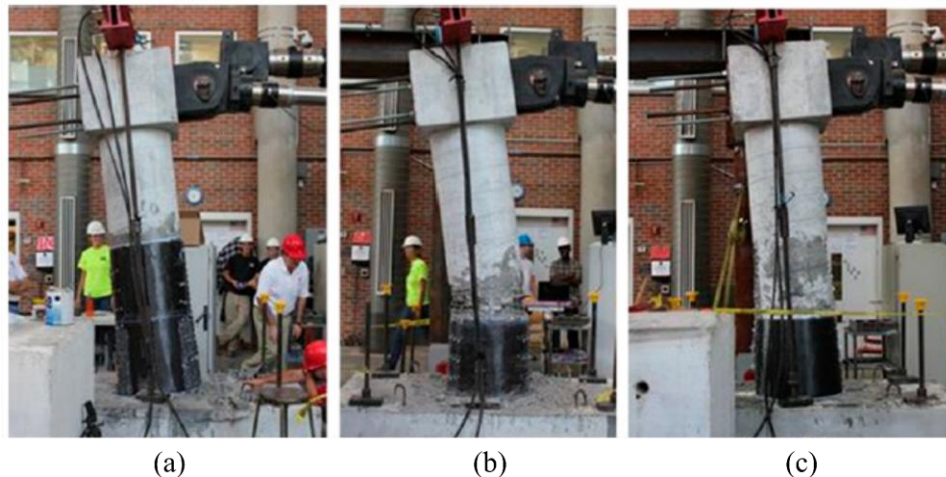


**Figure 2-6: CFRP repair of (a) Specimen 1, (b) Specimen 2, and (c) Specimen 3 Rutledge et al. (2014).**

Specimens, sized at 23.5-inch in diameter and reinforced with 16, #6 longitudinal bars and #3 spirals, were initially tested in a previous study performed by (Goodnight et al., 2012) where columns were subjected to reverse cyclic lateral loadings that matched that of real earthquake loading histories. Under Rutledge et al. (2014), post-earthquake “aftershock” loadings were

applied to the damaged, unrepaired column to obtain a force-displacement response for comparisons. Then, repaired columns were subjected to a displacement-controlled, three cycle set load history. Results indicated that the CFRP wrap repair strategy could successfully reestablish column strength and ductility capacities, however over-strengthening the column, such as in the first specimen, resulted in failure in the foundation which otherwise should be capacity-protected. Without additional strengthening, Specimen #2 proved to successfully develop a plastic hinge above the repair region while Specimen #3, which experienced both bar buckling and fracture, failed prematurely due to the rupturing of the CFRP anchors (Rutledge et al., 2014).

Researchers have used the success of repair RC structures using FRP jackets as motivation to extend this repair strategy to CFST columns. While there is limited research on the utilizing FRP jackets for plastic hinge relocation of earthquake-damaged, CFST columns, there has been an extensive research program where CFRP jackets have been used to repair fire-damaged CFSTs (Tao et al., 2008, 2007). Tao et al. (2008) observed the effects of repairing eight CFST beam-column specimens that experience extensive fire damaged; four specimens were circular while the other four were square. Damaged specimens exhibited global and local tube buckling as well as internal concrete crushing before repair, at the location of buckling, though crushing was not observed in specimens that did not buckle. Upon repair, it was found that CFRP wrapped specimens were able to restore some strength and stiffness, however the strength was not returned entirely to the original capacity. The number of CFRP layers directly correlated to an increase in ductility performance, where increasing from one to two layers, increased the ductility coefficient (ratio of ultimate displacement to yield displacement) from 11.25 to 12.58, respectively. This is due to the delay or even prevention of tube buckling due to the increase in layers. Shape also noticeably contributed to prevention of tube buckling, where circular specimens did not experience

local tube buckling, while square specimens did. This is most likely contributed to the fact that circular specimens have superior confinement effects from CFRP jacketing over square specimens.

### **2.2.2 Section Enlargement**

Section enlargement repair strategies utilize a built-up section around the damaged region, to recover, and exceed the original flexural moment capacity of the previous plastic hinge region, thus shifting the failure region above the repaired section. This is achieved by significantly increasing the cross-sectional size of the column by bonding new concrete around the damaged region. Section enlarged repairs are conventionally constructed by providing formwork around the column to place the new concrete, which is commonly left after construction to improve confinement of the repair concrete (Krish et al., 2018a).

Lehman et al. (2001) performed an experimental investigation on the effectiveness of section enlargement repairs of RC columns with moderate and severe damage resulting from lateral loading. The moderately damaged columns only experienced concrete spalling and bar yielding, and were repaired using conventional methods such as epoxy injections and concrete cover replacement. The severely damaged columns, having experienced bar buckling and rupture, underwent a more extensive repair procedure. Ruptured bars were replaced using mechanical couplers and new reinforced concrete was jacketed around the damaged section. One column was repaired to force plastic hinging above the repair, while the other was designed to the original capacity, thus reestablishing plastic hinging in the enlarged section. Typical columns were 2-ft in diameter and were loaded axially and laterally at a location 8-ft above the base. The hysteretic performances of the repaired columns were compared against undamaged columns and it was found that the repaired severely damaged columns successfully regained strength and stiffness,

and achieved their repair intention for all cases (i.e. plastic hinging above or at the enlarged section). The moderately damaged column, however, failed to reestablish its previous stiffness and strength.

One of the key design considerations of this investigation was limiting the shear force imposed on the original column, due to the reduced height available to develop the plastic moment above the pedestal. However, a minimum pedestal height is required to develop the repair reinforcement, as well as to sufficiently repair the damaged area of the original plastic hinge. Overall, the results of this study successfully demonstrate the effectiveness of section enlargement as repair strategy for earthquake-damaged bridge columns (Lehman et al., 2001).

More recently, Krish et al. (2018), carried out an experimental investigation on plastic hinge relocation of severely damaged RC columns to demonstrate that RC columns that have experienced both longitudinal bar buckling and fracture, can be readily repaired. A similar repair protocol as described in Lehman et al. (2001) was followed for six, severely damaged columns with a focus on using commercially available repair materials (i.e. two-part epoxy and ready-mix concrete) to demonstrate that these materials can be used to streamline the repair process. Column pedestals were designed using moment-curvature analyses to ensure that the applied moment at the repaired section, does not exceed the pedestal's elastic moment capacity (Krish et al., 2018b). In addition to this, a focus was made on providing methods to improve the bonding performance of the ruptured bars in the repair concrete. It was observed from the first tested column that if the repaired bars were left untreated to improve bonding, bars would experience severe debonding from the repair concrete under extreme lateral loads and ultimately would result in a softening response and pinching behavior of the column. As shown in Figure 2-7a, a steel, mechanical anchor head can be attached to the base of the fractured bar to improve their flexural response. This

approach was applied to two of the repaired columns and proved to reliably develop the strain response of the headed, fractured bar with no debonding observed, as shown in Figure 2-7b (Krish et al., 2018a).

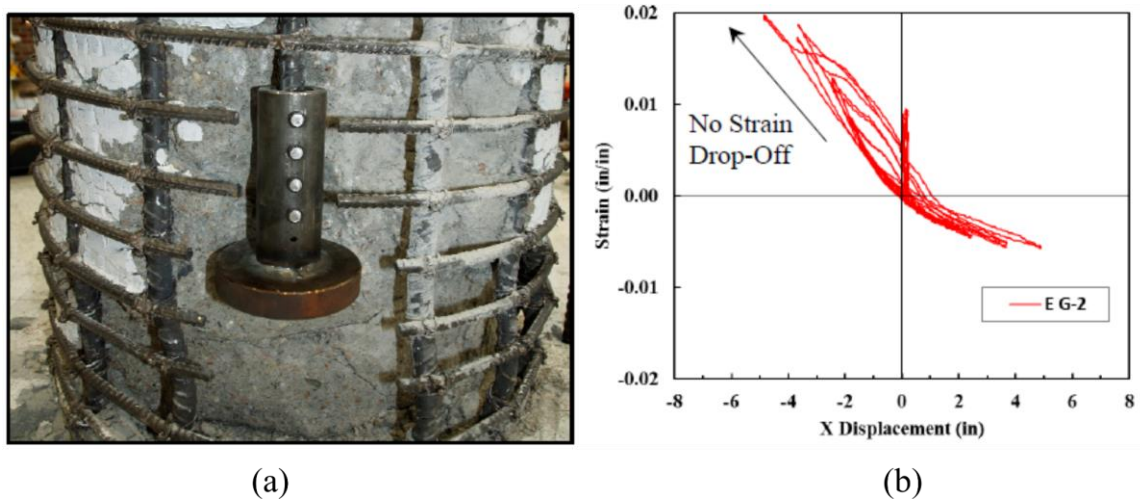


**Figure 2-7: (a) Mechanical head to improve concrete bonding of repaired rupture bar and (b) its strain vs column displacement response (Krish et al. 2018b).**

### **2.3 Performance Based Repair Strategies**

The Northridge earthquake of 1994 and the Kobe earthquake of 1995, brought about significant change to seismic design philosophies. During this time, conventional seismic design methodologies were employed with the intent of designing for limits of stresses and member forces against prescribed lateral earthquake forces (Ghobarah, 2001). This design direction is largely based on input parameters, like material properties and strength, and relies on the inelastic behavior of the entire steel structure for energy dissipation. While this approach typically prevents collapse, excessive seismic damage seen as residual column drifts and member displacement is

commonplace, and often times the structure will be deemed unserviceable after seismic events. In response, a new design philosophy has come forth which focuses on structure performance, such as its serviceability and repairability post-earthquake events. This performance based seismic design (PBSD) approach aims to control damage to an isolated region, or limit damage of the structure in general, allowing for a rapid-repair solution that can easily be applied post-earthquake (Shoeibi et al., 2017). Recent research has sought to implement these design philosophies to bridge structures as well, specifically by incorporating external or internal energy dissipators for damage isolation, and/or implementing column-rocking and column self-centering techniques to limit damage and residual drifts. This section highlights these PBSD techniques and concludes with research programs that have successfully implemented them to RC and CFST bridge columns.

### **2.3.1 Available Energy Dissipators for Implementation in Bridge Structures**

Energy dissipators are uniquely designed systems that are preemptively engineered to dissipate energy. The mechanism to dissipate energy can be categorized as either a (1) yielding or (2) non-yielding mechanism. The latter can consist of viscous dampers that resist motion through viscous friction or friction dampers which can dissipate energy through friction buildup between steel plates. These non-yielding mechanism, however, are typically more costly and less effective and were not considered in this research (White, 2014), while yielding mechanisms are more suitable for implementation in bridge structures.

Energy dissipators that utilize a yielding mechanism are typically made of steel, and rely on plastic development from large inelastic deformation to dissipate energy. RC structures, for example, depend on plastic development of internal steel rebar for energy dissipation which commonly results in large, residual deformations, making continued service unlikely. At the

forefront of research, is the application of Shape Memory Alloys (SMAs) as reinforcement in RC structures. SMAs can exhibit large deformations, and upon the application of heat or the removal of stress, will return to their original, undeformed shape. Nickel-Titanium SMAs (Nitinol) is the most commonly investigated superelastic SMA for structural application and contains 56% nickel and 44% titanium alloy. The ideal hysteretic response is shown in Figure 2-8 (Abdulridha et al., 2013).

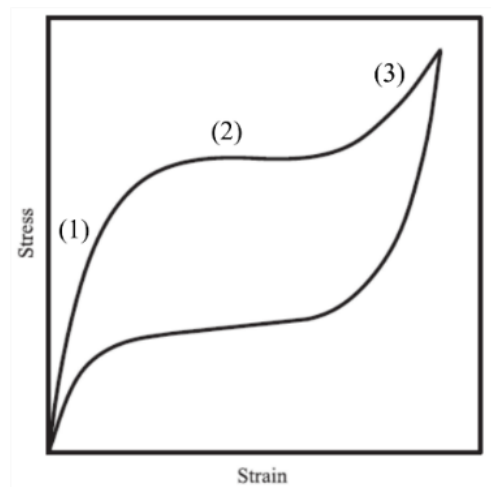


**Figure 2-8: Idealized hysteretic response of Shape Memory Alloys (Abdulridha et al. 2013).**

As shown, the unloading response of the SMA follows the reverse of its loading stage, creating a flag-shaped, hysteretic response with theoretically no permanent deformation (Abdulridha et al., 2013).

U-Shaped Flexural Plates (UFPs) are a section of mild steel, bent into a U-shape that dissipates energy through shear loadings. The relative displacement of one side of the UFP creates a rolling type phenomenon along the curved region of the plate, ideally isolating the steel yielding to the semi-circular region of the UFP, allowing large deformation and stable, hysteretic development (Baird et al., 2014). UFPs have increased in popularity in seismic research due to

their successful implementation into coupled timber shear wall systems and have even been employed in modern day structures such as the Southern Cross Hospital in Christchurch, New Zealand (Baird et al., 2014; White, 2014).

Tension and compressive loading and unloading action is frequently seen in structural members resisting lateral forces from earthquakes. To concentrate plastic development and energy dissipation, some of these particular members can be manufactured with a reduced cross-section across their midspan length. This is particularly advantageous, because if designed properly, only the reduced cross-section will yield, allowing for the rest member to remain elastic. However, by reducing the moment of inertia of the cross-section at the midsection, the compressive loading enforced on the member can result in global buckling before yielding can occur, thus greatly reducing the member's energy dissipation capacity. To overcome this, a buckling restraining mechanism is introduced that physically restrains lateral movement of the cross-section, therefore enabling the development of a symmetrical hysteretic curves (i.e. yielding in both tension and compression). This type of energy dissipator, called a buckling restrained fuse (BRFs), originated from buckling restrained braces (BRBs) which follow the same energy dissipating principal. BRFs are commonly made of plain, circular bars with a reduced diameter whereas BRBs have a variety of cross-sections including flat bars or cruciforms (Bruneau et al., 2011; White, 2014).

### **2.3.2 Column-Rocking and Self-Centering Techniques**

Low-damage bridge column design philosophies have gained recent traction for their ability to maximize energy dissipative capabilities, while reducing residual drifts and subsequent repair costs (Marriott et al., 2011; Staton et al., 2014). To achieve this, two strategies have emerged: (1) column-rocking and (2) column self-centering. The first, as depicted in Figure 2-9,

is achieved by debonding the base of the column from the footer/cap-beam by using a piece of interfacial membrane, like a steel plate or elastomeric rubber, allowing the column to rock freely along the rocking interface with limited damage. This is then combined with an internally unbonded, post-tensioned bar that continuously applies a self-centering, axial load through the column and into the adjacent concrete element. This results in minimal residual drifts post-earthquake (White, 2014).

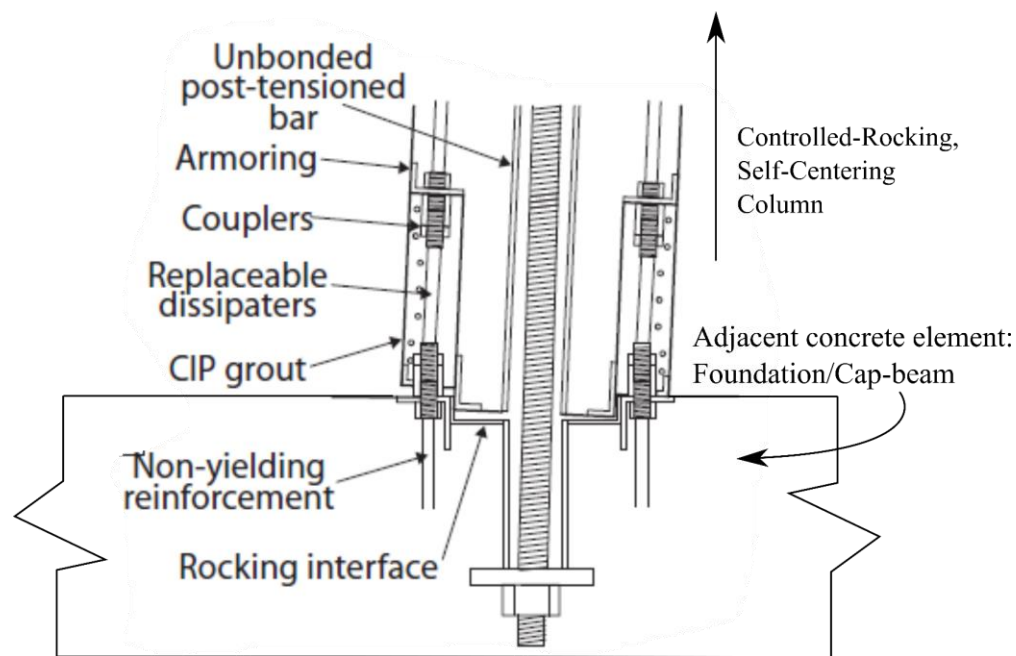


**Figure 2-9: Bridge column with controlled rocking, and self-centering effects from an internal post-tension bar (White and Palermo 2016).**

Residual drift reduction can also be achieved by incorporating, segmentally constructed, post-tensioned bridge columns. Here, individual segments of the bridge column are stacked on each other, and connected through a concentric, post-tensioned duct. This allows for column-rocking at each segmental interface as well as a recentering, axial force to reduce residual drift (Dawood et al., 2012). In addition, SMAs are frequently employed to achieve self-centering effects

due to their shape memory nature. This is achieved by internally or externally attaching the SMAs at the extreme deformation location of the structure, which reduces residual deformations upon reloading (Abdulridha et al., 2013; Varela and ‘Saïid’ Saiidi, 2016).

### **2.3.3 Dissipative Controlled Rocking (DCR) Columns**

Dissipative controlled rocking (DCR) combine debonded, post-tensioning rods with column rocking and energy dissipative devices. While research in implementing similar DCR columns objectives in the repair strategies of CFST bridge columns is limited, there has been extensive studies for the new-construction and repair of RC DCR bridge columns. White and Palermo (2016) proposed a controlled damage, member socket column system (Figure 2-10a) that incorporates self-centering, post-tensioned bars and debonded, internal reinforcement to induce a natural rocking surface along the adjacent concrete element interface. This connection is preemptively designed to facilitate a post-earthquake repair strategy that utilizes externally attached BRFs by including cast-in place threaded inserts located at the base of the foundation and side of the column. The experimentally tested repair methodology, however, did not include threaded inserts, due to limited space of the half-scale tested column. Rather, chemically anchored bars were used and an FRP wrap was provided for additional confinement of the plastic hinge region due to the excessive concrete spalling of the undamaged RC column. This connection detail, as shown in Figure 2-10b is referred to as the “experimental connection” herein, and incorporates a steel collar (Figure 2-10c) that attaches to the chemically, anchored threaded bars. This collar then provides a surface to bolt the BRF, energy dissipators, thus simplifying their replacement upon failure. The BRFs used in this connection detail are a groove-type dissipator which was found

to be successful in resisting large tension and compression intervals. Their design is covered more thoroughly in (White, 2014; White and Palermo, 2016).

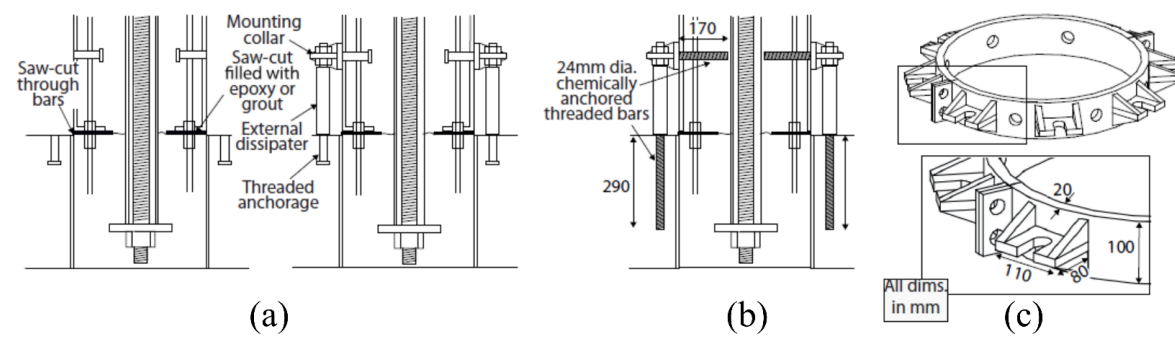


**Figure 2-10: (a) Proposed repair connection, (b) experimentally tested repair, and (c) steel collar to connect external energy dissipaters (White and Palermo 2016).**

The experimentally tested repair connection was subjected to reverse, cyclic biaxial loadings approximately 8-ft above the foundation. A biaxial drift cycle of 7.8% was achieved during testing, however mounting collar sliding was observed at 1.5% drift and at 2.5% drift, pullout of the energy dissipaters was also observed. Figure 2-11a and 2-11b depict the hysteretic performance of the undamaged versus the experimentally tested repair strategy.

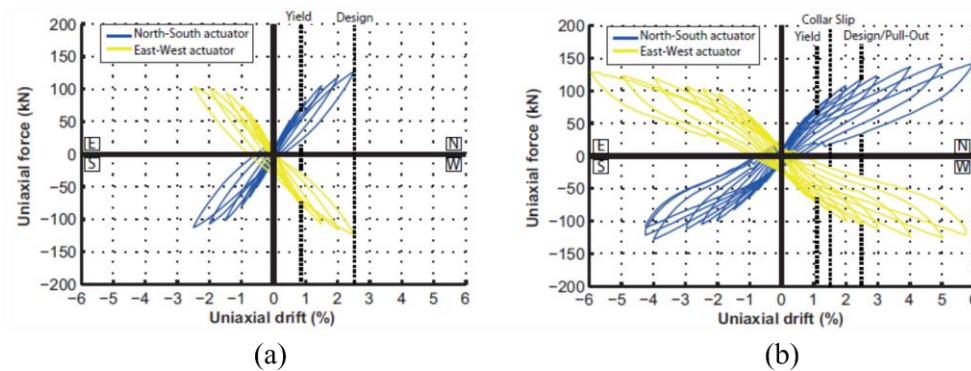


**Figure 2-11: Hysteretic performance of the (a) undamaged connection and (b) the repaired connection (White and Palermo 2016).**

As shown roughly 1%, residual drift remains of the repaired column suggesting that achieving a flag-shaped, hysteretic behavior is promising. For future testing, it was concluded that additional improvements need to be made to prevent premature slipping and pullout of the collars and dissipators (White and Palermo, 2016).

Chou and Chen (2006) experimentally tested two segmental, CFST bridge columns for new-construction, where one excluded energy dissipators (Figure 2-12a) and the other was fabricated with external energy dissipators (Figure 2-12b).

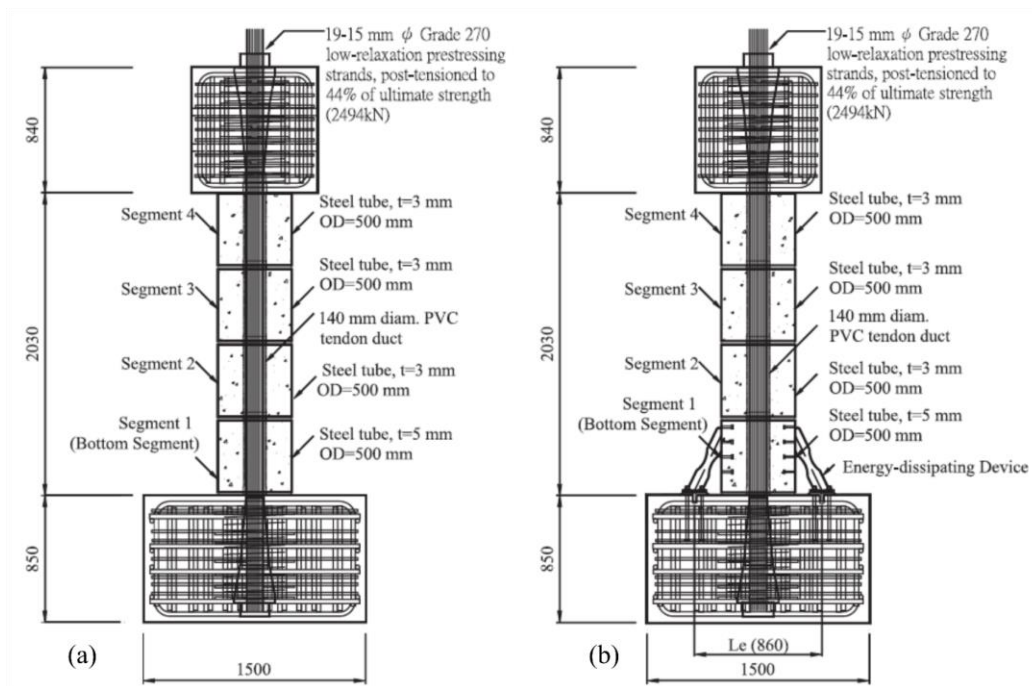


**Figure 2-12: The experimentally tested segmented, CFST bridge columns, fabricated either (a) without energy dissipators or (b) with dissipators (Chou and Chen 2006).**

Columns consisted of four segmental, 20-inch, diameter CFSTs which were connected via a post-tensioned axial duct and were designed to allow for rocking at the foundation interface, and first and second segment interface. Two reduced steel plate (RSP) stiffeners were used as energy

dissipating devices and included shear studs within the base CFST segment to improve force transfer between the RSP stiffeners and internal, CFST concrete. A target drift of 6% was used in the displacement history of the tested columns. Results indicate that self-centering effects were observed in each tested specimen as well as strength and ductility objectives for each column being achieved. The inclusion of external energy dissipators increased the cumulative energy dissipation by 20% compared to that of specimen without any dissipaters, demonstrating the successful achievement of this performance-based objective (Chou and Chen, 2006).

### **3.0 Analytical Modeling of CFST Columns Under Seismic Loadings**

This chapter gives a detailed description of the numerical modeling procedure performed in this study. First, an overview of the numerical modeling procedure of CFST columns is presented with a detailed discussion of the non-linear constitutive models and interaction definitions that were used. Next, an experimentally tested, reference specimen is introduced, and the numerical results developed of the reference specimen are compared to its experimental data to provide validation of the modeling approach. Finally, the methodology used to numerically, simulate earthquake damage in CFST columns prior to repair is introduced.

#### **3.1 Numerical Model Overview**

Extensive numerical investigations have been performed previously (Stephens, 2016; Zhu et al., 2017) to evaluate the behavior of CFSTs that use the ER connection. In these studies, the commercially available, finite element formulation ABAQUS (ABAQUS, 2017) was used to perform non-linear analyses. A similar numerical approach using ABAQUS was adopted here.

The modeled geometry of the CFST specimen, depicted in Figures 3-1a to 3-1c, consisted of the steel tube, embedded ring, column concrete, foundation/cap-beam with reinforcing, and grout. Steel reinforcement, located in the adjacent concrete element, was modelled using 2-node truss elements (T3D2 truss elements) while all other parts utilized 3-dimensional, 8-node, solid brick elements with reduced integration (C3D8R elements). As depicted in Figure 3-1b, half-symmetry along the z-axis was adopted to facilitate computation time. Therefore, the boundary

conditions consisted of ABAQUS' z-symmetry boundary condition as well as a fixed boundary constraint applied to the base of the foundation. The loading protocol consisted of a constant axial applied at the center of the CFST column with a lateral, displacement loading applied at the top of the column.

To further aid in model efficiency, a varying mesh density approach depicted in Figure 3-1c was adopted where areas of analytical importance (i.e. the plastic hinge region) had a finer mesh density compared to less important regions (i.e. the foundation/cap-beam). A mesh 1 x 1-inch was used for the grout, steel, and concrete of the CFST located within the connection pocket. The plastic hinge region was assumed to range from the base of the foundation to a maximum height of 6-inches, with a failure location at 2-inches above the adjoined concrete element based on previous experimental observation. Within this area, the steel and concrete elements were sized using a mesh size of 1 x 1/4-inches. Above the plastic hinge region, the CFST was divided into three, equal sections with increasing mesh sizes along the height; these sizes were 1 x 1-inch, 1 x 2-inches, and 1 x 3-inches, respectively. The foundation/cap-beam was meshed using 1 x 2-inch element to also improve efficiency.

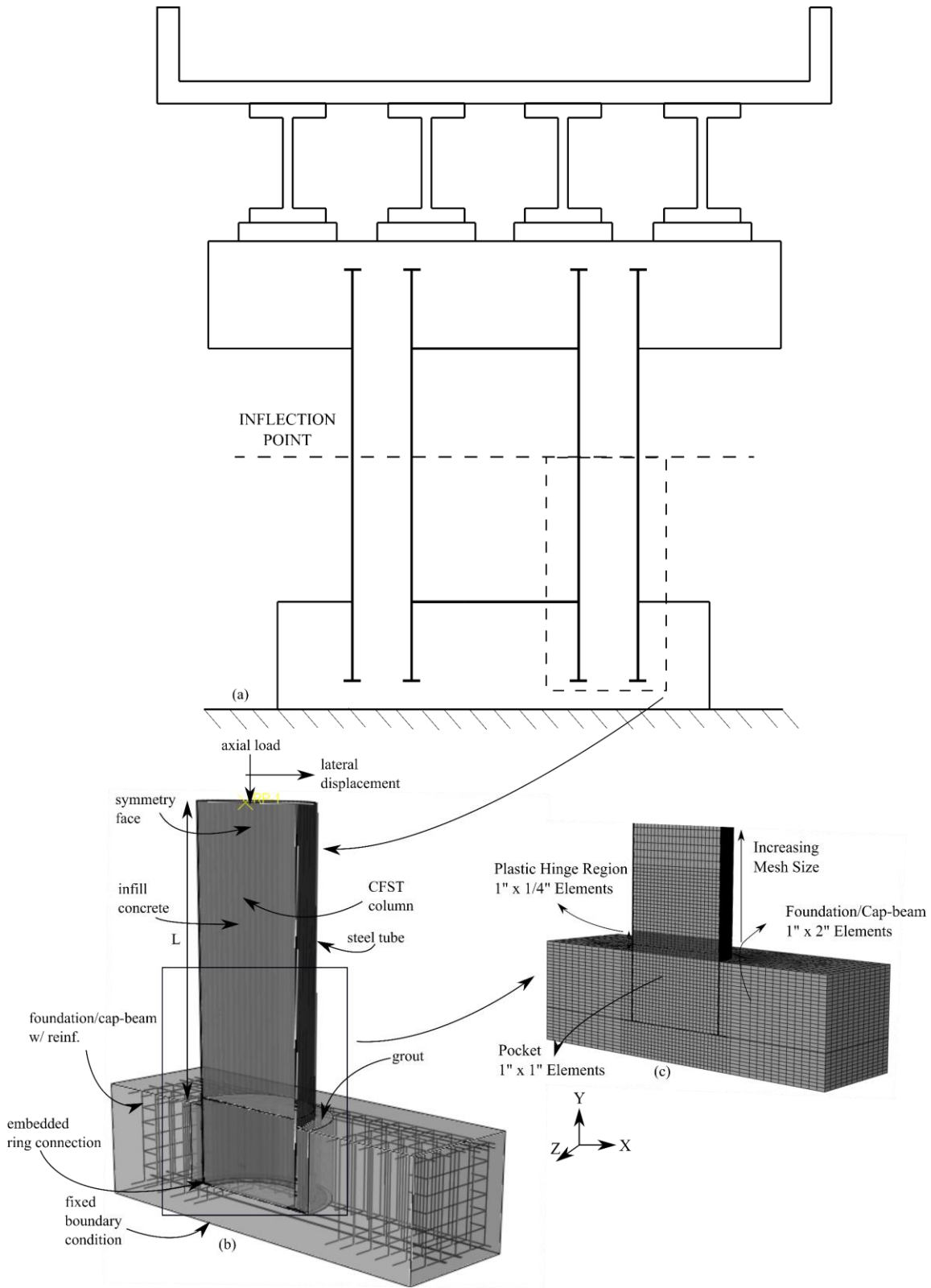


**Figure 3-1: (a) Typical bridge containing CFST columns with a depiction of the (b) ABAQUS model overview and (c) varying mesh densities.**

### 3.1.1 Non-linear Material Properties and Interaction Definitions

Material non-linearity was incorporated using built-in constitutive models in ABAQUS. The non-linear behavior of the steel tube was captured using a quad-linear, stress-strain curve simplification with isotropic hardening. It was assumed that a stress plateau would initiate at  $\epsilon_y$  until the onset of strain hardening, at a strain value of  $\epsilon_{sh}$ . Strain hardening then propagates until a strain value of  $3\epsilon_{sh}$ , where a second stress plateau occurs until a stress and strain combination of  $f_u$  and  $4\epsilon_{sh}$  respectively. Similarly, the reinforcing steel followed a simplified, tri-linear stress-strain curve with strain hardening occurring until failure at an ultimate strain of  $4\epsilon_{sh}$ . The stress-strain curves of concrete, the steel tube, and steel reinforcing are summarized in Figures 3-2a, 3-2b, and 3-2c respectively.

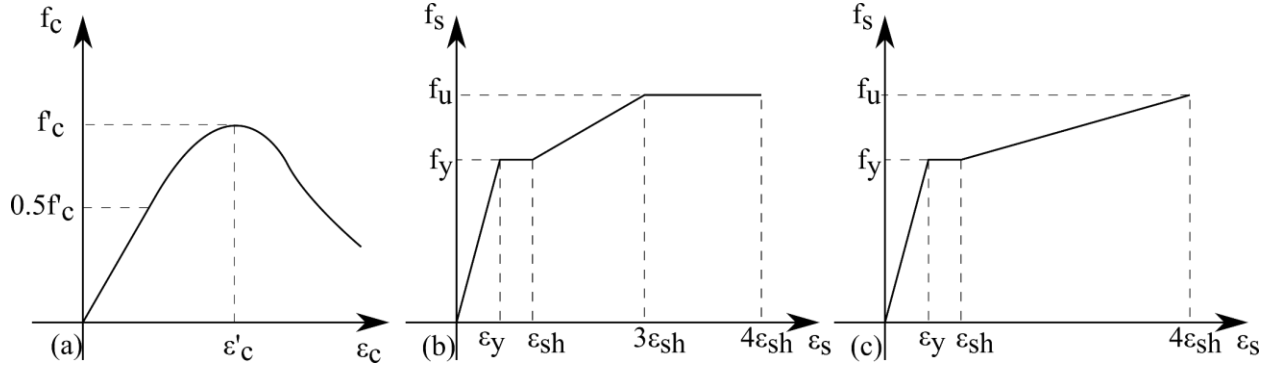


**Figure 3-2: Non-linear stress-strain curves for (a) concrete, (b) the steel tube, and (c) reinforcing steel.**

Concrete inelasticity was modeled using a concrete damaged plasticity (CDP) model. The CDP model can capture the quasi-brittle nature of concrete, and tensile and compressive stiffness reduction under reverse, cyclic loadings (Zhu et al., 2017). To define the CDP constitutive model, ABAQUS requires the input of the elastic material parameters, compressive and tensile stress-

strain data, plasticity parameters (Table 1), and compression and tension damage parameters. The elastic modulus was calculated directly from the compressive strength,  $f'_c$  while a Poisson's ratio,  $\nu$ , was assumed to be 0.20 for all concrete elements. The compressive stress-strain relation for the column concrete, grout, and foundation specimens were defined based on typical compressive strength curves provided in Zhu et al. (2017). Tensile, stress-strain curves were developed for each concrete part based on the Hsu and Mo (2010) tensile-strain relation, which assumes a linear stress-strain relation up until cracking stress,  $f_{cr}$ , is equal to  $7\sqrt{f'_c}$ . A softening, stress-strain relation was defined using the function provided in (3-1) where  $\epsilon_{cr}$  is the cracking strain (Hsu and Mo, 2010).

$$f'_{cr} = f_{cr} \left( \frac{\epsilon_{cr}}{\epsilon} \right)^{0.4} \quad (3-1)$$

The plasticity parameters required to define CDP consists of five parameters including: (1) dilation angle (2) flow potential eccentricity, (3) compressive strength ratio under biaxial loading to uniaxial loading ( $f_{b0} / f_{c0}$ ), (4), ratio of the second stress invariant on the tensile meridian to the compressive meridian (K), and (5) the viscosity parameter. Values of these plasticity parameters implemented here are summarized in Table 1 and were selected based on that previously implemented in literature (Zhu et al. 2017) However, the dilation angle varied between concrete elements as it predicts the brittle or ductile response under loadings; low values are used for brittle responses, while high values predict a more ductile response. The viscosity parameter is widely known to have noticeable effects on computational time with a tradeoff in accuracy. This parameter allows for a fictitious, concrete tangent stiffness during the softening regime at very small, time increments, to facilitate potential convergence issues (Demir et al., 2018; Zhu et al., 2017). Under monotonic loadings, Zhu et al. (2017) determined that values of 0.001, 0.005, and

0.01 were within reasonable accuracies where a model using a value of 0.0001, takes roughly 10 times longer to converge than a model using a value of 0.001 (Zhu et al., 2017). A value of 0.005 was used in this study for all CDP model formulations.

**Table 1: Plasticity parameters for CDP model.**

Dilation Angle			Eccentricity	$f_{b0} / f_{c0}$	K	Viscosity Parameter
Column Concrete	Foundation	Grout				
20	20	30	0.1	1.16	0.667	0.005

Damage parameters, referred to as  $d_c$  and  $d_t$  for compressive and tensile damage, respectively, are tabulated, non-decreasing, scalar stiffness degradation variables that are a function of accumulated concrete cracking or crushing strain values. The degraded, elastic stiffness, is depicted as a function of the tensile and compressive damage parameters in Figures 3-3a and 3-3b, respectively (ABAQUS, 2017; Stephens, 2016; V.Chaudhari and A. Chakrabarti, 2012; Zhu et al., 2017).

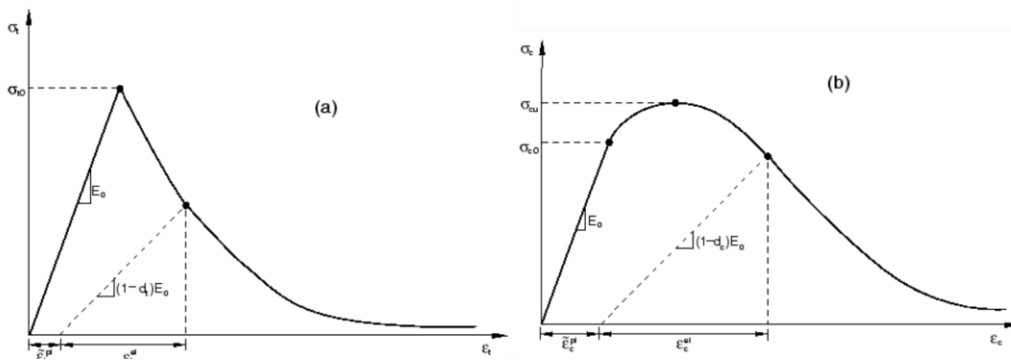


**Figure 3-3: CDP stress-strain curve response of concrete subjected to uniaxial (a) tension and (b) compression (ABAQUS, 2017).**

The CDP model does have some limitations however, especially when the material is subjected to reversed cyclic tension-to-compression cycles. Specifically, the model does not allow for crack closure prior to the development of compression resistance, resulting in a hysteretic response that does not accurately reflect the response of cracked concrete. This limitation can be overcome through the inclusion of the damage parameters ( $d_c$  and  $d_t$ ) as describe above, however computation demand is significantly increased. It has also been noted that the tensile resistance of the concrete fill of the CFST, contributes very little to the overall strength of the connection and often reaches maximum tensile strength before steel tube yielding occurs (Zhu et al., 2017). To improve model efficiency in this study, a “pre-cracking” approach was implemented which includes modeling the infill concrete at the location of maximum rotation as two separate parts in ABAQUS, with a surface-surface contact described between their interfacial surfaces, denoted by Surface 1 and Surface 2 in Figure 3-3. This allows for compressive stresses to still be captured on the closing side of the fill, while simplifying the uplift between parts on the tension side (Zhu et al., 2017). This methodology was implemented in this study by locating the “pre-crack” at a height of 2-inches above the foundation/cap-beam based on prior experimental observation (Stephens, 2016).

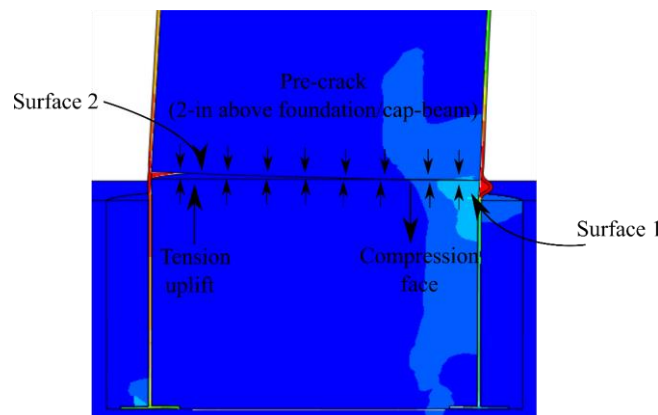


**Figure 3-4: Depiction of the “pre-crack” approach implemented at the plastic hinge of the CFST column.**

A series of interaction and constraint definitions were implemented into the numerical model for the required parts of the CFST specimen. The interfaces between the steel tube and concrete elements (e.g. concrete fill, foundation/cap-beam, or grout) were defined using a contact interaction. The two faces of the concrete fill located at the pre-crack was also defined with a contact interaction. A contact property with tangential and normal behavior definitions were included in the surface-surface interactions; tangential behavior was defined using a penalty friction formulation, while the normal behavior was defined as a hard contact. Friction coefficients between steel and concrete used a value of 0.35 (Zhu et al., 2017) while a value of 0.80 was used between concrete to concrete interactions.

Tie constraints were used between the grout and foundation/cap-beam parts, and exposed base of the infill concrete to the adjoining concrete part. A perfectly embedded constraint was used for modeling the embedment of the steel reinforcement into the foundation/cap-beam. The top of the column was tied to a reference point using a kinematic constraint with displacement degrees of freedom constrained. The axial load and lateral displacement definitions were applied through this reference point as well.

### **3.2 Numerical Validation with Reference Specimen**

The results from a previous investigation (Stephens, 2016) served as the experimental baseline of this study, given its successful hysteretic performance and it exhibiting a ductile failure mode with damage isolated into the CFST column, rather than the foundation/cap-beam element. The sizing of the reference specimen was determined from a design based on using the Laguna De Santa Rosa Bridge near Santa Rosa, California as a prototype. The design procedure consisted of

redesigning the 48-inch diameter, RC bridge columns as equivalent ER, CFST columns of the same strength. An in-depth design procedure is provided in Stephens (2016).

The redesign resulted in the reference specimen utilizing a 53-ksi, API 5L X42 PSL1 grade steel tube with a 24-inch diameter and a ¼-inch wall thickness (i.e. a D/t ratio of 96). As shown in Figure 3-5, the specimen's height was 72-inches from the top of the foundation, which was sized at 76 x 29.75 x 48-inches (L x h x b) and internally reinforced to ensure elastic behavior. The height of the column was terminated at the inflection point to simplify its experimental and numerical construction. The reference specimen was constructed using the grouted connection detail (Figure 2-4) with an embedment length,  $L_e$ , equal to 20-inches, and specific depth,  $L_{pc}$ , equal to 9.75-inches. An inner and outer radius for the ER was taken as 9.75-inches and 14-inches, respectively, or a distance of  $8t$  (2-inches) off of the interior and exterior face of the steel tube. The foundation included a 30-inch diameter pocket to complete the grouted connection. Specimen geometry is summarized in Table 2 while the material strengths, measured on the day of testing, are summarized in Table 3.

The lateral load displacement protocol was based on ATC-24 guidelines (Krawinkler, 1992) specified for steel structures subjected to seismic loadings, which bases a target displacement as a multiple of the initial yield displacement. Peak results indicated that the reference specimen slightly exceeded its plastic moment capacity ( $1.12M_p$ ) of 11,000 k-in as determined from the plastic stress distribution method. The peak moment capacity was recorded at 4.50% drift and, at 8.6% drift, a 20% moment strength degradation was observed.

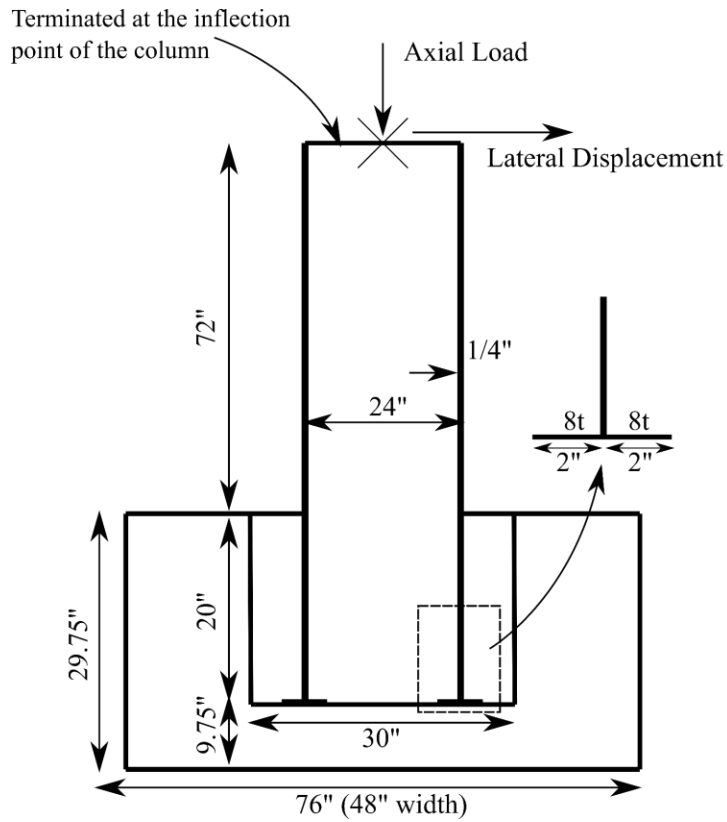


Figure 3-5: Geometric detailing of the CFST reference specimen.

Table 2: Summary of the reference specimen geometry.

$D_t$ (in)	$t_t$ (in)	$L_f$ (in)	$h_f$ (in)	$b_f$ (in)	$L_{col}$ (in)	$L_e$ (in)	$L_{pc}$ (in)
24	0.25	76	29.75	48	72	20	9.75

Table 3: Summary of the reference specimen material properties.

$F_{y,t}$ (ksi)	$F_{u,t}$ (ksi)	$f'_{c,col}$ (ksi)	$f'_{c,grout}$ (ksi)	$f'_{c,f}$ (ksi)
53	68.9	8.3	8.7	10.1

To validate the modeling procedure, a numerical model of the reference specimen was created using the procedure outline in Section 3.1. The modeled utilized a simplified, ATC-24 loading protocol which reduced the number of drift cycles at each target drift. The results of the hysteretic performance of the numerical model are compared against the experimental behavior of the reference specimen in Figure 3-6. In general, the numerical model captures the behavior of the reference specimen. Peak moment capacities at 2, 3 and 5% are similar and the unloading response follows very closely to the experimental response. In addition, outward tube buckling of the steel tube was still successfully captured as illustrated in Figure 3-7a. The model does over predict initial strengths and stiffness, and under predicts strength degradation in the steel tube. This could be contributed to the simplified, loading protocol utilized in the model in comparison to that used in the experiment.

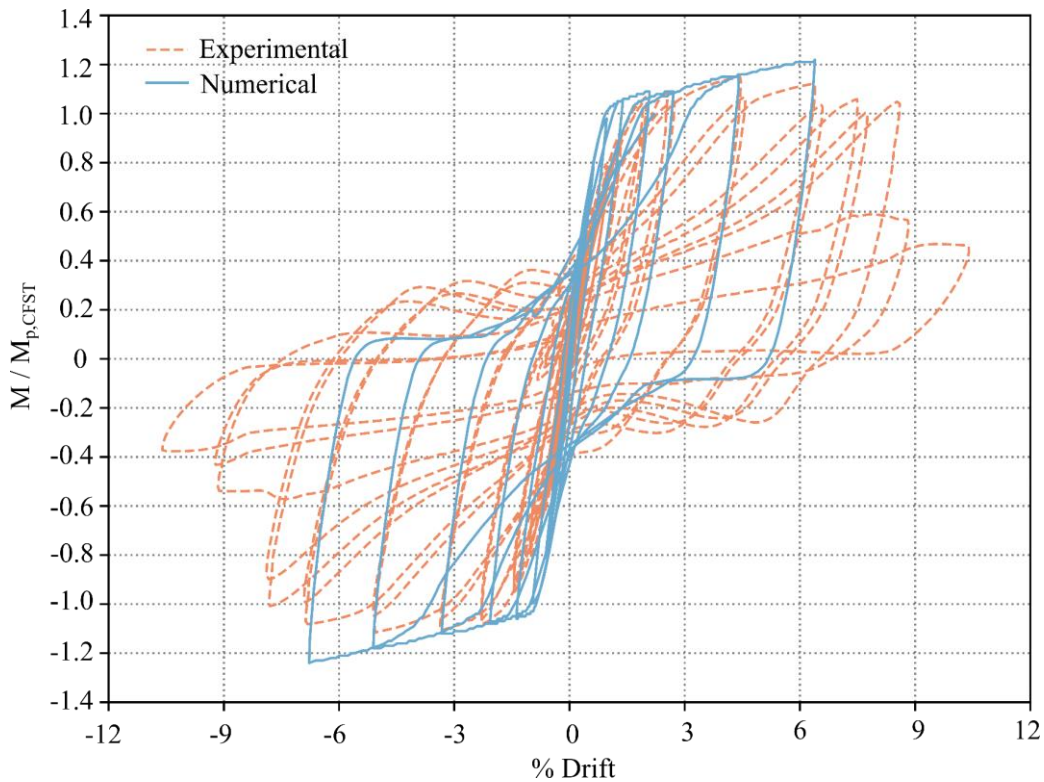


**Figure 3-6: Experimental vs numerical response of the reference specimen.**

### 3.2.1 Modeling Initial Earthquake Damage

Damage of a well-detailed, CFST bridge column subjected to a complete, earthquake loading history, will experience outward tube buckling failure and eventual tube tearing, as depicted in Figure 3-7a. This tube buckling/tearing was accurately captured in the numerical model, as shown in Figure 3-7b, and is subsequently removed in order to simulate earthquake-damage of CFST columns, in ABAQUS models (Figure 3-7c). Based on experimental observation, it was assumed that 1-inch of steel above and below the pre-crack location should be removed, thus creating two separate parts of the steel tube, above and below the damaged region.

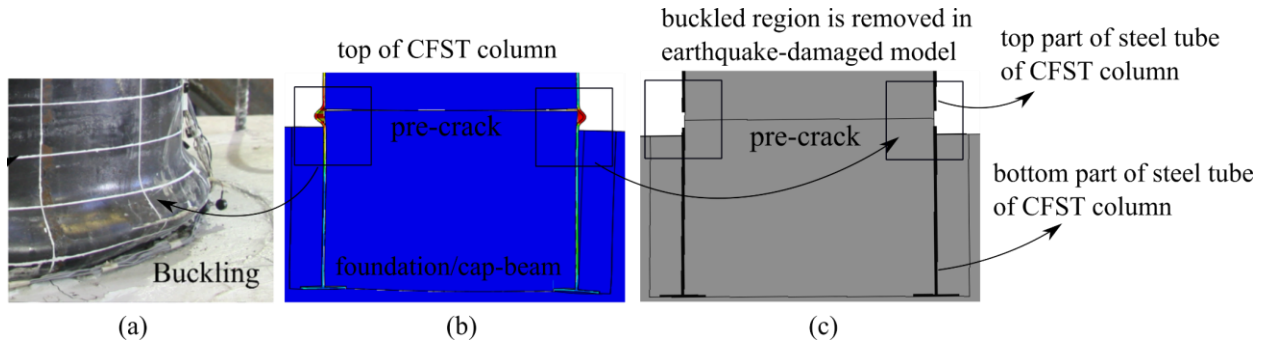


**Figure 3-7: Typical buckling failure captured (a) experimentally and (b) numerically, and (c) its damage-simulation in ABAQUS.**

## **4.0 Plastic Hinge Relocation Repair Strategy**

This chapter covers the design and a limited numerical parameter study of the plastic hinge relocation repair approach. A detailed description of the repair is provided, including an overview of the different force transfer mechanisms (FTM) implemented to transfer force from the column into the foundation/cap-beam as well as the desired performance. After this, a moment-curvature analysis approach used to design the repair is introduced. Finally, a brief description of the numerical model and summary of the limited numerical parametric study conducted on the different FTMs is provided. The parametric study primarily focused on the influence of the different FTM parameters on the lateral load response of the repair, and concludes with a hysteretic comparison of the most successful FTM repair design to that of the undamaged, reference specimen.

### **4.1 Repair Overview**

In the plastic hinge relocation repair strategy, a CFST pedestal is used to encase the damaged region of the original CFST. Steel reinforcement is embedded in the CFST pedestal, and is anchored into the adjacent concrete element using epoxy to transfer the applied moment from the pedestal into the foundation/cap-beam. The design of this reinforcement and pedestal height is covered in more detail in Section 4.2. A steel tube is employed to serve as the formwork for the new concrete, and is left in place post-construction, to provide additional confinement to the repair infill concrete. Unique to this design compared to conventional RC, enlarged sections, is a suite of

force transfer mechanisms (FTMs) that are welded to the CFST to successfully transfer lateral forces from the damaged column into the pedestal. In this study, three force transfer mechanism were evaluated: (1) a welded ring, (2) conventional shear studs, and (3) weld bead strips. These are shown in Figures 4-1a to 4-1c, respectively. The welded ring is similar to the embedded ring connection detail, and can be readily welded to the steel tube of the CFST column using a fillet weld detail. The shear studs proposed for use in this repair are similar to those conventionally used in design to transfer forces between steel and concrete, such as in composite beam structures. These can also be readily attached using a shear stud welding gun. The weld bead FTM consist simply of a strip of weld that is completed in a single pass by the welder.

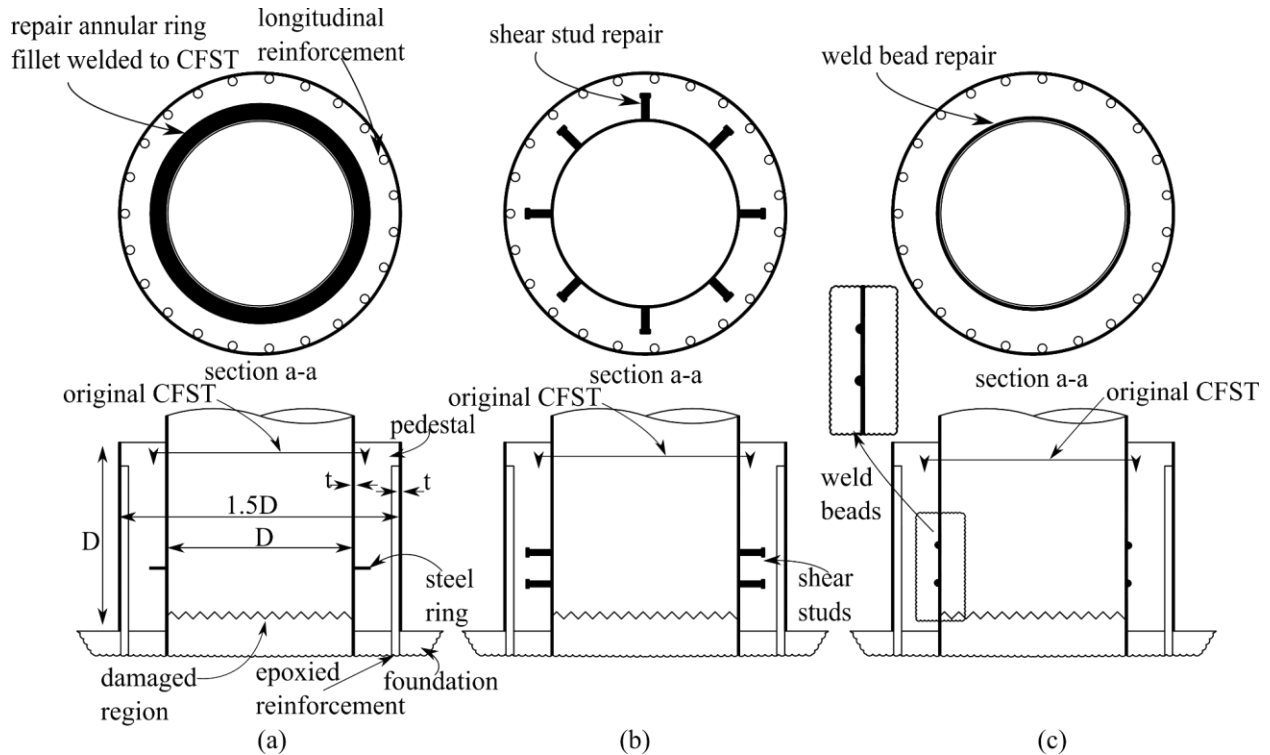


**Figure 4-1: Repair methodologies using (a) welded ring, (b) shear studs, and (c) weld beads**

### **4.1.1 Performance Objectives**

A successful performance of this repair strategy is characterized by shifting the plastic hinge location above the pedestal; this would be demonstrated by the full development of the plastic moment capacity of the CFST at this region as well. Ductility and stiffness restoration are also target objectives for this repair and are assessed by comparing the stiffness and ductility of the repaired CFST column, to the undamaged column's peak behaviors. An additional performance objective was to limit rotation within the repair pedestal. This was assessed based on a rigid body rotation analysis of the system, where under ideal conditions, lateral displacement of the column would be contributed completely from the top of the column to the new plastic hinge region. The pedestal would not exhibit any uplift nor any relative rotation to the foundation/cap-beam. This analysis procedure is covered in more detail in Section 4.4.

## **4.2 Design Procedure**

The purpose of this section is to present a design procedure for designing the size and dimensions of the CFST pedestal. A similar design procedure is provided in (Krish et al., 2018b) for the repair of RC columns. However, in the design procedures provided by Krish et al. (2018a), the original, damaged RC column has internal reinforcement which, depending on their damage, may still contribute to the overall flexural resistance of the repaired section. This is not true for the repair of CFST columns; all flexural resistance in the repaired region is provided by the repair pedestal.

### 4.2.1 Estimating Flexural Demand and Pedestal Height

As previously stated, a main objective of the plastic hinge relocation repair is to develop the original plastic moment capacity of the CFST, directly above the repair pedestal. To achieve this objective, the plastic moment of the CFST must be developed over a shorter, effective column length ( $L' = L - h$ ) resulting in a moment which exceeds the plastic moment capacity of the CFST, at the base of the pedestal. Therefore, additional strengthening of the foundation/cap-beam may be required to prevent foundation failure. (4-1) derives this maximum moment at the base of the pedestal ( $M_r$ ) as a function of the original moment capacity of the CFST ( $M_{CFST}$ ), the length of the column to the inflection point ( $L$ ), and the new, effective length of the repaired column ( $L'$ ). This derivation is also depicted in Figure 4-2 for clarity.

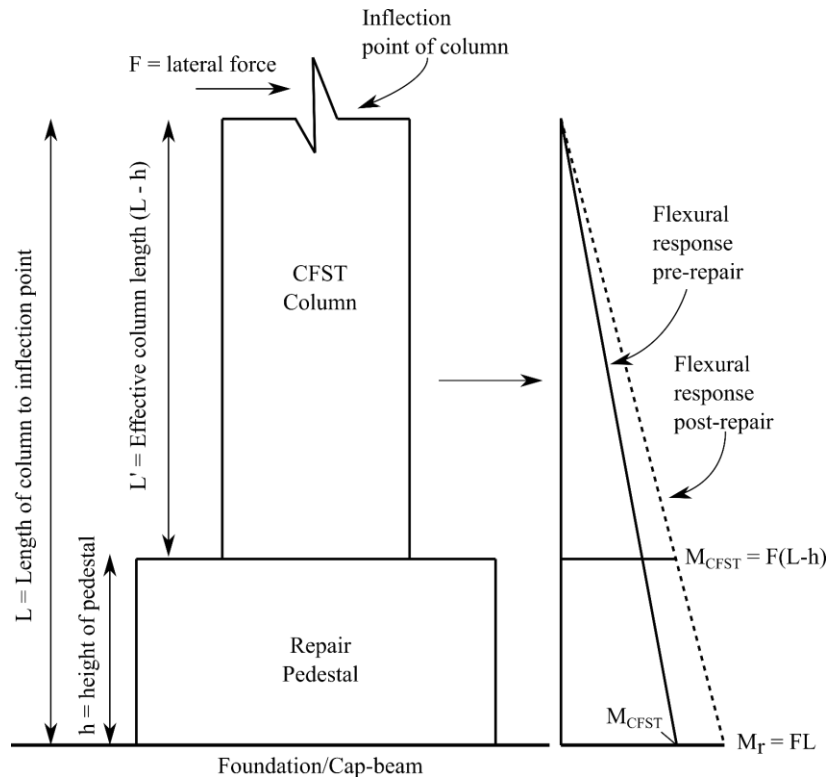


Figure 4-2: Flexural response of the CFST column repair using the plastic hinge relocation method.

$$\frac{L}{L'} = \frac{M_r}{M_{CFST}} \quad (4-1)$$

The height of the pedestal ( $h_r$ ) must also have adequate height in order to provide sufficient concrete to bond to the reinforcement within the repair infill concrete. The American Concrete Institute provides design equation, (4-2), below to provide the required height of concrete ( $H_r$ ) to develop the internal reinforcement, assuming normalweight concrete and uncoated reinforcement sized greater than or equal to a #7 bar, where  $f_y$  is yielding stress (psi) of the reinforcement and  $f'_c$  is the concrete compressive strength (psi) (American Concrete Institute, 2014). Headed reinforcement may also be used to reduce this requirement. Additionally, the required depth of anchorage within the foundation/cap-beam should be determined based on the epoxy supplier.

$$H_r \geq \frac{f_y}{20\sqrt{f'_c}} (d_b) \quad (4-2)$$

There is no direct equation that is available to size the diameter of the repair pedestal, however several performance factors are influenced by this dimension. Intuitively, a larger diameter would create a larger moment-arm for the internal reinforcement, thereby reducing the reinforcing congestion within the pedestal, however there is limitation based on the available footprint on the foundation/cap-beam and the increase strain demand on the reinforcing. Though not explicitly studied in this investigation, the anticipated strain history of the repair reinforcement should be considered; Krist et al. (2018a) provides additional discussions for reference.

## 4.2.2 Estimating Flexural Capacity of the Repair Pedestal

The cross-section of the repair must be designed to elastically resist the applied moment,  $M_r$ , calculated in accordance with EQ (2). Two strength calculation methods were evaluated here: (1) the strain compatibility method and (2) plastic stress distribution method to compare two common moment-curvature analysis procedures. These procedures were elected given that they are commonly employed to calculate the plastic moment capacity of columns subjected to combined axial and bending loads. The nominal material strengths with overstrength, should be used in design as well as confined concrete strengths since the repair infill concrete is confined by the exterior steel tube, as adopted from Krish et al. (2018a). It is assumed that the entire concrete cross-section, including the concrete within the CFST, provides compressive resistance, and the axial load applies a compressive load over the repaired section.

### 1. Strain compatibility method

The strain compatibility method is commonly used to calculate the strength of RC columns subjected to combined axial and bending loadings, and was therefore adopted for this study. Figure 4-3 provides an idealized strain distribution of the cross-section assuming a maximum allowable concrete strain of 0.003 and a linear strain accumulation from this point. A variable, “c”, is used to represent the distance from the extreme concrete compressive fiber to neutral axis and is used to calculate curvature and tensile and compressive forces of the cross-section based on their strain development. The maximum allowable force of the reinforcement is taken as  $F_y A_{\text{bar}}$  and the compressive force within the concrete is taken directly as  $0.95 f'_c A_{\text{concrete}}$ , where the area of concrete subjected to compression is reduced by the area of reinforcement present in this region. The value

of “c” is then iterated on until the combined axial forces are summed to equality, and the resulting resisting moment is calculated with respect to the center of the cross-section.

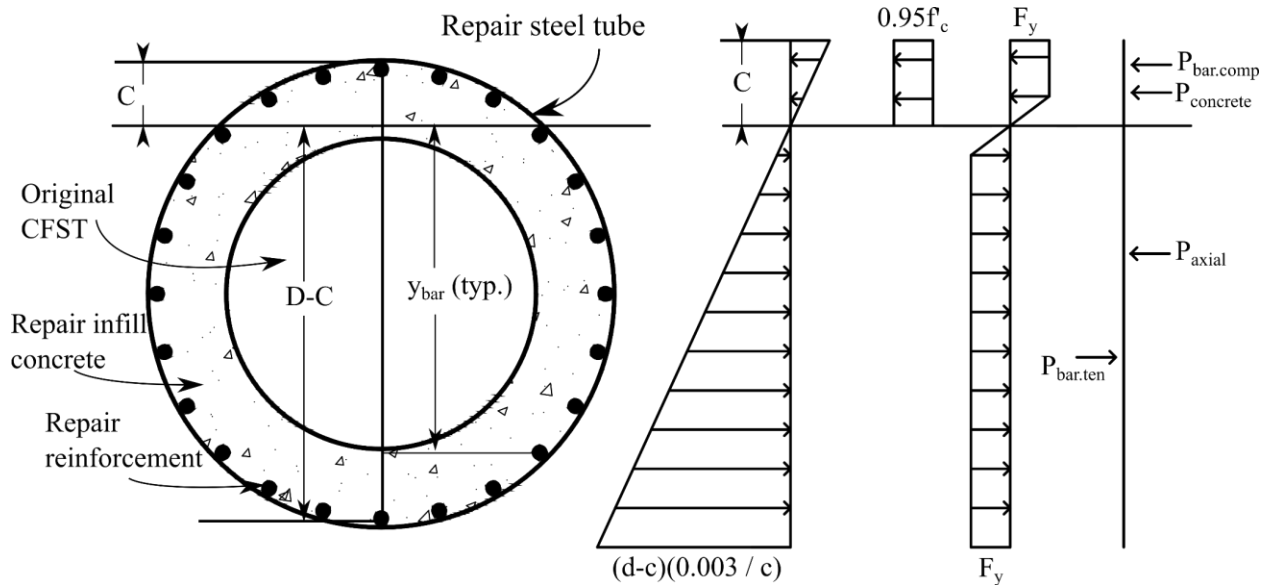
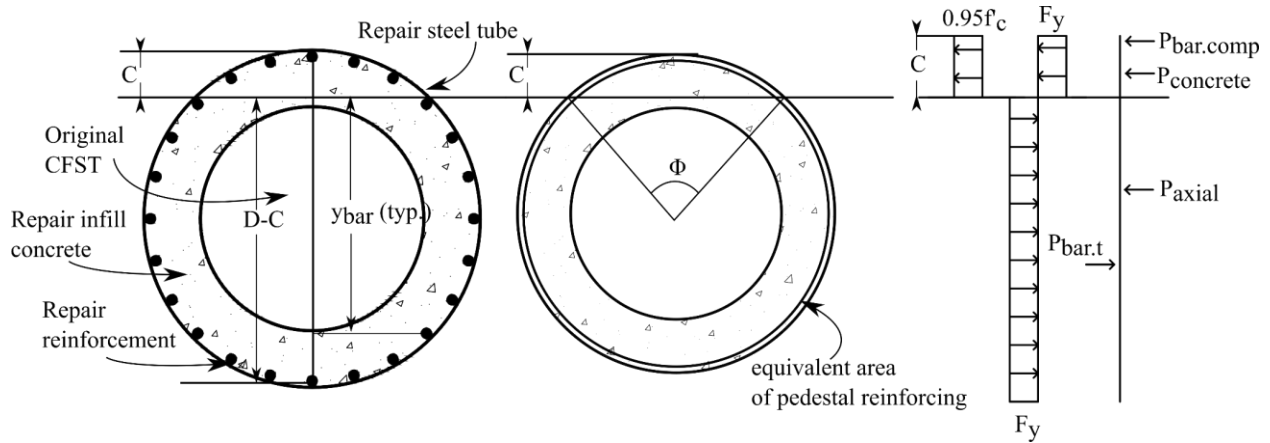


Figure 4-3: Idealized stress-strain curves of the strain compatibility method.

## 2. Plastic stress distribution method

The plastic stress distribution method has recently been recommended to calculate the combined flexural and axial load capacity of CFST columns (Stephens et al., 2016b). The plastic stress distribution method assumes that all steel components achieve their yield stress,  $F_y$ , across the entire cross-section while the internal concrete is assumed to reach a compressive strength of  $0.95f_c$ . This relationship is shown in Figure 4-4. Similar, to the strain compatibility method, the variable “c” is used to represent the extent of the compressive block and to calculate the area of concrete in compression. To simplify calculations, the internal, repair reinforcement is transformed to a concentric, thin-walled tube with equivalent reinforcing area of all of the repair pedestal reinforcement. This allowed for a simplified calculation of the compressive and tensile resisting

area of the repair reinforcement as function of angle,  $\Phi$ . Using these assumptions, the combined forces are summed to equilibrium and the nominal moment capacity is equated with respect to the center of the cross-section.



**Figure 4-4: Idealized stress-strain curves of the plastic stress distribution method.**

Using the design methods outlined above, and engineering judgement based from previous research ((Krish et al., 2018b; Lehman et al., 2001), a plastic hinge relocation repair was developed for the reference specimen. Figure 4-5 provides a reference for the dimensions that depict the repair strategy utilized in this investigation, which are also summarized in Table 5. Appendix A1 provides a detailed procedure for estimating the strength of the repair pedestal, using the two moment-curvature design analyses presented in Section 4.2.2.

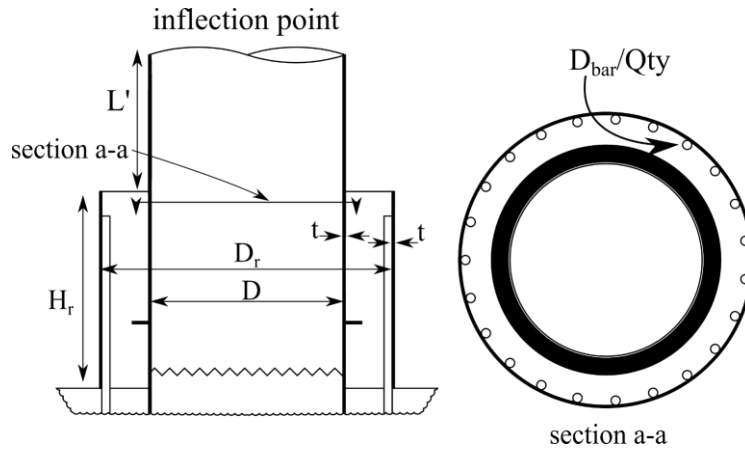


**Figure 4-5: Reference figure for the final design of the plastic hinge relocation repair.**

**Table 4: Plastic hinge relocation repair geometry.**

Repair Strategy	$D_{r,tube}$ (in)	$H_{r,tube}$ (in)	$L'$ (in)	$t$ (in)	$M_{CFST}$ (k-in)	$M_{repair}$ (k-in)	$D_{bar}$ (in)	Qty
PHR	36 (1.5D)	24 (1.0D)	48	0.25	11000	16500	9/8	24

### 4.3 Numerical Model

The analytical modeling procedure for developing the baseline damaged CFST model in ABAQUS uses the methodology presented in Chapter 3.0. To model the plastic hinge relocation repair, components of the pedestal were added including, the repair steel tube, the FTMs, and the repair reinforcement (extending from the foundation/cap-beam into the pedestal). An overview of the model with the pedestal included is provided in Figure 4-6a. All new geometries were modelled as separate parts, again using C3D8R elements to model steel and concrete parts and T3D2 elements to represent the steel reinforcement. The repair concrete used the same concrete damaged

plasticity formulation used for the infill, CFST concrete as described in Section 3.1.1, and the repair steel tube was assumed to have the same inelastic material properties as the steel tube of the column. Repair reinforcement was modeled using nominal strengths accounting for overstrength, assuming a tri-linear, stress-strain curve with yielding at 68-ksi and strain hardening up until an ultimate strength of 90-ksi.

The repair concrete was modeled to include a concentric lip to fill the opened, gap where the steel tube of the original column was removed to simulate damage. Additionally, a recess was included in the repair concrete to provide housing for the weld bead and embedded ring FTMs, and to allow for surface-surface interaction definitions. Figure 4-6b depicts the geometry of the weld bead repair pedestal, with views of the lip and housing previously described. Due to their geometric complexity, a fully embedment constraint was used to simplify the interaction between the shear studs and repair concrete, assuming a perfect bond between the two constituents. A fully embedment constraint was also used to model the reinforcement bond within the repair concrete and foundation/cap-beam, assuming a perfect bond as well. Surface-surface definitions were implemented for the all other steel-concrete interactions including that between the repair steel and concrete, repair concrete and original steel tube, and the interaction of the top of the foundation/cap-beam to the repair pedestal.

As shown in Figure 4-6b, a pre-crack approach was placed at the anticipated failure location of 2-inches above the pedestal and 1 x 1/4-inch elements were utilized within this region to improve computation accuracy. The infill concrete of the original CFST was modeled as three separate parts (above the repaired region, within the pedestal, and within the foundation/cap-beam) using surface-surface interaction definitions to define the interaction properties between them.

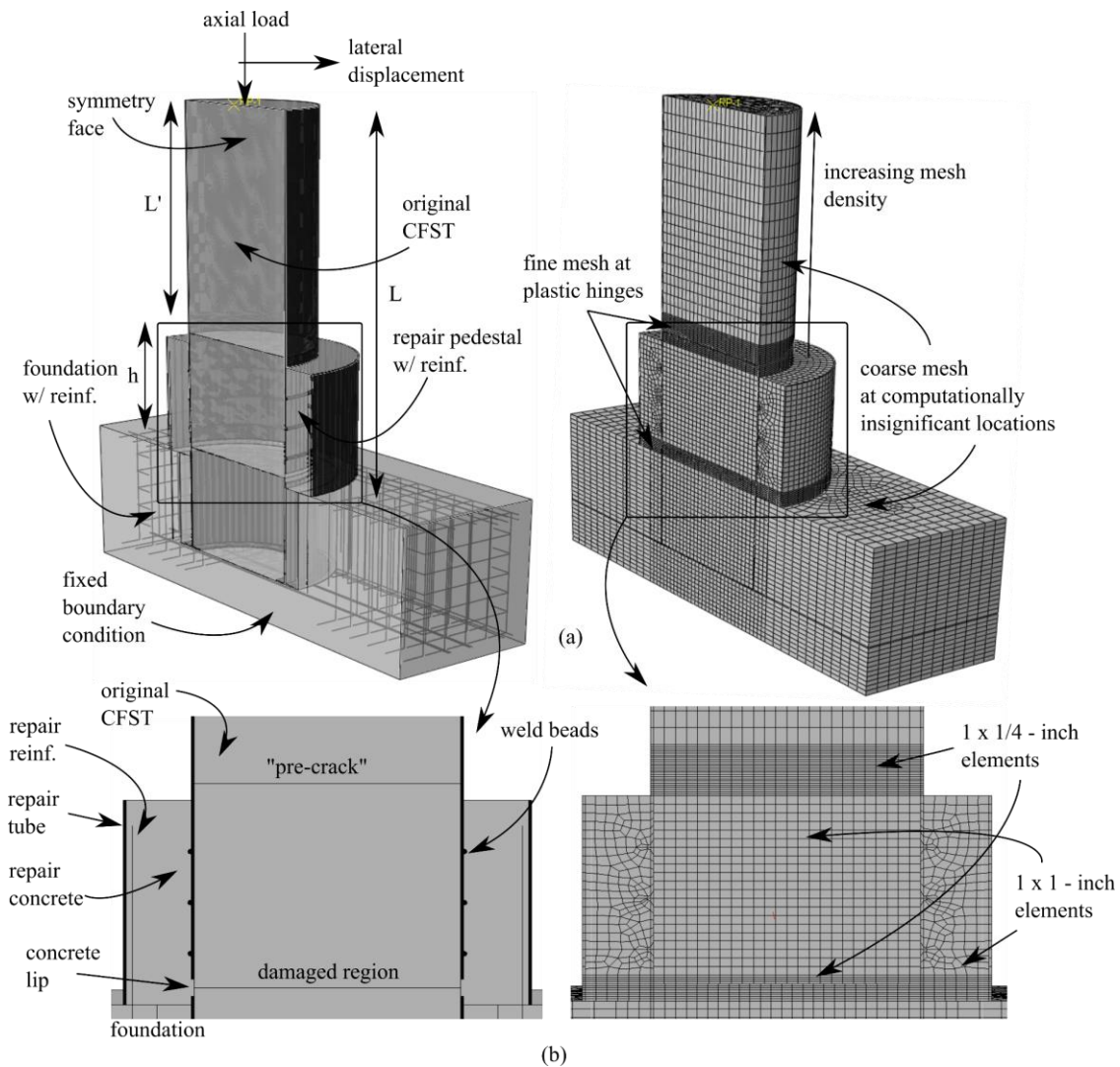


Figure 4-6: (a) Numerical overview of the weld bead plastic hinge repair and (b) views of the pedestal.

### 4.3.1 Parametric Analysis of the FTMs

A limited, parametric study was performed to assess the moment-drift performance of the three FTMs (depicted in Figures 4-1a to 4-1c). The parametric study focused on modifying the dimensions, quantity, and location of components within the FTMs and determining the effect that these parameters had on the stiffness and strength of the repair. The geometry and reinforcement of the pedestal remained constant for all studies; however, one additional study was performed on

the repair tube thickness to evaluate the effect of increasing its thickness. Tables 5 to 7 outline the geometry of each repair evaluated in the parametric study. The nomenclature used to refer to the FTM is as follows: welded ring (ER), shear studs (SS), and weld beads (WB) with the trailing details showing the geometry ( $8t = 8$  times tube thickness) and quantity ( $x2 =$  two rows) used in the analysis. The extruded length of the welded ring as measured from the face of the original CFST was taken as  $8t$ , where  $t$  is the tube thickness. Shear stud dimensions were sized from a common supplier where it was assumed that 8 total shear studs (per row) would provide adequate force transfer. Weld beads were sized for ease of construction as the maximum allowable weld size that can be performed in one pass was utilized, as determined from AISC Steel Construction Manual (American Society of Civil Engineers, 2011)

**Table 5: Summary of ER parameters.**

Name	Description	Image (pedestal not included)
ER-8t	$h_r = 1/3D = 8\text{-inch}$ $w_r = 8t_t = 2\text{-inch}$ $t_r = t_t = 1/4\text{-inch}$	
ER-4t	$h_r = 1/3D = 8\text{-inch}$ $w_r = 4t_t = 1\text{-inch}$ $t_r = 2t_t = 1/2\text{-inch}$	
ER-2x4t	$h_{r1} = 2/3D = 16\text{-inch}$ $h_{r2} = 1/3D = 8\text{-inch}$ $w_r = 4t_t = 1\text{-inch}$ $t_r = 2t_t = 1/2\text{-inch}$	

**Table 6: Summary of SS parameters.**

Name	Description	Image (pedestal not included)
SS-x2	$h_{ss} = 1/3D = 8\text{-inch}$ $w_{ss} = 3\text{-}1/8\text{-inch}$ $t_s = 3/4\text{-inch}$ $t_h = 1\text{-}1/4\text{-inch}$	
S-x4	$h_{ss1} = 2/3D = 16\text{-inch}$ $h_{ss2} = 1/3D = 8\text{-inch}$ $w_{ss} = 3\text{-}1/8\text{-inch}$ $t_s = 3/4\text{-inch}$ $t_h = 1\text{-}1/4\text{-inch}$	

**Table 7: Summary of WB parameters.**

Name	Description	Image (pedestal not included)
WB-x2	$h_{wb} = 1/3D = 8\text{-inch}$ $w_{wb} = 5/16\text{-inch}$	
WB-x3	$h_{wb1} = 3/4D = 18\text{-inch}$ $h_{wb2} = 1/2D = 12\text{-inch}$ $h_{wb3} = 1/4D = 6\text{-inch}$ $w_{wb} = 5/16\text{-inch}$	
WB-x3-1	$h_{wb1} = 3/4D = 18\text{-inch}$ $h_{wb2} = 1/2D = 12\text{-inch}$ $h_{wb3} = 1/4D = 6\text{-inch}$ $w_{wb} = 5/16\text{-inch}$ $t_t = 3t_t = 3/4\text{-inch}$	

## 4.4 Analytical Results

The performance of each repair was evaluated using a monotonic loading protocol with a target drift of 5% measured from the top of the column to the top of the pedestal ( $L'$ ). The stiffness, strength, and contribution of pedestal rotation were used to quantify the performance of the various repair geometries. The results for each repair are summarized in Table 8, and a detailed description of the behavior of each repair is given in the following sections. Pedestal rotation was evaluated to determine the effectiveness of the different FTMs in creating two isolated systems (i.e. the pedestal and the original column) where in ideal conditions, the pedestal would remain rigid with zero contribution to the overall drift. To evaluate the rotation contributions of the pedestal and CFST to the total rotation, the individual displacements were recorded at the top of the pedestal and top of the column as indicated in Figure 4-7. The rotation contributions were then determined by dividing the rotation of each individual component by the total rotation ( $\theta_{ped}/\theta_{tot}$  and  $\theta_{CFST}/\theta_{tot}$  for the pedestal and CFST respectively).

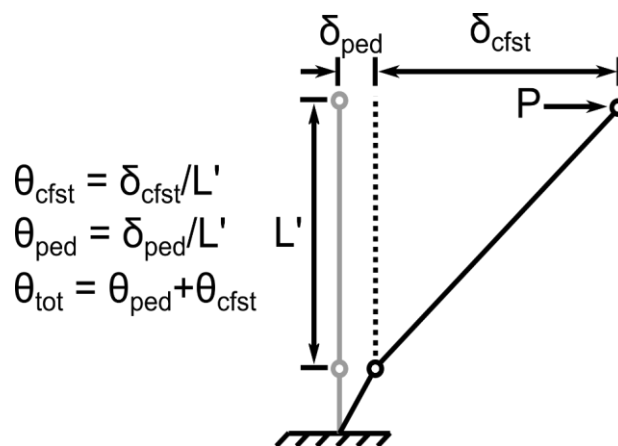


Figure 4-7: Idealized rigid body rotation of the plastic hinge repair strategy.

**Table 8: Summary of FTM parameteric study**

FTM	Name	$M_{max}/M_{p,CFST}$	$\theta_{ped}/\theta_{tot}$ (%)	$\theta_{cfst}/\theta_{tot}$ (%)
Welded Ring	ER-8t	1.06	26.3	73.7
	ER-4t	1.11	24.0	76.0
	ER-2x4t	1.15	20.8	79.2
Shear Studs	SS-x2	1.12	25.5	74.5
	SS-x4	1.15	19.6	80.4
Weld Beads	WB-x2	1.10	24.5	75.5
	WB-x3	1.22	21.4	78.6
	WB-x3-1	1.21	16.1	83.9

### 1. Welded Ring

Three, monotonic moment-drift analyses were performed for the welded ring FTM. These included, (1) 8t sized ring (extruded from side of original CFST), with thickness  $t$  (ER-8t), (2) 4t sized ring with thickness,  $2t$  (ER-4t), and (3) two rows of the 4t sized ring with thickness,  $2t$  (ER-2x4t) as summarized in Figure 4-8a. A moment-drift comparison is shown in Figure 4-8b, while the rigid-body rotation analysis results are shown in Figure 4-8c. The peak moment capacity normalized to the original plastic moment capacity of CFST, and column/pedestal contributions at peak drift are shown in Table 8. Figures 4-9a to 4-9c and Figures 4-10a to 4-10c show comparisons of the stress distribution for steel and concrete, respectively. Results are shown at 4% drift for each figure for comparison, and concrete stresses are compared to the compressive strength of the column (8.3-ksi).

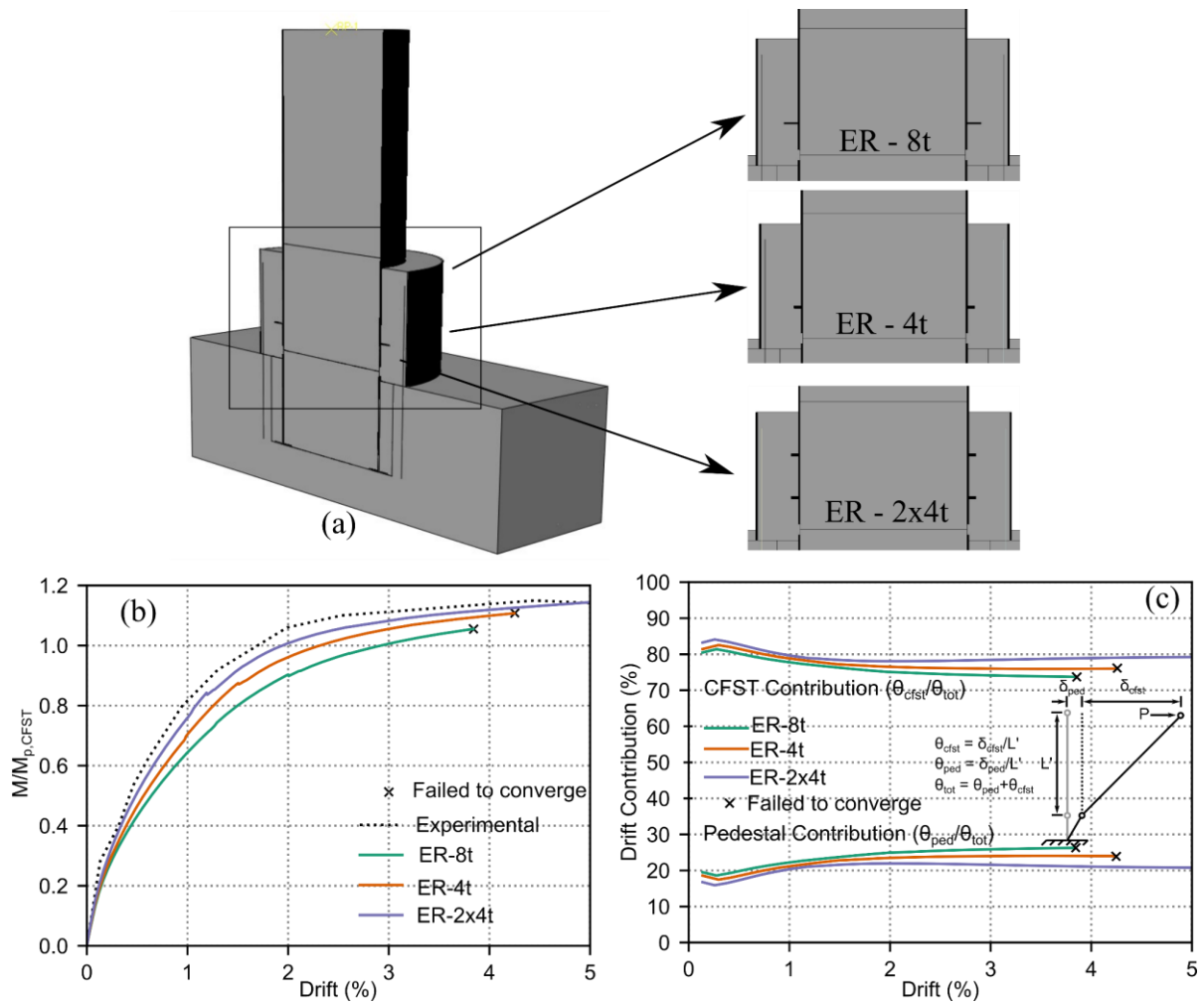


Figure 4-8: Depiction of the (a) overview of ER, FTM repairs, (b) moment-drift response, and (c) rigid-body rotation.

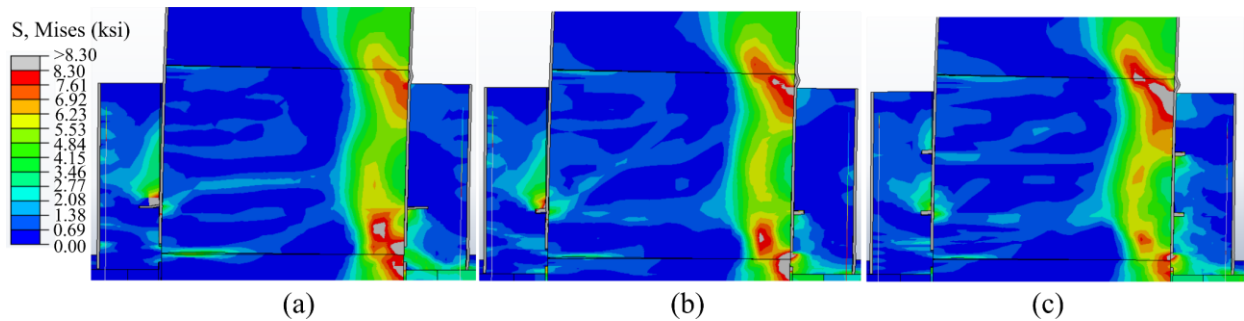
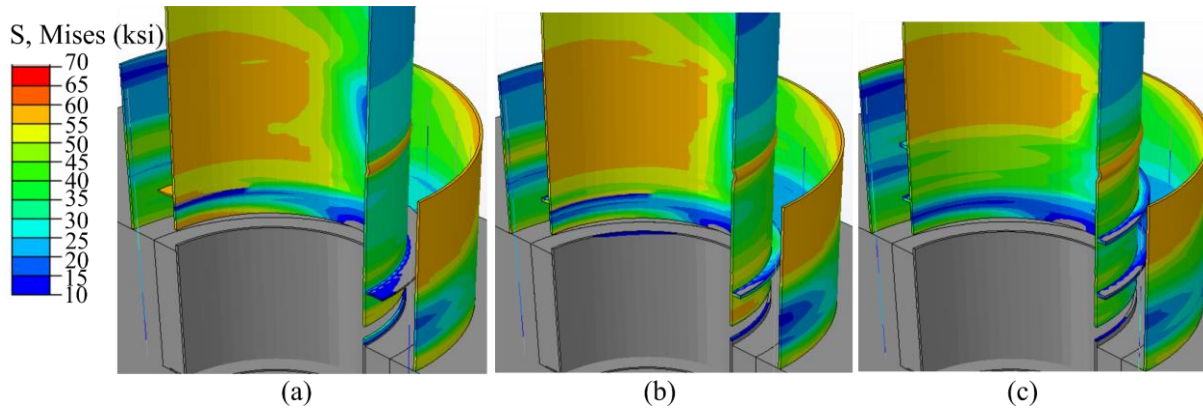


Figure 4-9: Concrete stress concentration at 4% drift for repair (a) ER-8t, (b) ER-4t, and (c) ER-2x4t.



**Figure 4-10: Steel stress concentration at 4% drift for repair (a) ER-8t, (b) ER-4t, and (c) ER-2x4t where the concrete of the pedestal and CFST are not shown for clarity.**

All welded ring repairs achieved strength objectives to exceed the original plastic moment of the CFST, however each repair failed to redevelop the original column stiffness. As shown in Figures 4-8b and 4-8c, the thickness and projection length of the ring have a significant impact on the moment-drift and rigid-body rotation performance. A shorter projection length and thicker ring, improves stiffness and strength, as in cases ER-4t and ER-2x4t, due to a less rigid-body rotation contribution of the CFST within the pedestal and inelastic deformation of the FTM, as compared to ER-8t. Figures 4-9a and 4-10a, highlights this as higher stress concentrations and inelastic deformation can be seen around the projected ring compared to Figures 4-9b and 4-9c, and Figures 4-10b and 4-10c of the more rigid, welded rings. Furthermore, there is a noticeable movement in the location of the compressive concrete stress concentrations in the infill concrete from the original damaged region (in ER-8t), to the interface between the top of the pedestal and CFST (in ER-2x4t). This is due to a greater pedestal rotation in ER-8t compared to a more isolated, CFST rotation above the pedestal in ER-4t and ER-2x4t. Adding an additional row of welded rings along the pedestal as for case ER-2x4t, also has noticeable improvement to strength and stiffness as force transfer from the CFST to repair pedestal greatly improves when comparing Figures 4-9b

and 4-9c. In doing so, this appears to alleviate stress buildup in the original steel tube of the column, as there is continuous stress reduction on the tension side of the CFST when moving from Figures 4-10a to 4-10c.

## **2. Shear Studs**

Two monotonic drift analyses were performed for the shear stud repair configuration including the use of (1) two rows of shear studs (SS-x2) or (2) four rows of shear studs (SS-x4), as shown in Figure 4-11a. Figure 4-11b depicts the moment-drift response and Figure 4-11c results of the rigid-body rotation analysis for both configurations. As can be seen in the figures, each repair method failed to regain the original stiffness, though strength and ductility objectives were achieved. Rigid-body rotation in the pedestal appeared to improve with the addition of two more rows at the top of the pedestal. This also improved the stiffness and strength response. Figures 4-12a and 4-12b, and Figures 4-13a and 4-13b, show the stress accumulation at 4% drift within the steel and concrete elements, respectively.

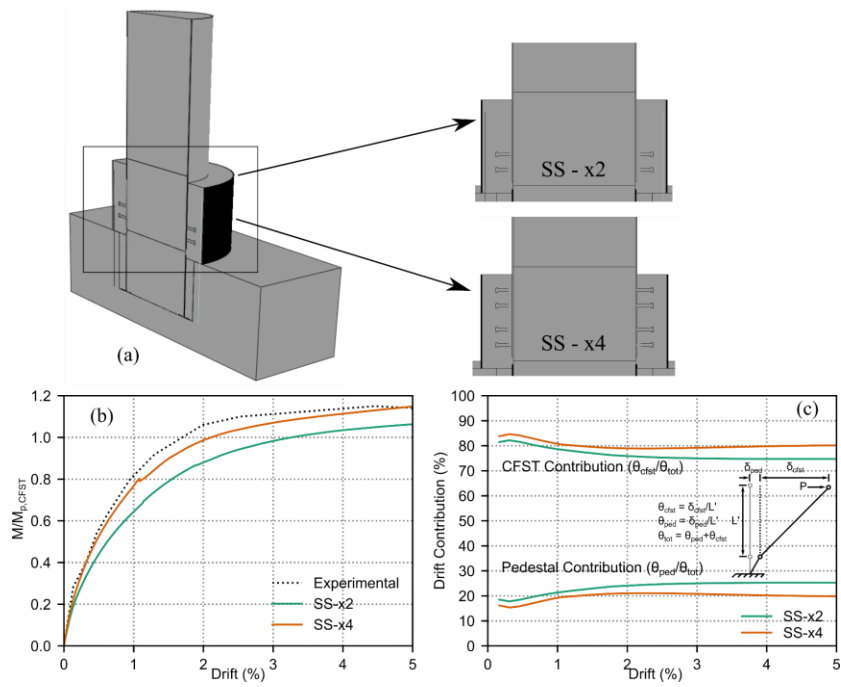


Figure 4-11: (a) Overview of the shear stud repair method with depiction of its (b) moment-drift and (b) rigid-body rotation response

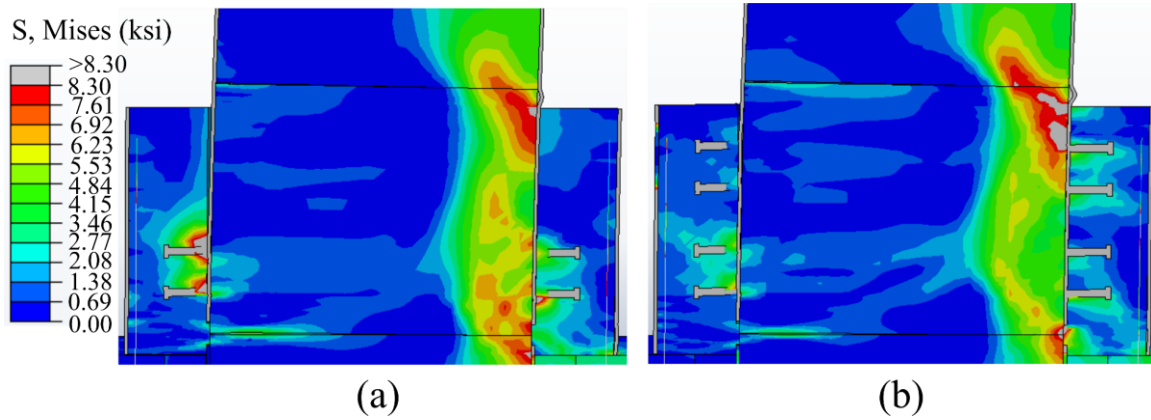
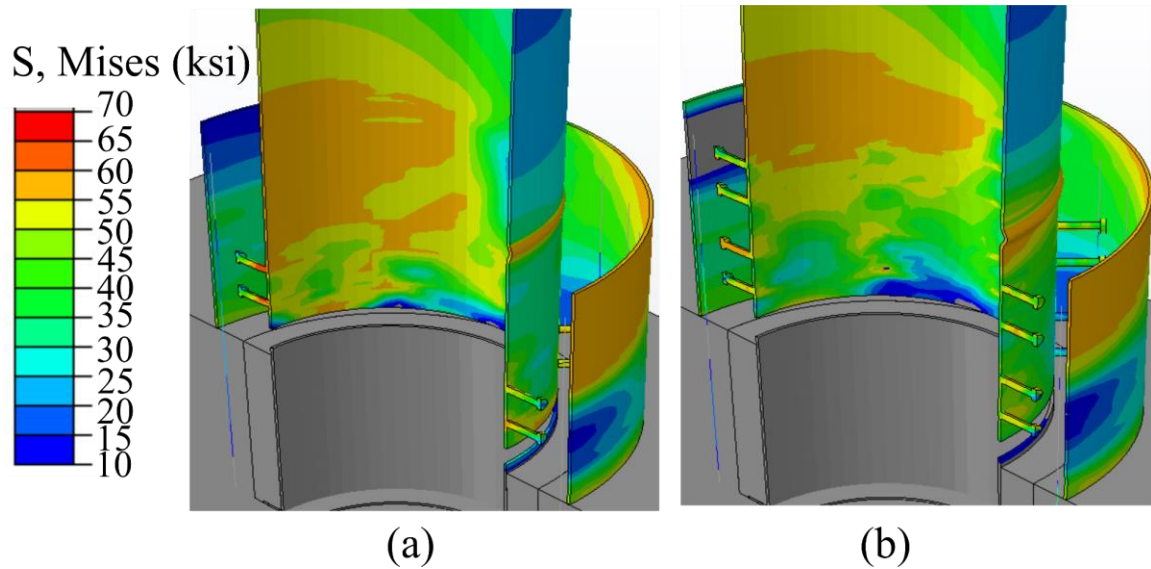


Figure 4-12: Concrete stress concentration at 4% drift for repair (a) SS-x2 and (b) SS-x4.



**Figure 4-13: Steel stress concentration at 4% drift for repair (a) SS-x2 and (b) SS-x4 where the concrete of the pedestal and CFST are not shown for clarity.**

The use of shear studs appeared to be a promising option for developing the strength of the repair, though additional shear studs are required along the height of the pedestal to fully develop stiffness. Furthermore, additional shear studs helped to alleviate concrete stress concentrations at their connection interfaces, as illustrated in Figures 4-12a and 4-12b. However, the distribution of concrete stress appeared to remain relatively the same along the addition regardless of the number of shear studs present. Steel stress within the original CFST was reduced with additional shear studs present and greatly improved stress buildup in the shear studs located on the tension side of the pedestal, particularly those closest to the foundation. It also appears that the top row of shear studs did not exhibit high stress accumulation which may be contributed to a reduction in rotation in the pedestal. It should be noted that the deformation of the shear studs, though they are around the same projection length as the ER, FTM in ER-8t, did not appear to be significant. This could be contributed to the use of an embedment constraint, rather than at surface-surface interaction to define the interaction between the shear studs and repair concrete.

### 3. Weld Beads

Three weld bead configurations were evaluated in this study – (1) two strips of weld beads (WB-x2), (2) three strips (WB-x3), and three strips, with a repair tube thickness of  $3t$  (WB-x3-1). Figure 4-14a illustrates these three repair methods and Figure 4-14b and 4-14c show the resulting moment-drift response and rigid-body rotation response, respectively. For WB-x3 and WB-x3-1, strength and stiffness objectives were achieved, where both had a peak moment capacity of  $1.20 M/M_p$ . WB-x2 however, failed to reach the stiffness and ductility objectives, and performed worse in terms of its rigid-body rotation, with a higher rotation contribution from the pedestal. Figures 4-15a and 4-15b, and 4-16a and 4-16b show the stress distribution of concrete and steel, respectively, at approximately 4% drift. Figures 4-15c and 4-16c are shown at the maximum drift achieved for WB-x3-1 which is 3.30% drift.

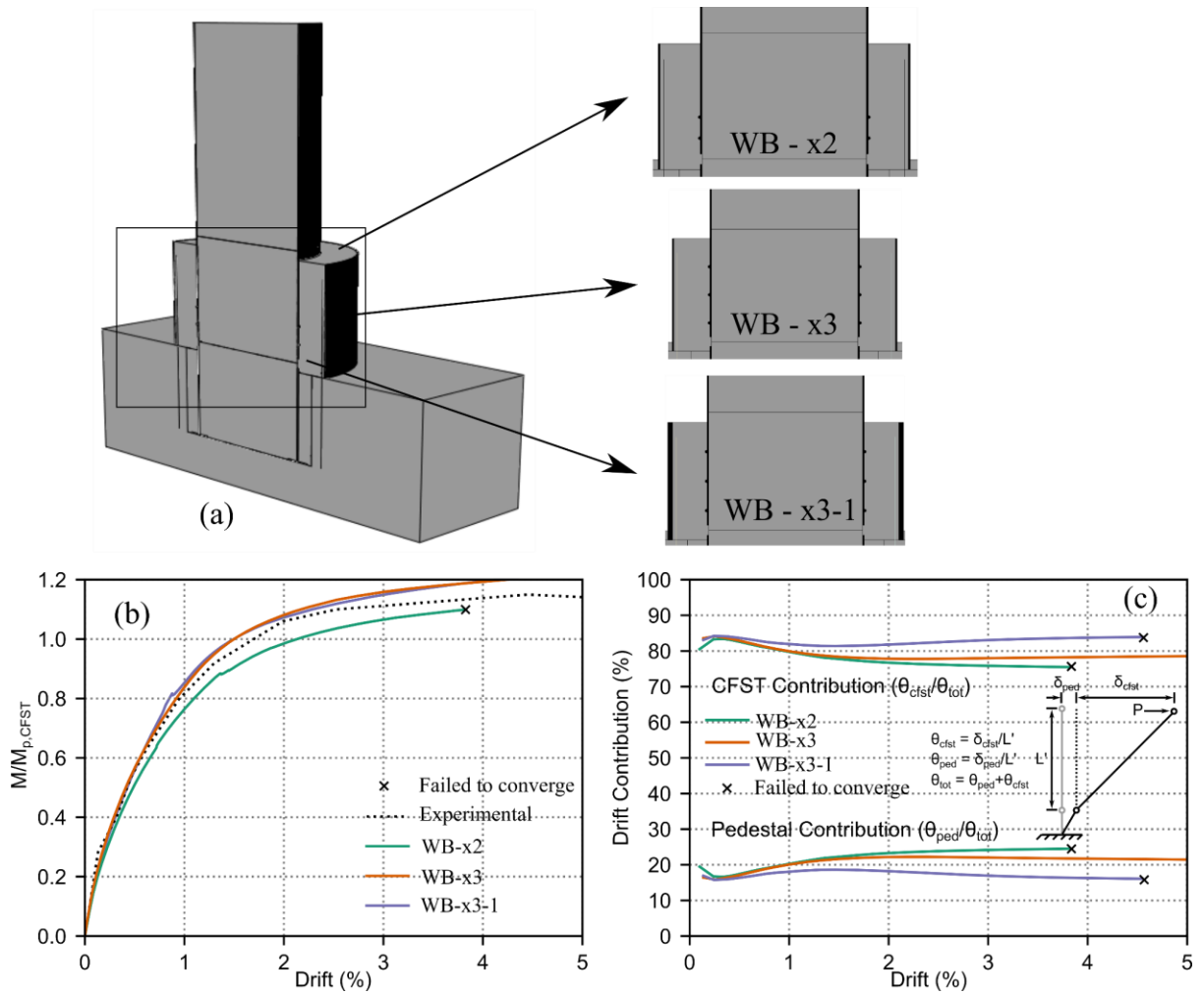


Figure 4-14: Depiction of the (a) overview of the weld bead repair and its (b) moment-drift and (c) rigid-body rotation response.

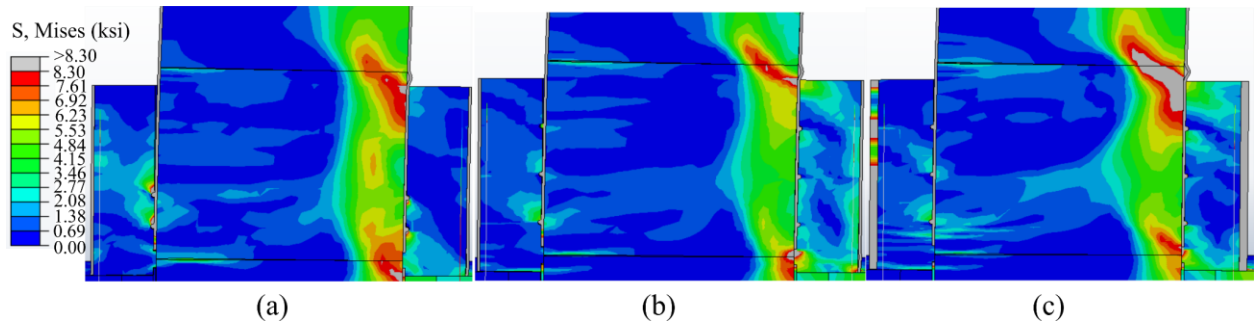
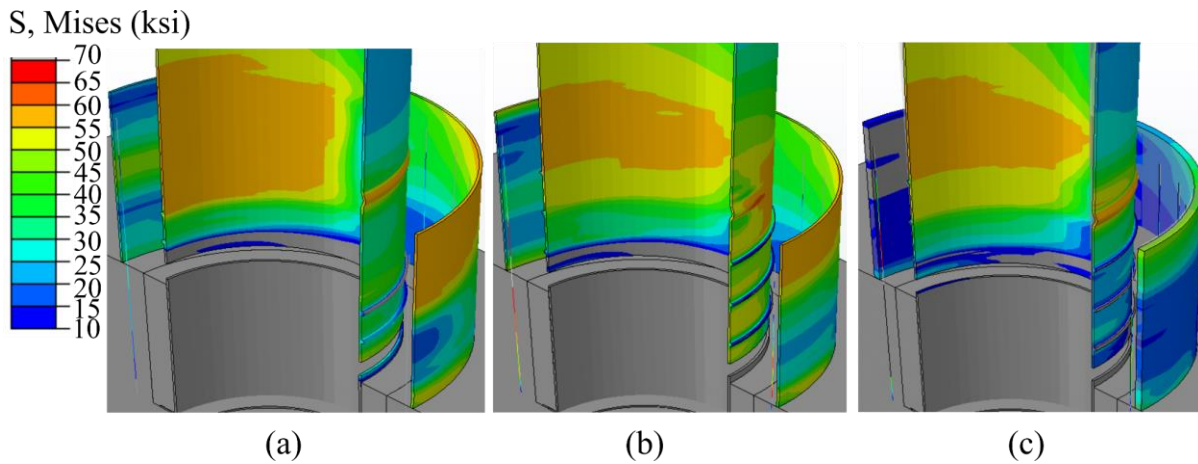


Figure 4-15: Concrete stress concentration at 4% drift for repair (a) WB-x2 and (b) WB-x3 and at 3.30% drift of (c) WB-x3-1.



**Figure 4-16: Steel stress concentration at 4% drift for repair (a) WB-x2 and (b) WB-x3 and at 3.30% drift of (c) WB-x3-1 where the concrete of the pedestal and CFST are not shown for clarity.**

In general, the weld bead repair performed well in restoring the stiffness and strength relative to the original CFST. Adding additional weld bead strips along the height of the pedestal resulted in a clear increase in strength and stiffness, as well as a reduction in pedestal rotation contribution. Figures 4-15b and 4-15c therefore show a greater stress distribution within the repair concrete and higher stress concentration within the infill concrete near the top of the pedestal, suggesting that a greater quantity of weld beads along pedestal height helps shift plastic deformation above the pedestal and reduces rigid-body rotation within the pedestal. There is only a marginal reduction in steel stress between Figures 4-16a to 4-16c, however, tube buckling is more pronounced at the plastic hinge of WB-x3, compared to WB-x2 most likely due to the increase rotation demand in for CFST column above the pedestal. Interestingly, increasing the repair tube thickness in WB-x3-1 appears to have little change in moment-drift and stiffness response compared to WB-x3. However, there is a significant improvement WB-x3-1 in reducing rigid-body rotation in the pedestal as indicated in Figure 4-14c. This suggests that increasing the

repair pedestal's moment of inertia is also an effective way to isolate rotation to the CFST above the pedestal.

#### **4. Comparison of the Repair Configurations**

Four repair configurations were selected to compare the performance of the welded ring, shear stud, and weld bead repair configurations: (1) ER-2x4t, (2) SS-x4, (3) WB-x3, and (4) WB-x3-1. These configurations were selected because they demonstrated the best performance in terms of achieving the stiffness and strength objectives. The moment-drift and rigid-body performances are compared in Figures 4-17a and 4-17b, respectively. As shown, the weld bead repairs (WB-x3 and WB-x3-1) were superior in terms of achieving target strength and stiffness objectives. This suggests that the overall rigidity of the FTM plays a significant role in repair strength performance and force transfer. ER-2x4t and SS-x4 are significantly longer and less rigid than the weld beads which ultimately which resulted in higher pedestal rotation contributions and larger inelastic deformations of the FTM. It should also be noted that all four repair methods selected for comparison in this section used FTMs that were distributed along the height of the pedestal (e.g. 2 welded rings, 4 shear studs, 3 weld beads) Thus it is recommended that this approach should be included in future designs.

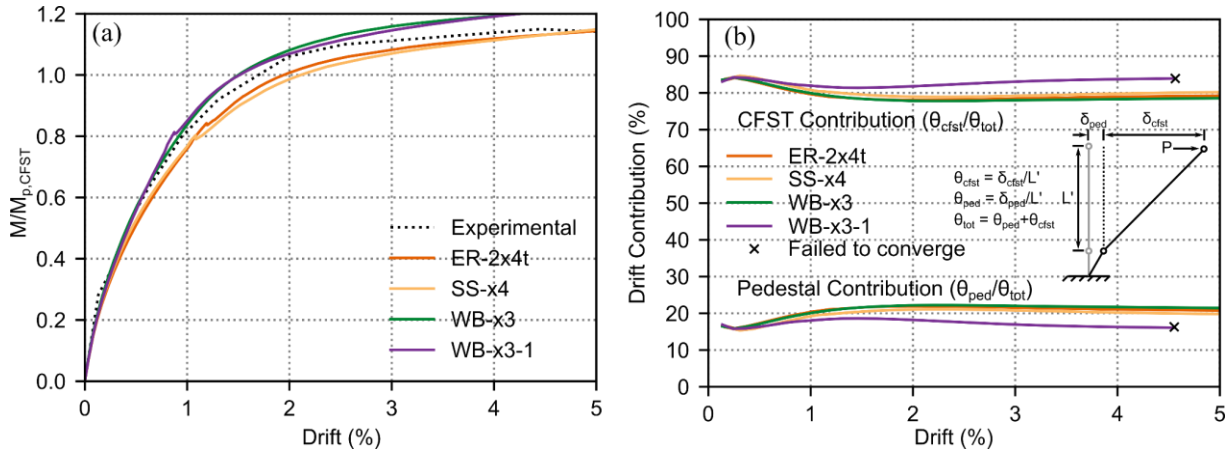


Figure 4-17: Comparison of the best performing repair methods, depicting the (a) moment-drift and (b) rigid-body rotation responses.

## 5. Hysteretic Performance of Weld Bead Repair

Based on performance of the weld bead repair (WB-x3) in terms of restoring stiffness and strength, a further non-linear, numerical analysis was performed to evaluate the reversed cyclic hysteretic response. The repair model was analyzed using a reduced ATC loading protocol (Krawinkler, 1992). The moment-drift response is presented in Figure 4-18.

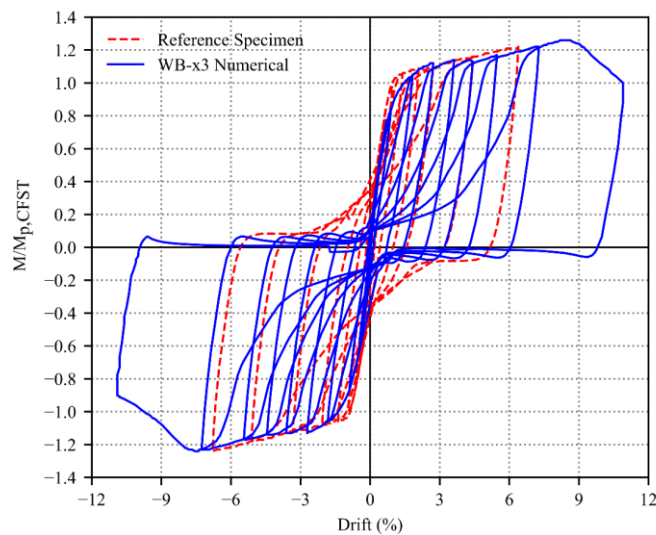


Figure 4-18: Hysteretic performance of WB-x3 compared to the numerical results of the reference specimen.

The WB-x3 repair configuration was successful in achieving the strength and stiffness capacity of the original, CFST column, very closely matching the same peak moment capacities in early stage, drift demands. Strength degradation was not observed until roughly 6.5% drift, where a maximum  $M/M_p$  ratio of 1.26 was achieved. This equates to 1.89  $M/M_p$  that is induced at the base of the pedestal. The theoretical plastic, moment capacity of the pedestal was calculated as 2.56  $M/M_p$  using the strain compatibility method (SCM), and 2.45  $M/M_p$  using the plastic stress distribution method (PSDM). However, yielding was observed within the pedestal reinforcing at the pedestal-foundation interface, where a maximum PEEQ strain of 0.007 in/in was recorded. This suggests that the two proposed design methods for calculating the required strength of the pedestal, underestimate the required strength to prevent yielding of the reinforcement, however the reasoning for this needs to be researched further.

## **6. Pedestal Reinforcement**

As detailed in Chapter 4.2, pedestal reinforcement was designed to elastically resist the pedestal-foundation/cap-beam moment demand of the repaired CFST. Results from the parametric studies conducted here indicated that the extreme fiber, repair reinforcement in the welded ring and shear stud configurations remained elastic. Repair methods that utilized weld beads, however, exhibited a different trend. Repair reinforcement within WB-x2 remained elastic throughout loading, however repairs WB-x3 and WB-x3-1 exhibited yielding of repair reinforcement at approximate drifts of 1.75% and 1.50%, respectively. To characterize this behavior, Figure 4-19 shows the PEEQ (in/in) versus drift relationship for the most extreme tensile reinforcing in the pedestal for weld bead configurations WB-x3 and WB-x3-1. Note that WB-x3-1 is only presented until roughly 3.30% drift due to the model terminating prematurely. The greater strain demand on

the pedestal reinforcement in the weld bead repairs is potentially a result of the relatively large stiffness and strength of the repair. In the welded ring and SS repair methods, larger inelastic deformations developed in the welded ring and shear studs which resulted in a reduction in the rotation demand on the pedestal. As a result, this reduced the strain demand of the pedestal reinforcement such that yielding was not observed. However, as the rigidity of the FTM improves (as was the case for the weld bead repairs), the embedded CFST is more constrained by the repair pedestal, and imparts a larger moment into the pedestal that is resisted by the pedestal reinforcing.

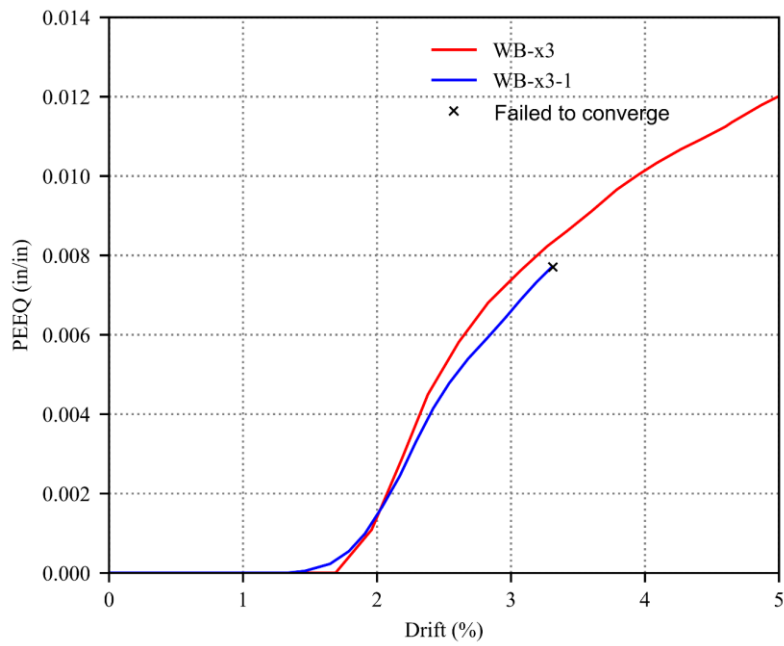


**Figure 4-19: PEEQ vs %Drift of WB-x3 and WB-x3-1 repair methods of extreme fiber reinforcing in pedestal.**

## **5.0 Performance-Based Repair Strategy**

This chapter covers the design and a limited numerical study of a performance-based repair strategy that incorporates bolted and replaceable external energy dissipators for resistance. First, a detailed description of the repair configuration is provided, including the components of the repair, the performance-based objectives, and design methodology. Then a description of the energy dissipator is provided, as well as a proposed design methodology for an individual energy dissipator. Next, an experimental investigation into the performance of the proposed energy dissipator, including the experimental methodology and results of cyclic-compression loading protocol are discussed. Then finally, the numerical methodology to evaluate the global response of the performance-based repair and results from the study are presented.

### **5.1 Performance-Based Repair Strategy Overview**

The performance-based repair strategy uses replaceable external, energy dissipators that are field-bolted to a CFST pedestal which encases the damage region of the original, CFST column as illustrated in Figure 5-1. The use of three rows of weld beads was selected to serve as the force transfer mechanism between the original CFST column and repair pedestal, given the success of this configuration as demonstrated in Chapter 4.0. The repair concrete fill in the pedestal provides concrete confinement of the exposed, damaged concrete of the CFST column. In addition, the repair pedestal includes a welded, annular steel plate located at the pedestal-foundation/cap-beam interface, thus isolating the damaged, CFST from the foundation, and allowing for column-rocking

along the damaged region. The repair configuration eliminates the need for reinforcement extending from the foundation/cap-beam into the repair pedestal, as load is transferred from the pedestal to the foundation via the external, energy dissipators which are epoxied into foundation. To facilitate replacement, the dissipators are bolted to a steel flange that is welded at the top of the repair. Due to the high concentrated forces at the connection points, the flange is stiffened using steel plates that are welded between the underside of the flange and exterior of the steel tube. One main impetus for using energy dissipators as the sole source for moment resistance is that it allows the designer to tune the structure to a desired strength and stiffness objective by means of adjusting the quantity or size of the dissipators. A further description of the type of energy dissipator that is utilized in this investigation called the BRBar, is provided in Section 5.3.

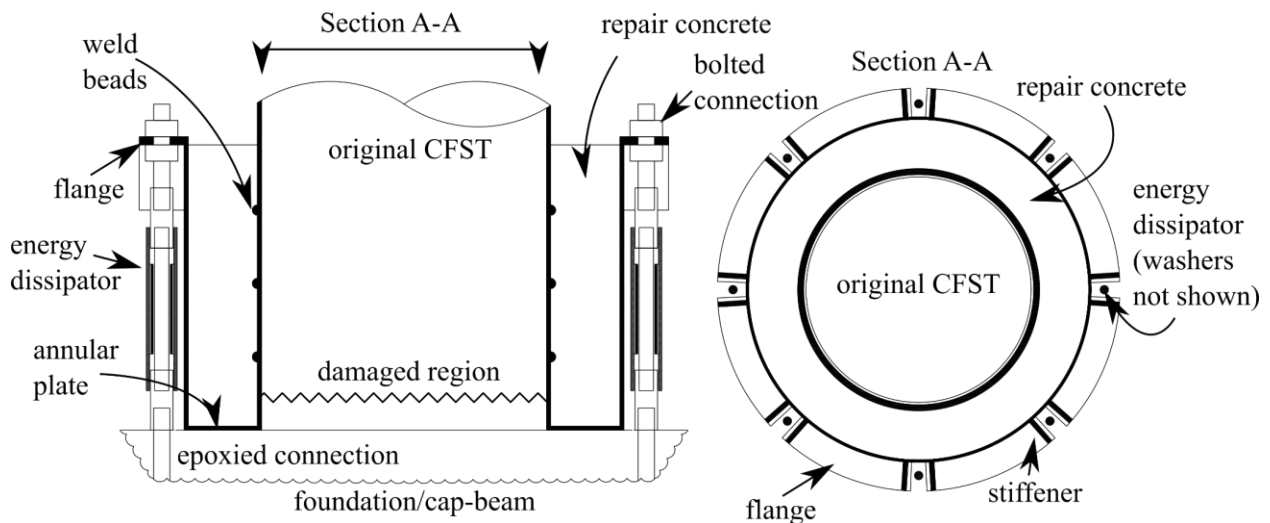


**Figure 5-1: Performance-based repair using external energy dissipators and column-rocking.**

The idealized column-rocking behavior is shown in Figure 5-2. Due to column-rocking at the base of the pedestal, the effective CFST length ( $L'$ ) and the pedestal ( $H$ ), will ideally rotate as a rigid system. As a result, plastic hinging and subsequent outward, tube buckling would not be

observed above the pedestal, and inelastic behavior is controlled to only occur in the external, energy dissipators, allowing for rapid-replacement of the dissipators post-earthquake to return the structure to service. This differs from the plastic hinge relocation repair, where the pedestal and effective CFST, operate as two isolated systems, with ideally no pedestal rotation.

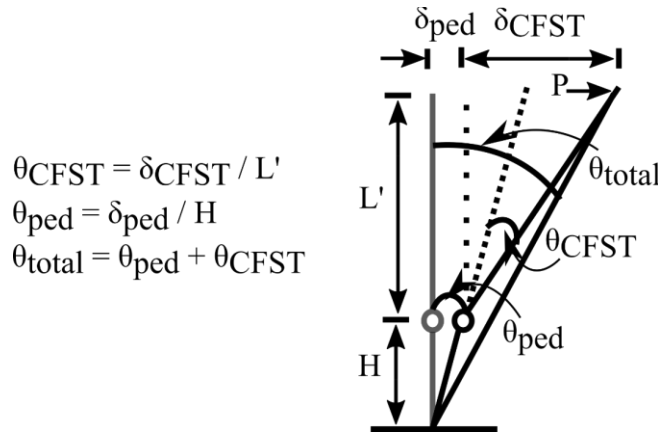


Figure 5-2: Idealized rigid-body rotation of the performance-based repair.

## 5.2 Design of the Performance-Based Repair

The following section outlines a design strategy for the performance-based repair method to design for strength of the global repair strategy (i.e. the entire BRBar-repair pedestal system). Recommendations are provided for estimating the repair's flexural strength, and for sizing the repair pedestal. A further discussion on designing the BRBar on the subcomponent level, is provided in Section 5.3.1.

The design strategy of the performance-based repair method requires unique design considerations due to the presence of column-rocking at the base of the pedestal and the

replaceable energy dissipators outside the footprint of the pedestal. Since rotation of the CFST occurs along the damaged section, the only moment being transferred into the foundation/cap-beam is from the compression of the pedestal coupled with the tension from the dissipators. Thus, the moment strength of the connection can be explicitly selected by the designer. To achieve flexural capacity, the designer can manipulate either the size or the quantity of BRBars. However, there are some tradeoffs between these two options. For example, a larger quantity of energy dissipators would likely be more labor intensive and would require a larger footprint, that may not be available for construction, as well as additional fabrication work to manufacture the flange of the repair steel tube to accommodate for the dissipators. However, with smaller BRBars, the required anchorage depth into the adjoining, concrete element would be shorter and may reduce the likelihood of interfering with internal reinforcement. The manufacture and labor requirement would likely decrease with larger BRBars; however, their larger embedded section would increase the required anchorage depth, thus likely increasing the chance of interfering with existing foundation/cap-beam reinforcement.

In addition, since pedestal reinforcement is not required, the pedestal height ( $H_{r,tube}$ ) is no longer a function of the required height to develop the repair reinforcement. Instead, its minimum required height is primarily a function of the required height to fit the BRBar assembly.

To design the strength of the performance-based repair, a similar moment-curvature analysis presented in Section 4.2 (e.g. strain compatibility and plastic stress distribution methods) can be implemented, under the assumption that the performance-based repair cross-section, behaves as a reinforced concrete section, with reinforcement (the BRBar energy dissipators), located outside the footprint of the pedestal. The idealized stress-strain, equilibrium diagrams are

presented in Figure 5-3 and 5-4 for the strain compatibility method, and plastic stress distribution method, respectively.

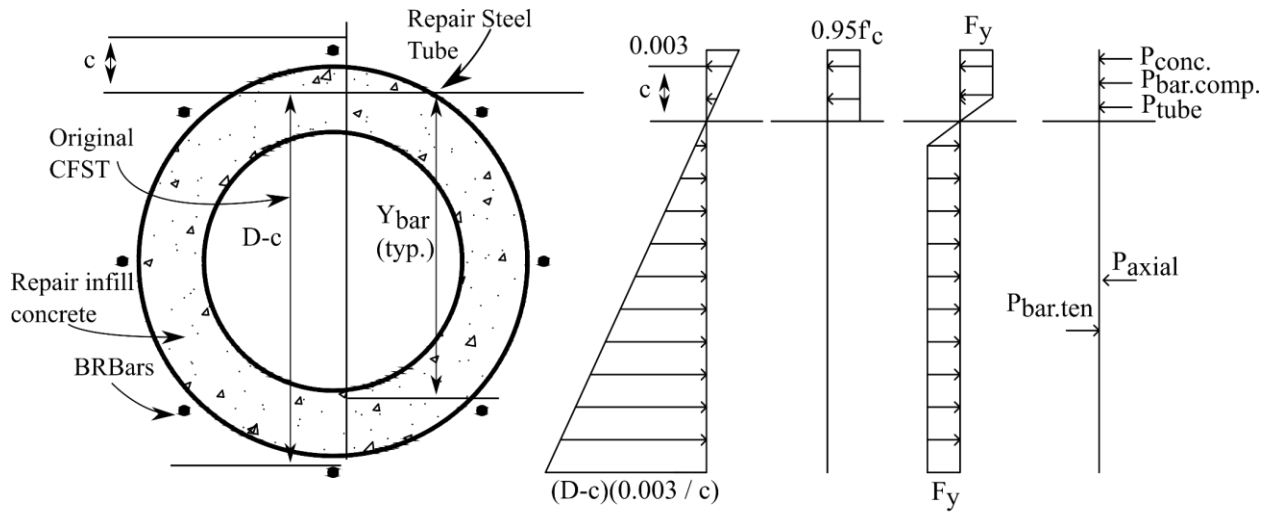


**Figure 5-3: Strain compatibility method idealized equilibrium diagram.**

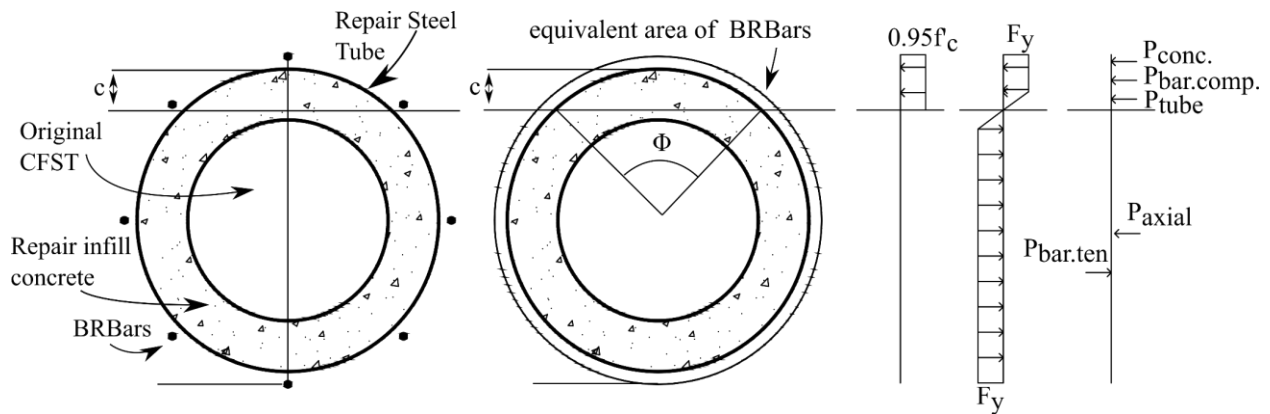


**Figure 5-4: Idealized plastic stress distribution method equilibrium diagram.**

There are several key differences between the plastic hinge relocation repair and performance-based repair design methods that need to be considered. First, because the BRBars operate outside of the pedestal, the area of concrete in compression does not need to be reduced by the area of the bars within that area. Next, the confining tube on the pedestal is assumed to only

provide compressive resistance; its tension resistance is neglected due to the rocking mechanism. To facilitate design calculations, the BRBars can be transformed into an equivalent concentric, thin-walled tube, similar to the procedure described in Chapter 4.2, and area calculations can be calculated using the typical angle,  $\Phi$ , shown in Figure 5-4. This approach is only adopted for the plastic stress distribution method. It should also be noted that the strain compatibility method was selected based on its ability to estimate the capacity of RC structures subjected to axial and bending loadings, however, since the BRBars operate outside of the concrete, it is likely that this method will not perform well.

### **5.3 Buckling Restrained Reinforcing Bar (BRBar)**

The performance-based repair strategy utilizes a buckling restrained, reinforcing bar fuse (BRBar) as the replaceable external energy dissipator. The BRBar is designed using concepts commonly implemented in large scale, buckling restrained braces used in buildings in seismic regions (Bruneau et al., 2011). Figure 5-5 shows a cross-section of the BRBar, depicting a larger bars couple with LENTON transition couplers, to a smaller bar that is restrained from buckling; the smaller bar acts as the structural fuse, while the larger bars are designed to remain elastic (White, 2014). Readily available, steel reinforcing bars are used both as the restrained structural fuse and the larger non-yielding section that extends into the concrete element. The other end of the BRBar utilizes a larger section of non-yielding, all-thread bar which provides a threaded bolted connection to the steel flange of the repair steel tube.

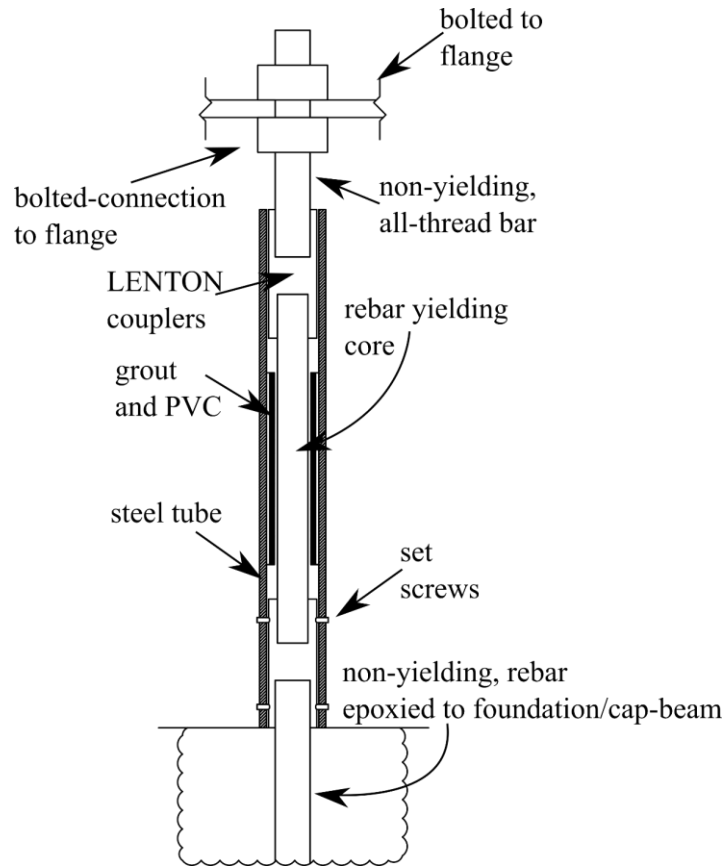


**Figure 5-5: Depiciton of the BRBar energy dissipator.**

A buckling restraining mechanism (BRM) surrounds the yielding fuse to prevent buckling before compressive, yielding can develop. The BRM consists of a hollow, thin-walled steel tube with an internal, PVC tube that is epoxied to its interior face to serve as the debonding agent to prevent longitudinal force transfer between the yielding fuse and BRM. To connect the BRM to the bar-coupler system, a series of set screws are threaded through the bottom of steel tube of the BRM into the adjacent coupler. This has three purposes: (1) to center all the components of the BRBar, (2) to allow for the yielding bar to freely deform within the BRM, without transferring forces between the two elements, and (3) to allow the internal, yielding fuse to easily be replaced post-earthquake since the BRM and fuse are connected using removable screws, thus eliminating the need to replace the entire BRBar system,

### 5.3.1 Subcomponent Design of the BRBar

The ductility design of each individual, BRBar is based on the expected strain history of a BRBar placed at the location of extreme tensile and compressive resistance. The expected maximum strain of the yielding bar can be calculated as a function of the target drift ( $\theta$ ) using a rigid-body analysis as depicted in Figure 5-6. In this analysis, it is assumed the pedestal rotates about the interior edge of the steel tube of the original CFST column, referenced as Point R, in Figure 5-6. It should be noted that this rotation point is along the damaged region, not along the foundation/cap-beam level. The distance  $X_{ten.}$  is the distance from Point R to the centroid of the extreme tension resisting, BRBar, while  $X_{comp.}$  is the distance to the extreme compressive resisting, BRBar. At any given drift demand, an angle ( $\theta$ ) is used to designate the subsequent rotation demand of the BRBar, or the angle between the point of rotation (Point R) and the point of deformation of the BRBar. Using trigonometry, the angle ( $\theta$ ) is equivalent to the inverse tangent of the drift of the column ( $\theta$ ). At a given column drift ( $\theta$ ), (5-1) provides a generalized, deformation equation, derived to calculate the theoretical, deformation demand ( $\Delta_{BRBar}$ ) of either the extreme tension or compression BRBar for cases of X equal to  $X_{ten.}$  or  $X_{comp.}$ , respectively. To calculate the maximum deformation, column drift ( $\theta$ ) is substituted with the maximum, target column drift ( $\theta_{max}$ ).

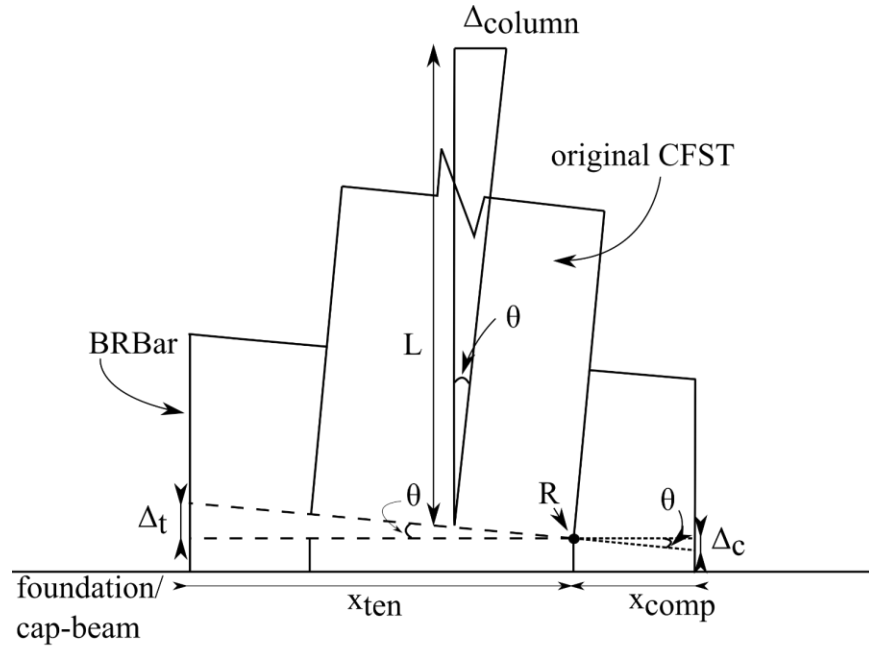


Figure 5-6: Idealized deformation demand of the BRBar at a given column-drift.

$$\Delta_{BRBar} = x \tan\left(\frac{\theta}{100}\right) \quad (5-1)$$

The required length of the yielding fuse ( $L_{fuse}$ ) is determined from the expected deformation demand ( $\Delta_{BRBar}$ ) due to tension, as calculated using (5-2) where ( $\epsilon_d$ ) represents the maximum desirable strain demand of the fuse. For this investigation, a value of 0.15-inch/inch was taken as the maximum strain demand of the rebar fuse.

$$L_{fuse} = \frac{\Delta_{d,BRBar}}{\epsilon_d} \quad (5-2)$$

The buckling restraining mechanism (BRM), which consists of a steel tube with an internal PVC pipe, grouted to the wall of the tube, is designed to resist global buckling of the BRBar system under compressive loadings. Bruneau et al. (2011) suggests that the BRMs of buckling restrained braces should be designed to resist a Euler buckling load ( $P_e$ ) of  $1.5P_y$ , where  $P_y$  is the yielding

load of the fuse. Given the uncertainty of the expected behavior of the BRBar, a value of  $2.0P_y$  was conservatively chosen for all BRBars evaluated here. It is also recommended to ignore the contribution of internal fill between the outside tube and fuse. Therefore, the moment of inertia of the steel tube ( $I_{tube}$ ) required to restrain buckling can be directly calculated using the Euler Buckling equation (5-3), assuming that the length of the tube ( $L_{tube}$ ) extends from the top to the bottom of the transition couplers. In addition to meeting this requirement, the restraining steel tube must also be sized to fit the transition couplers. In determining the required transition couplers, a diameter size of two-times the diameter of the yielding fuse should be used for the non-yielding elements within the BRBar assembly.

$$I_{tube} = \frac{P_e L_{tube}^2}{E\pi^2} = \frac{2.0P_y L_{tube}^2}{E\pi^2} \quad (5-3)$$

#### 5.4 Experimental Program for the BRBar Subcomponent

A limited experimental study was performed to evaluate the performance of the BRBar. The experimental procedure of the BRBar subcomponent consisted of testing two different sized BRBars (a #6 and #7, sized yielding core) under a cyclic, compression loading protocol. These will be referred to as BRBar#6 and BRBar#7, respectively herein. Two unbraced, reinforcing bars equal to the total length of the BRBars and sized at either a #6 and #7 diameter, were also tested to provide a baseline performance for comparison. These are herein referred to as Unbraced#6 and Unbraced#7, respectively. For BRBar specimens, the yielding cores were coupled to #8 rebar on one end, and a 1-inch diameter all-thread on the other. All other dimensions (e.g. core length, transition bar lengths, BRM length and size) were consistent between the two specimens, besides

the LENTON transition couplers required for the #6-to-#8 and #7-to-#8 transitions. An overview of the BRBar specimen is summarized in Figure 5-7.

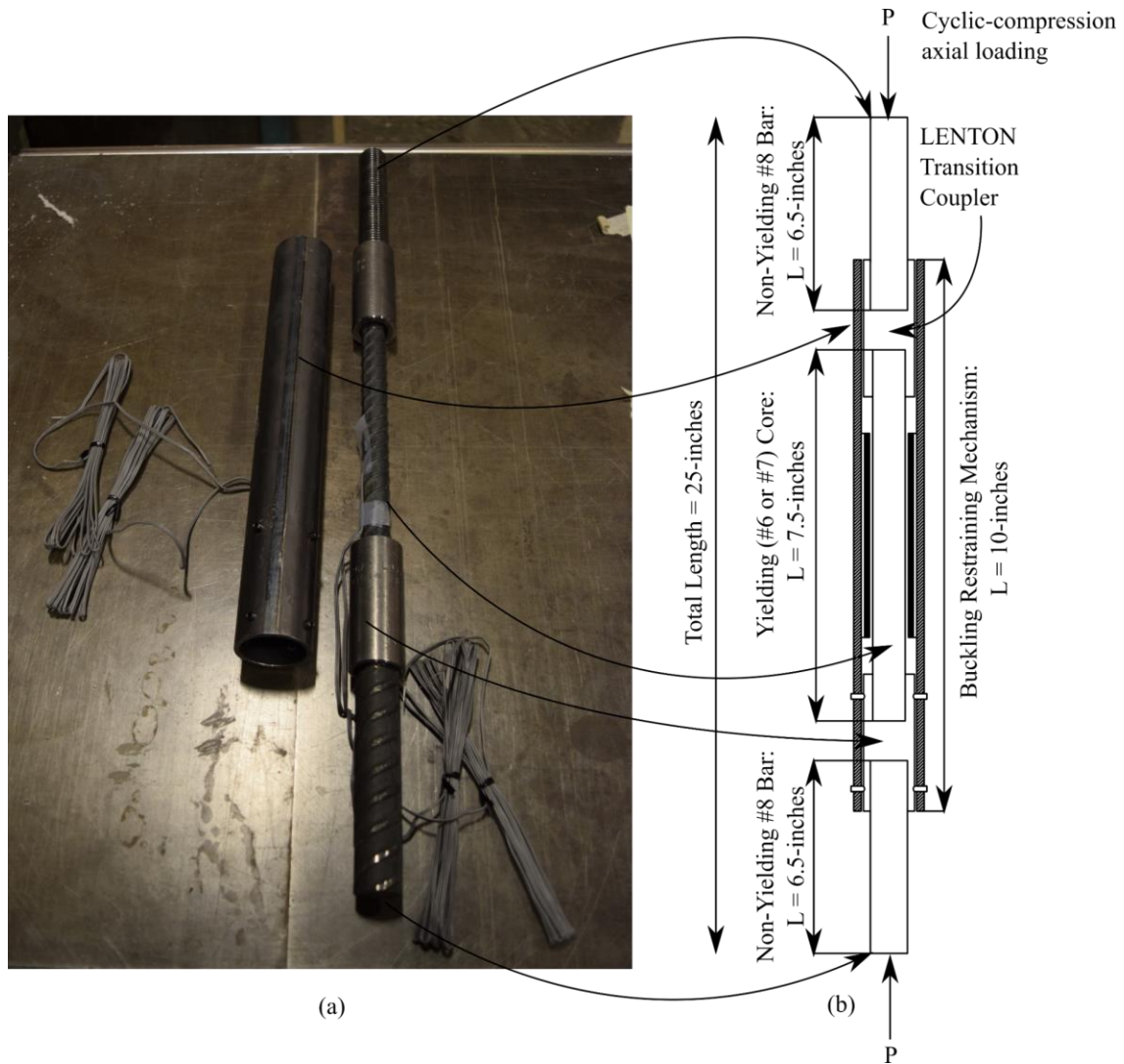


Figure 5-7: (a) Tested BRBar subcomponent with the (b) dimensions of each of its parts.

#### 5.4.1 Fabrication of Specimens and Experimental Setup

The BRBar specimens were primarily fabricated in the University of Pittsburgh Structural Lab. The core and non-yielding bars were cut to length, and the ends were threaded for the

transition couplers. The steel tube of the BRM was also cut to length, and two rows of four holes located in each quadrant were drilled and threaded for the set screws. Note that threading for the couplers had to be completed offsite using proprietary machinery at the LENTON coupler distributor.

After the reinforcing and all steel components were threaded and cut to size, the internal PVC pipe was grouted into place. Threaded plugs, shown in Figure 5-8a, were built to ensure that the PVC pipe remained concentric and at midspan of the steel tube during grouting (Figure 5-8b). The bottom plug was machined to the same diameter as the internal diameter of the steel tube to prevent any leakage of grout during casting, while the top plug was sized as the outside diameter of the PVC to prevent grout from entering inside the PVC. Both plugs were machined with a small lip at their ends that was equal to the internal diameter of the PVC to provide a tight fit which prevented leakage. A threaded rod, threaded into the bottom plug, was used to stabilize the BRM during grouting, and provided a way to remove the bottom plug after the grout had set. The latter process is depicted in Figure 5-8c. The bottom end of the steel tube was capped using a nut and washer screwed onto the exposed threaded rod, as shown in Figure 5-8c. Then, as the nut is tightened, the plug can be slowly pulled out of the PVC pipe and steel tube, leaving the grouted PVC in place. The top plug can then easily be punched out since only the lip is holding it into place.

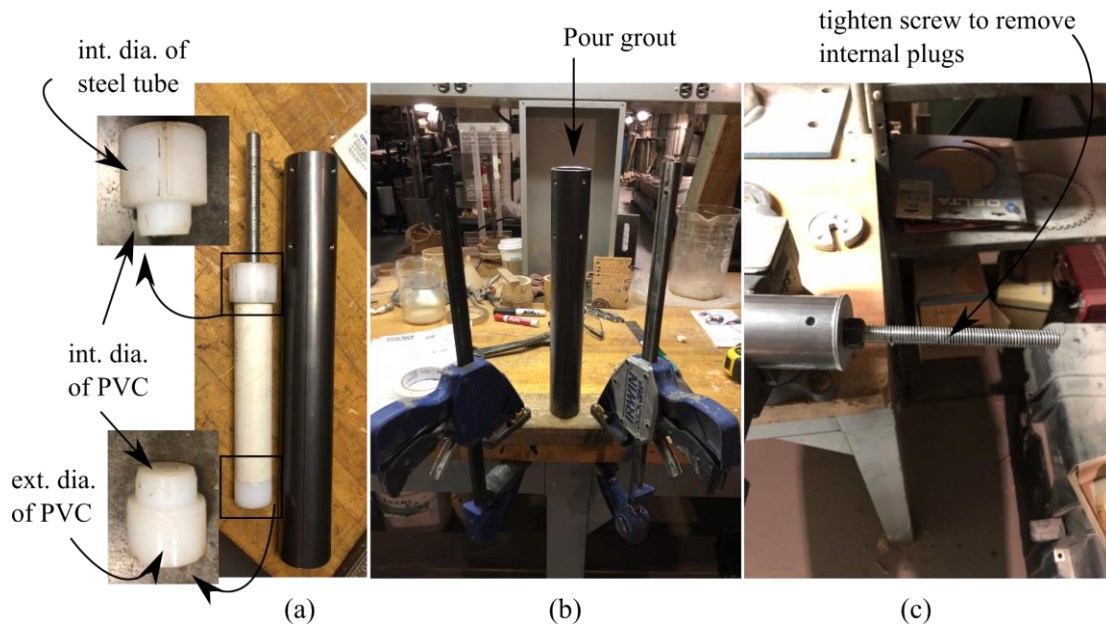


**Figure 5-8: (a) Internal plugs for (b) pouring the BRM's grout, and (c) removing them after curing.**

The BRBar specimens and unbraced baseline specimens were tested using a hydraulic, Universal Testing Machine (UTM) in the University of Pittsburgh Structures Laboratory. The testing apparatus, shown in Figure 5-9a, consisted of steel base plates with 1-inch diameter holes, bolted into the top and bottom of the UTM using set screws. The BRBar were fixed into the UTM during testing, by placing the specimens within the concentric holes of the base plates as depicted by the details of Figure 5-9a.

The compression loading protocol for the BRBars and unbraced specimens, shown in Figure 5-9b and 5-9c, respectively, were developed using (5-1) and were carried out under a displacement-controlled loading procedure, by converting the target strain to target displacement using the core length for the BRBar, or total specimen length for the unbraced bars. Due to the point of rocking being closer to the compression side than tension, as shown in Figure 5-6, an asymmetric displacement demand is subjected to the BRBar components, where the relationship between the tensile or compressive displacement of the BRBar at given drift demand is given by

the ratio of  $X_{ten.} / X_{comp.}$ . A small axial load of around 1-kip was placed first on the tested specimen before testing to remove any slack in the system.

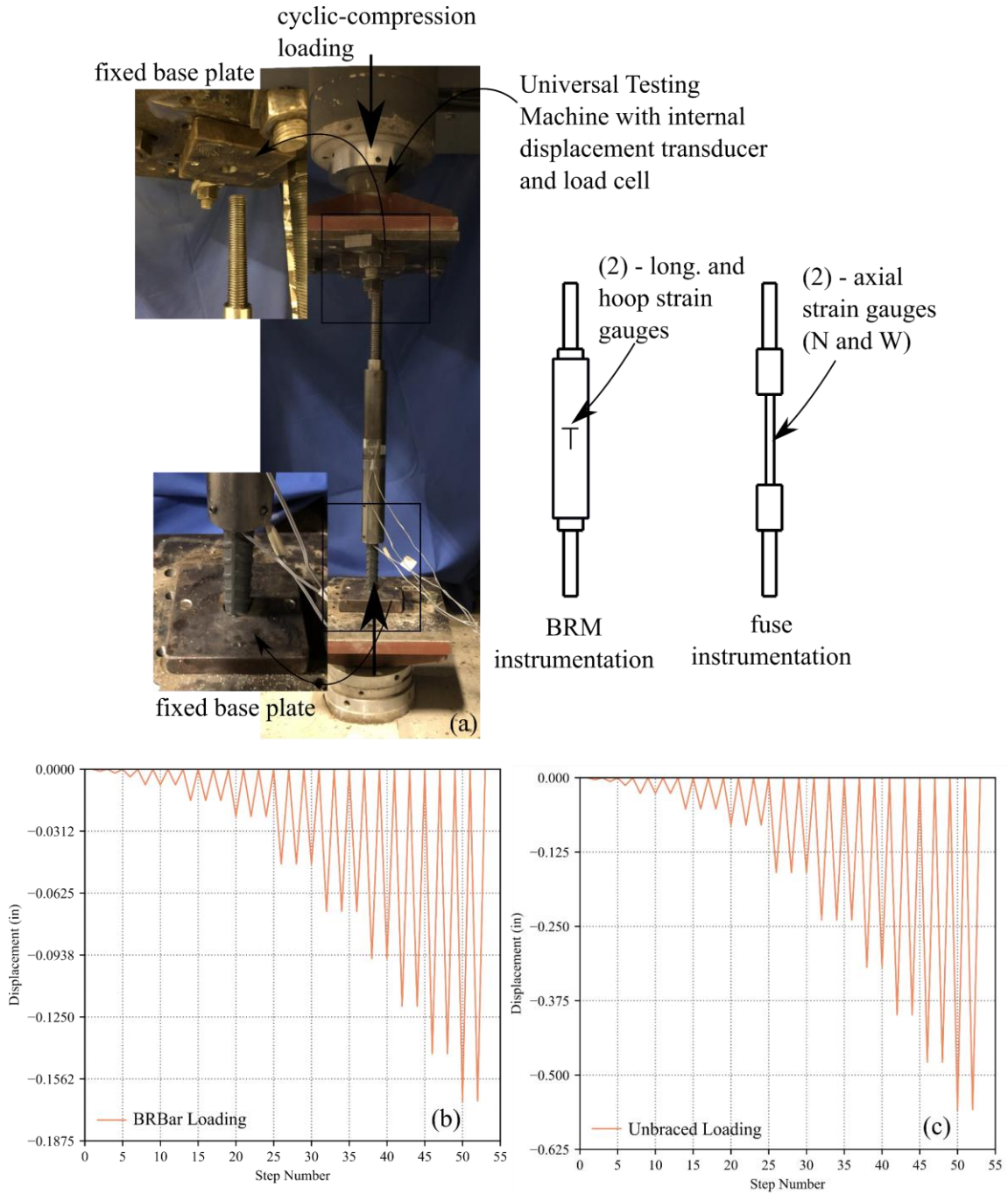


**Figure 5-9: (a) The experimental testing apparatus and displacement-controlled loading protocols for the (b) BRBars and (c) unbraced specimens.**

Displacement and force were measured directly from the UTM using its internal position transducer and load cell. Strain measurements were captured using YFLA-5-3LJC-F strain gauges that were placed on the steel tube of the BRM and yielding core. For the steel tube, one strain gauge was oriented longitudinally to capture axial strain while the other was placed transversely to capture hoop strain. This was done to assess demands on the steel tube restraining mechanism. One strain gauge was placed longitudinally along the northern (N) face and another strain gauge was placed longitudinally along the western (W) face of the yielding core. All measurements were gathered using a National Instruments, Compact Data Acquisition (DAQ) system.

## **5.4.2 Results and Discussion**

### **BRBar#6 Specimen**

Figures 5-10a and 5-10b, show the loading response of Unbraced#6 and BRBar#6. During testing of BRBar#6, a local instability occurred in the rebar-coupler system due to the presence of the 1/16-inch gap between the top coupler and steel restraining tube. This resulted in the BRM insufficiently restraining the lateral movement of the BRBar, and as loading progressed, local buckling occurred directly below the top coupler in the yielding fuse. The inherent eccentricity of the testing apparatus may also have further exacerbated this response as well.

However, the BRM was able to restrain further lateral movement once contact was initiated, thus significantly improving the compressive capacity of the BRBar where a maximum force of  $1.04F_y$  was observed during testing. Successful yielding of the BRBar fuse was further confirmed by observing the measured force vs measured strain response of the northern (N) and western (W) strain gauges, as depicted in Figures 5-11a and 5-11b, respectively. In both figures, the theoretical yield ( $\epsilon_y = 0.002$  in/in) was surpassed for the yielding core, with slight residual,

inelastic strain being observed in both strain gauges. Limited strain was observed within the steel restraining tube, as shown in Figures 5-12a and 5-12b which plot the longitudinal and hoop strain versus force responses, respectively. A maximum longitudinal and hoop strain of 0.000041 in/in and 0.000016 in/in were recorded, respectively, suggesting very marginal stress stresses developed in the steel tube. However, strain gauges were placed at mid-span and a larger strain response would be expected to have occurred near the top of the BRM, where the coupler was bearing against the steel tube, though no permanent deformations of the steel tube were visually identifiable after testing.

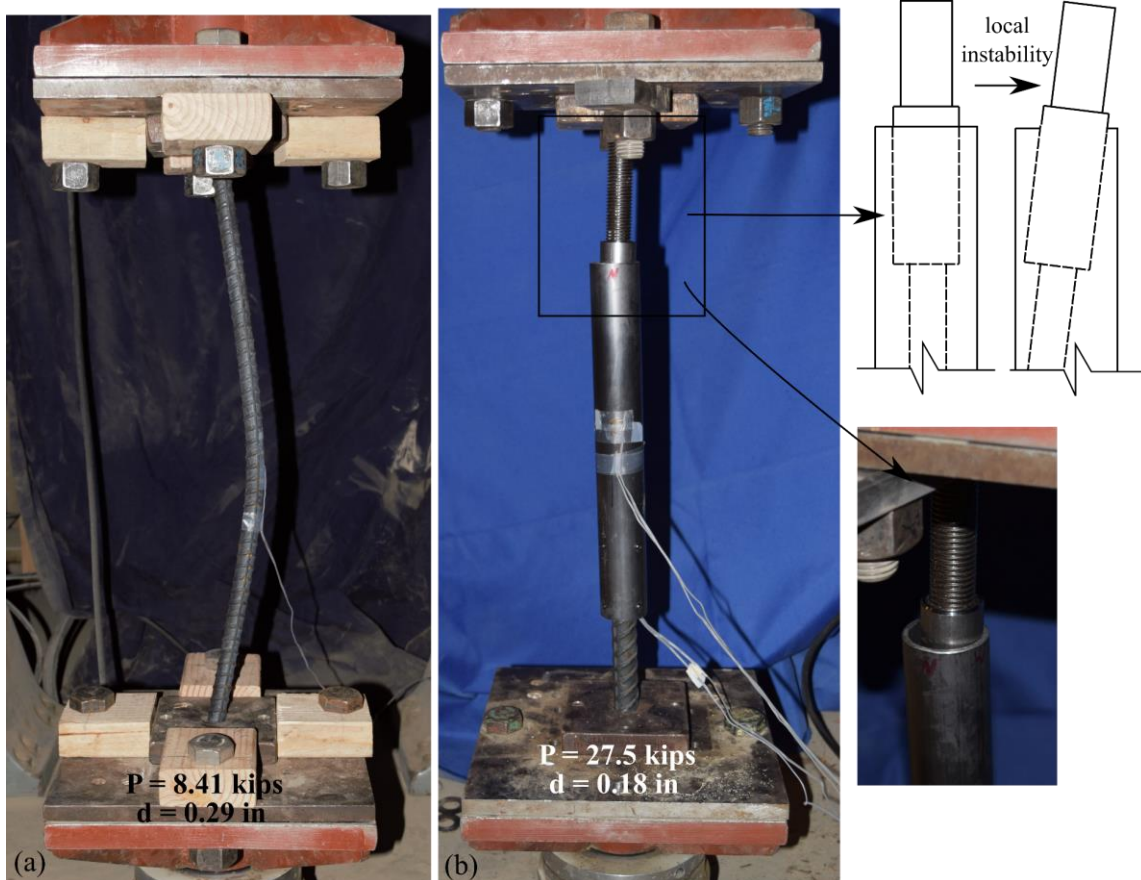
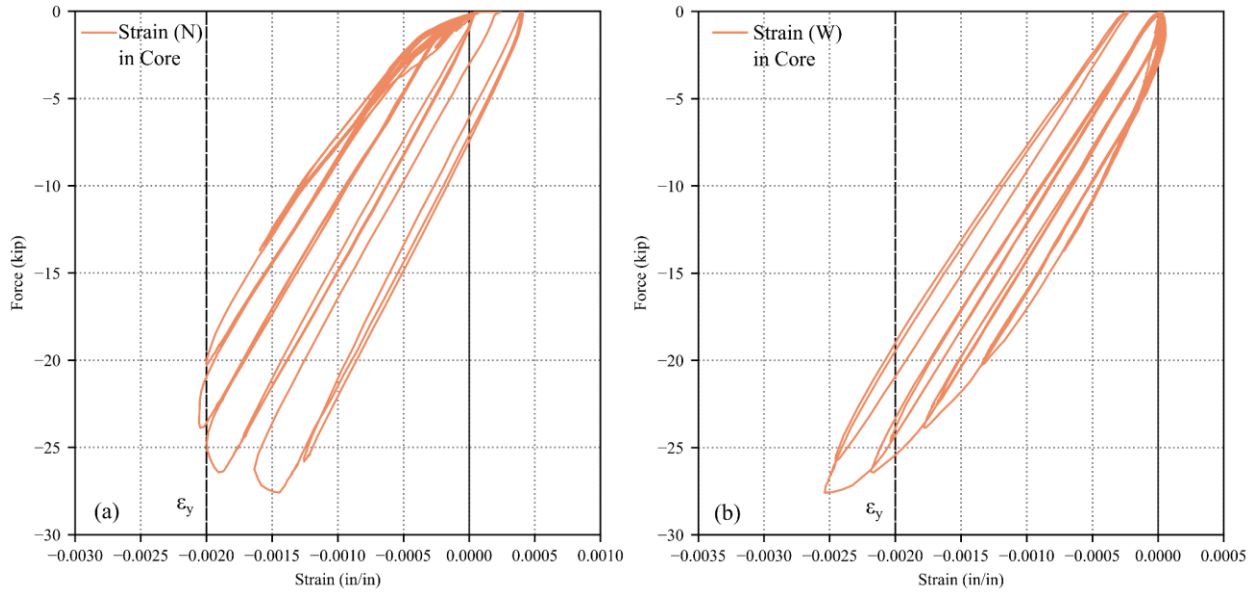
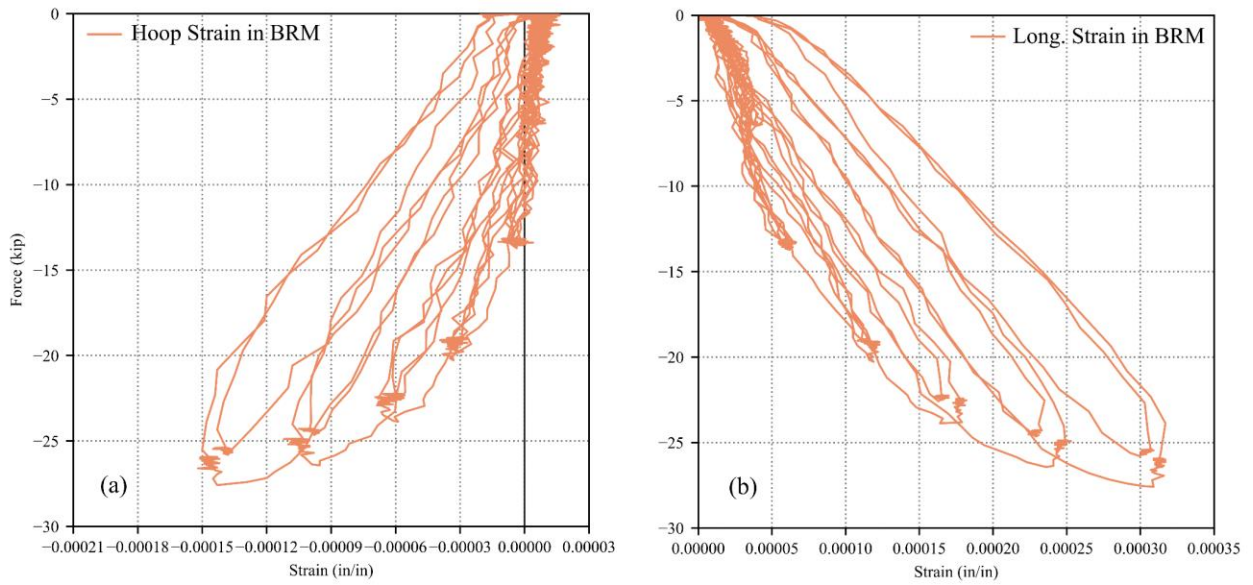


Figure 5-10: (a) Unbraced#6 deformation response compared to (b) BRBar#6.

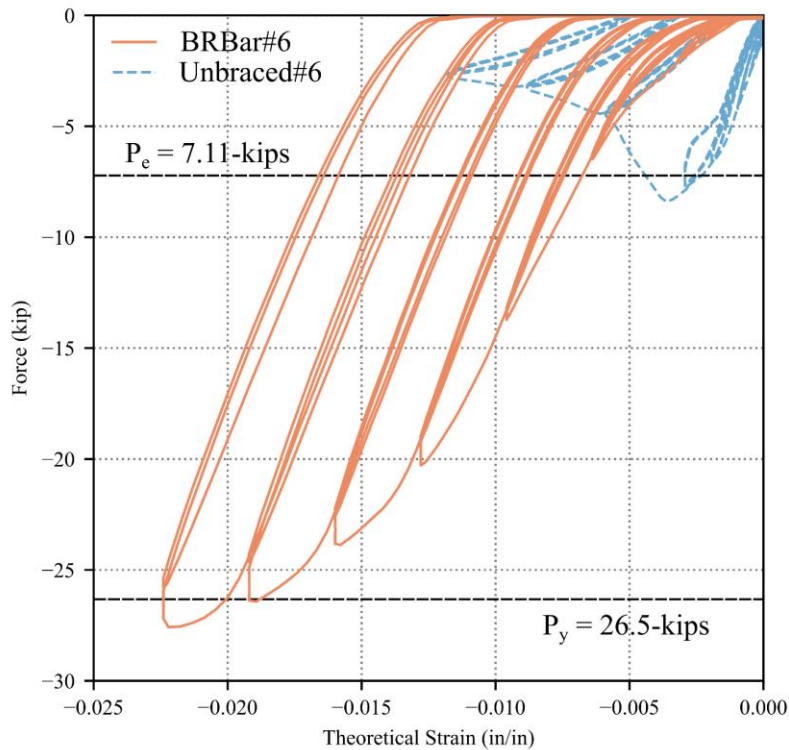


**Figure 5-11: Force vs strain responses recorded by the (a) Northern and (b) Western strain gauges on the yielding core.**



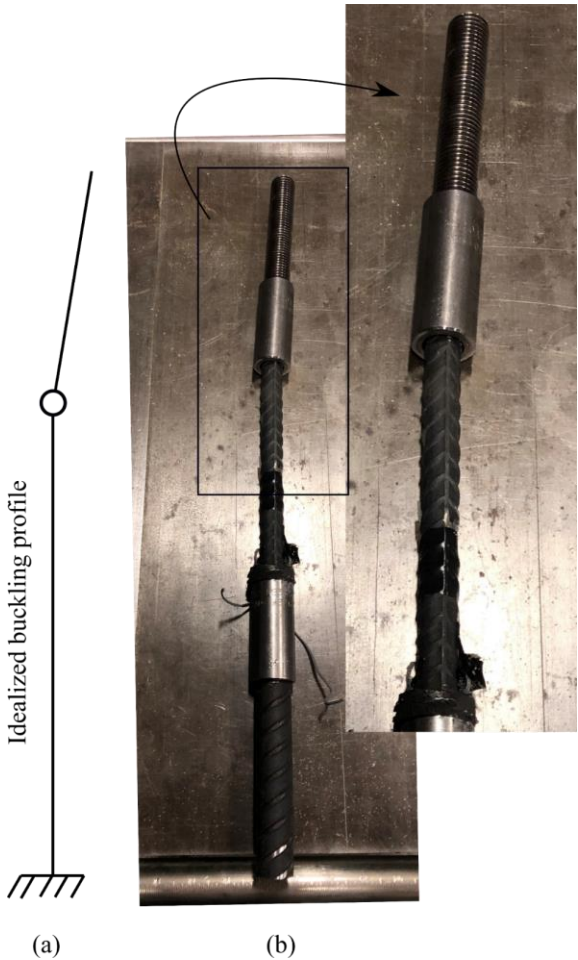
**Figure 5-12: Force vs strain responses recorded by the (a) hoop strain and (b) longitudinal strain gauges on the steel tube of the BRM.**

Figure 5-13 shows the force versus theoretical strain (i.e. strain calculated in (5-1)) plots of the BRBar#6 and Unbraced#6 specimens. The theoretical yielding force ( $P_y$ ) of the yielding core and Euler Buckling load ( $P_e$ ) of Unbraced#6 are also plotted for reference. It should be noted that the BRBar#6 was not loaded to an initial, axial load of 1-kip before testing which resulted in the low initial stiffness shown in Figure 5-13, compared relative to Unbraced#6 which was preloaded to 1-kip to remove all slack within the system. Testing showed that Unbraced#6 reached a maximum axial load of  $0.32F_y$ , before the initiation of buckling and significant strength degradation were observed. In addition, the side-by-side comparison of the deformed shapes in the BRBar#6 and Unbraced#6, shown in Figures 5-10a and 5-10b, demonstrates that the buckling restraint is effective in decreasing overall out of plane displacement, even when the coupler isn't fully supported by the buckling restraint tube.



**Figure 5-13: Theoretical strain (in/in) vs force (kip) response of BRBar#6 and Unbraced#6.**

Figures 5-14a and 5-14b show the final deformed shape of the BRBar after testing concluded. The lateral displacement of the top non-yielding bar and coupler is clearly shown to have occurred within the BRM. When removing the BRM, it can be seen that buckling occurred slightly below the coupler, in the reduced section of the yielding core, while bars below this point remained mostly unaffected. This test demonstrated the importance of fully restraining the rebar-coupler system and removing any gaps between the steel tube and couplers, which otherwise reduce the compressive capacity of the BRBar.



**Figure 5-14: The (a) idealized buckling profile of BRBar#6 and (b) experimental buckling profile.**

## BRBar#7 Specimen

Due to the local instability that was observed in testing BRBar #6 which resulted from the 1/16-inch gap between the coupler and steel tube, steel bushing was fabricated for BRBar#7 to remove the gap, and provide continuous restraint to the coupler during testing. The bushings are depicted in Figure 5-15a, and Figure 5-15b shows their location in BRBar#7. The bushings were machined such that they fit between the exact width of the opening, while still not restricting longitudinal displacement of the yielding core.

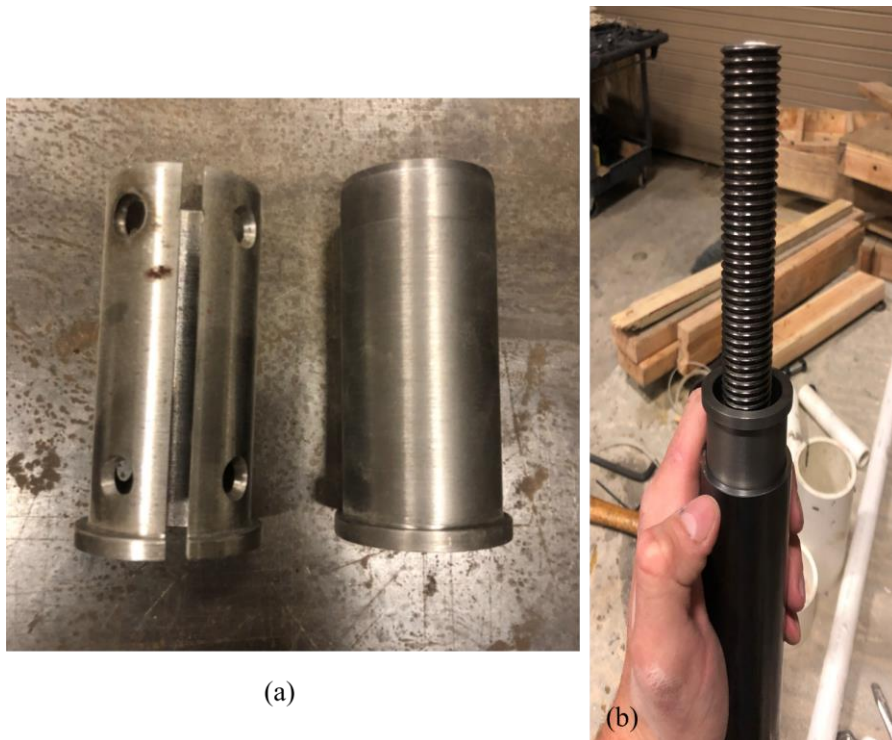


**Figure 5-15: (a) Bushing machined to be placed (b) between coupler and BRM to reduce lateral displacement.**

Lateral displacement of the coupler was able to be reduced by including bushings, and ultimately improved the compressive response of BRBar#7, where a maximum compressive force resistance of  $1.12F_y$  was recorded. Near the end of testing, noticeable buckling of the top, non-

yielding bar was observed due to its length and potential eccentric loadings within the UTM. This buckling response is shown in Figure 5-16. To overcome this, testing was prematurely stopped and the top, #8 threaded, non-yielding bar was replaced with the #8, non-yielding rebar used during the testing of BRBar#6. Testing resumed until stopping due to excessive buckling of both ends of non-yielding bars, as shown in Figure 5-17a and 5-17b, which depict the final deformed shape at peak loads for Unbraced#7 and BRBar#7, respectively. Yielding of the rebar core is further demonstrated by observing the force vs measured strain responses of the northern (N) and western (W) strain gauges of the yielding bar, shown in Figures 5-18a and 5-18b, respectively. Peak strain values of  $9.0\varepsilon_y$  and  $3.4\varepsilon_y$  were recorded in the northern and western strain gauges, respectively, before testing was terminated. Clear strain yielding and residual strain is captured in both strain gauges, further demonstrating the success of the BRBar to achieve yielding under compressive loading demands. Figures 5-19a and 5-19b, depict the axial and hoop strain response of the steel tube as a function of measured force. It can be seen that marginal strain development occurred in the steel tube, though again these values were recorded at the mid-depth of the tube and may otherwise be larger at the either end of the tube where extreme deformations occurred.

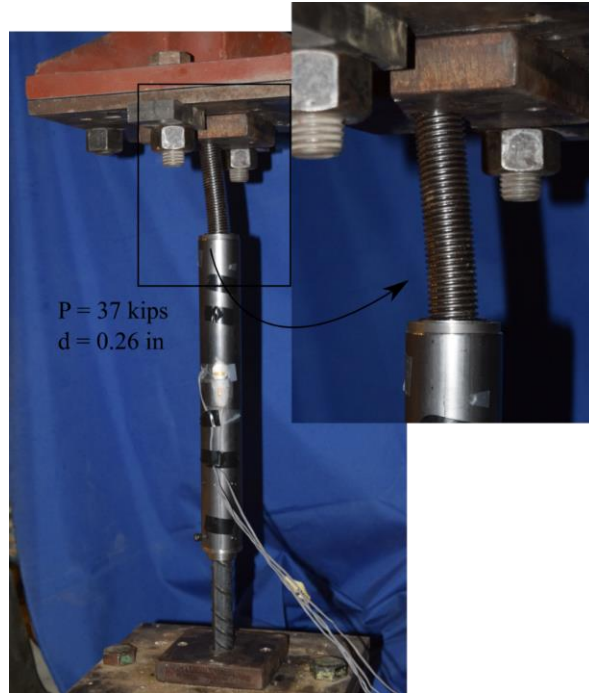


Figure 5-16: Depiction of the buckling of the top, non-yielding bar which was replaced during testing.

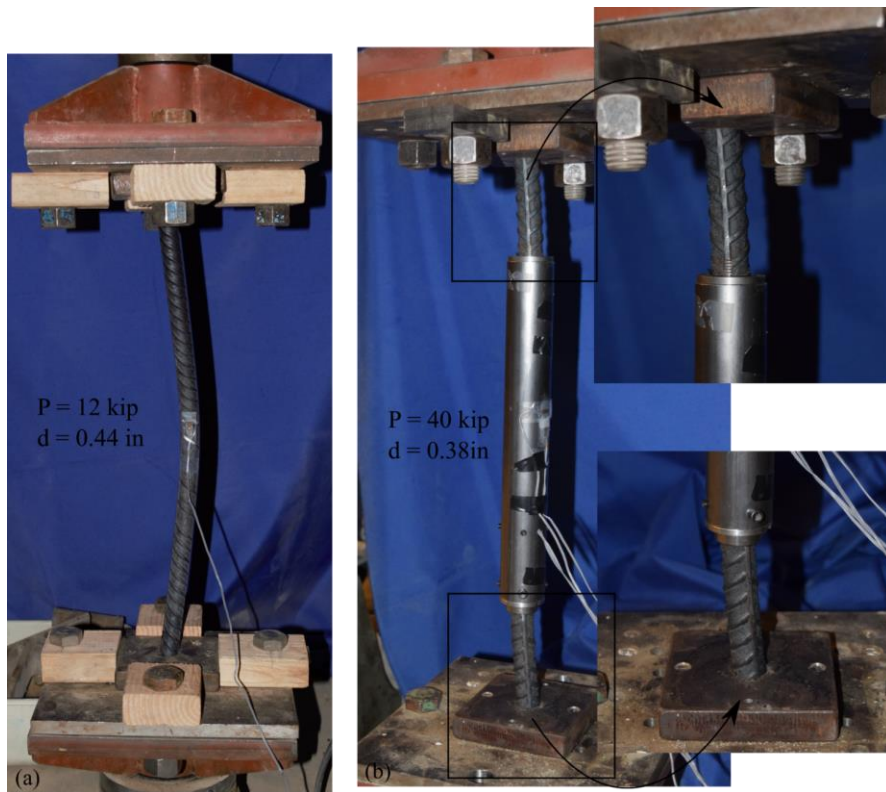
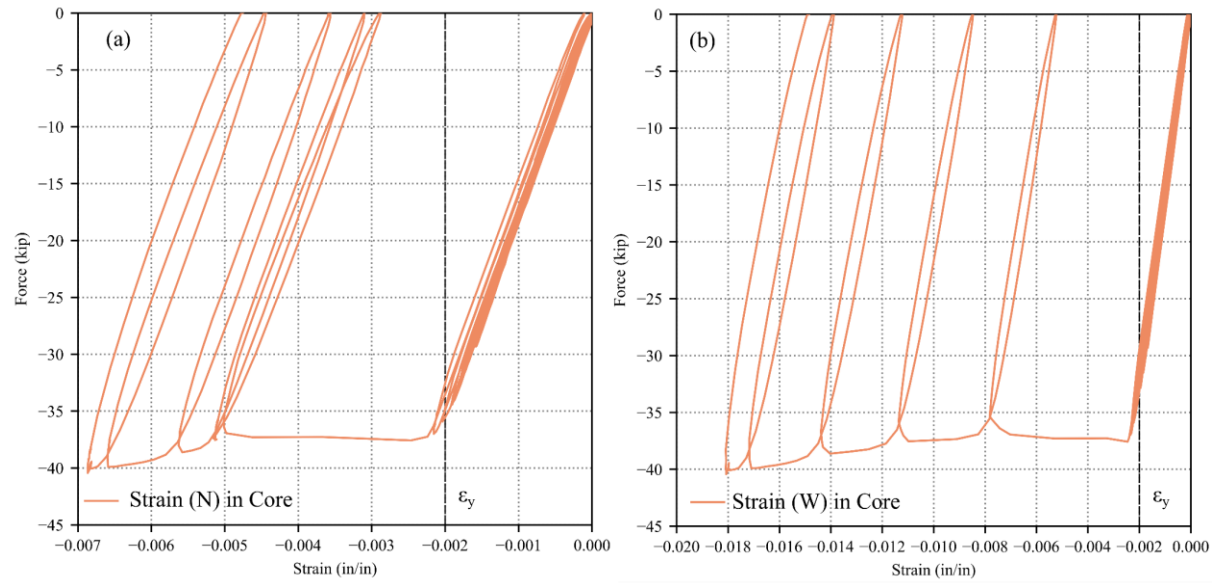
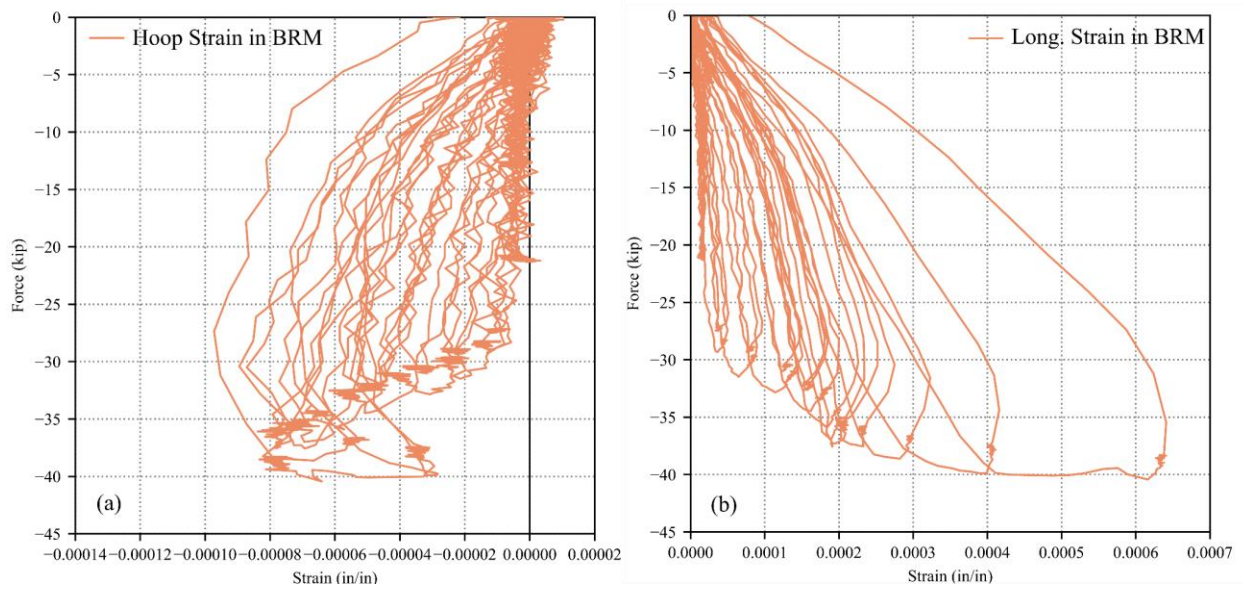


Figure 5-17: Final deformed shape of (a) Unbraced#7 and (b) BRBar#7.



**Figure 5-18: Force vs strain responses recorded by the (a) Northern and (b) Western strain gauges on the yielding core.**



**Figure 5-19: Force vs strain responses recorded by the (a) hoop and (b) longitudinal strain gauges on the steel tube of the BRM.**

Figure 5-20 shows the resulting force vs theoretical strain (i.e. strain calculated from (5-1)) response of BRBar#7 in comparison to Unbraced#7, with references to the theoretical yield of the fuse ( $P_y$ ) and Euler Buckling capacity of Unbraced#7 ( $P_e$ ). In this test, both BRBar#7 and Unbraced#7 were preloaded to approximately 1.0-kips, thus resulting in comparable, initial stiffness responses. In comparison to the BRBar#7, Unbraced#7 only achieved a maximum force response of  $0.33F_y$ , before significant strength reduction occurred due to buckling. This strength response, and the final deformed shape of the tested specimens shown in Figure 5-17a and 5-17b, demonstrate the ability of the bushings and BRMs to achieve yielding of the core and prevent extreme lateral deflections under compressive loadings. The final deformed shape of BRBar#7 is shown below in Figure 5-21a and 5-21b. As shown, a more dominant, S-Shaped buckling profile is observed in this specimen due to the buckling of the top and bottom, non-yielding bars above the coupler.

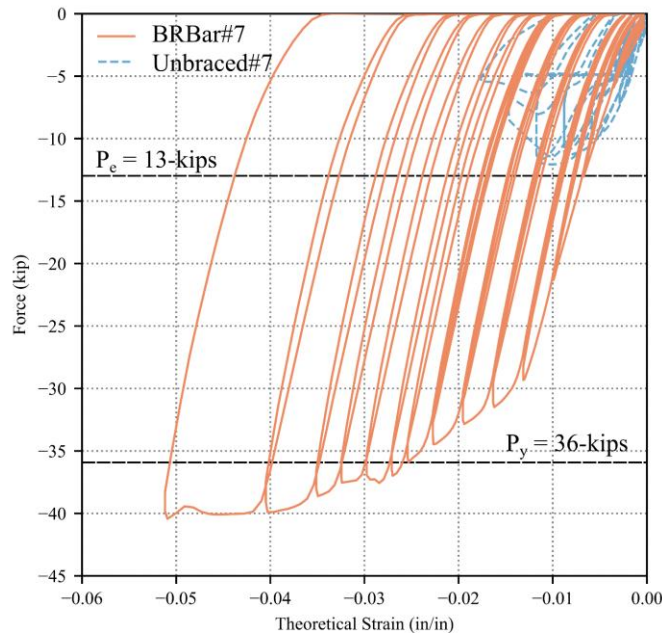


**Figure 5-20: Force vs theoretical strain of BRBar#7 and Unbraced#7**

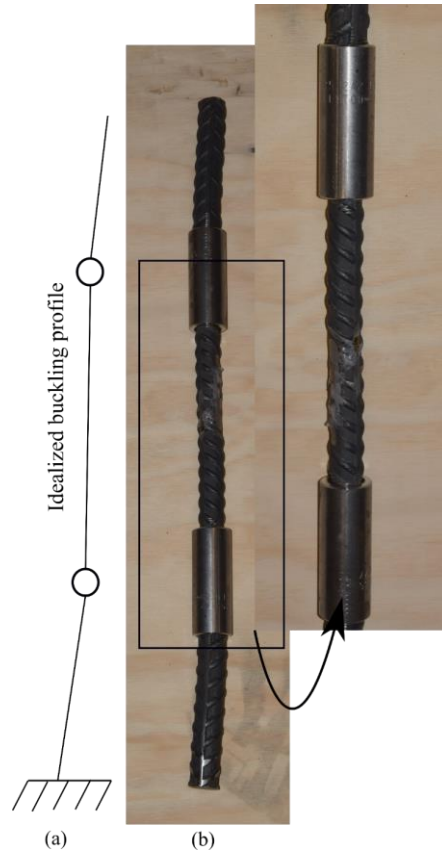


**Figure 5-21: The (a) idealized buckling profile of BRBar#7 and (b) experimental buckling profile.**

### **5.4.3 General Comments and Recommendation**

From this limited experimental study of the BRBars, several key recommendations can be made that should be followed in future experimental studies.

1. Minimize gaps between the steel tube of the BRM and couplers in order to prevent any local instabilities (Figure 5-10b). Testing here demonstrated that steel bushing (Figure 5-15a and 5-15b) can successfully eliminate instabilities and prevent lateral deflections of the coupler during testing.

2. Preload the BRBar to approximately 1-kip in order to reduce any inherent slack in the specimen, otherwise a low stiffness response will be observed during initial loadings (Figure 5-13).
3. Minimize the length of the non-yielding bars to prevent premature buckling during testing (Figure 5-17b). It is also recommended that a minimum diameter of two-times the yielding bar should be used for the non-yielding bars to further reduce the likelihood of buckling during testing, and in the field.

### **5.5 Numerical Modeling of Performance-Based Repair**

The analytical modeling procedure for developing the baseline damaged CFST model in ABAQUS uses the methodology presented in Chapter 3. To model the performance-based repair, components of the repair were added including: the repair pedestal (including the concrete, steel tube, baseplate and flange), the BRBar energy dissipator, and the connections between the BRBar and the flange and foundation.

The repair steel tube and concrete in the pedestal were modeled using the same inelastic material and element properties described in Chapter 4. However, in the performance-based repair model, there is no steel reinforcing included in the pedestal. The pedestal required the addition of the flange, flange stiffeners, and base plate. The base plate was assumed to be the same thickness as the steel tube, while the flange was modeled as twice its thickness and projecting 3-inches off the edge of the steel tube. The flange stiffeners were modeled to be 1-inch thick, with a depth of 4-inches and width spanning from the edge of the flange to outside face of the repair steel tube. All of these features were modeled as the same part within ABAQUS, rather than creating disparate

parts and using a tie constraint to develop the geometry. It was also assumed that each feature had the same inelastic material properties as the steel tube of the CFST column.

Sizing of these repair components were based on the design methods, and experimental evidence provided previously, and are summarized in Table 9. An overview of the model is shown in Figure 5-22a to 5-22b for reference, and a more detailed calculation procedure is provided in Appendix A2.

**Table 9: Design results of the performance-based repair for numerical investigation.**

Repair Strategy	$D_r$ (in)	$H_r$ (in)	$L_{core}$ (in)	$X_{ten.}$ (in)	$X_{comp.}$ (in)	$M_r$ (k-in)	$D_{fuse}$ (in)	Qty
PB - BRBars	36 (1.5D)	24 (1.0D)	15	31.125	7.625	11000	7/8	8

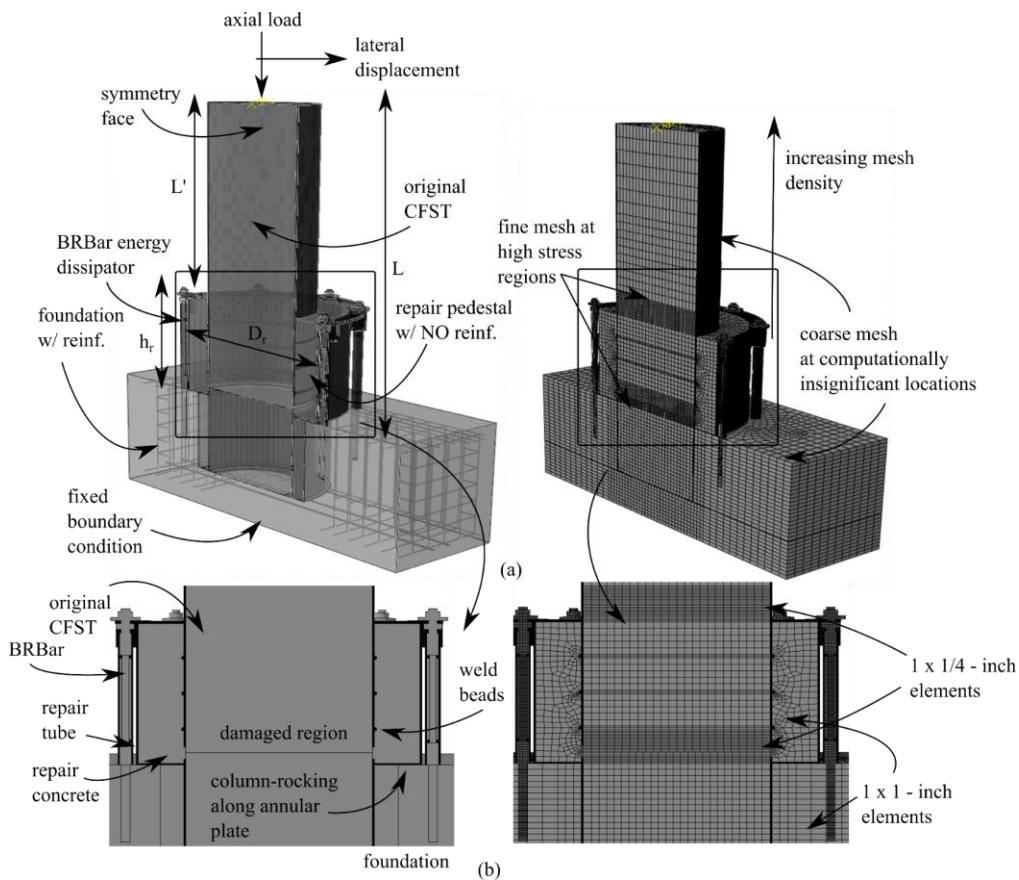


**Figure 5-22: (a) Overview of the performance-based repair model and a (b) detail of the pedestal.**

As shown in Figure 5-22b, a pre-crack was not included above the repair pedestal because it was expected that column-rocking would dominate response, eliminating the development of a plastic hinge above the pedestal. Therefore, the infill concrete of the CFST was modeled only as two separate parts; similar to the procedure outline in Chapter 3. However, the region above the repair pedestal was meshed with a higher density of elements due to the likelihood of high stress concentrations as shown in Figure 5-22b. The same interaction definitions presented in Section 4.3 were used to describe the interaction between the steel tube and concrete in the pedestal. In addition, a surface-surface interaction was defined between the interface of the base plate and foundation/cap-beam and between the repair base plate and steel tube, with steel-concrete and steel-steel property definitions respectively.

### **5.5.1 BRBar Model**

The BRBar subcomponent was modeled as five separate parts: (1) the yielding bar, (2) the top non-yielding bar, (3) the bottom non-yielding bar, (4) the infill grout of the BRM, and (5) the steel tube of the BRM. The overall depiction of the modeled BRBar is shown in Figure 5-23 with the element density composition shown in Figure 5-23a. Two model geometries were developed for the BRBar component: one geometry that included a small gap (approximately 1/16-in) between the internal grout and the yielding bar, and another geometry where this gap was removed, which are referred to as BRBar-Gap and BRBar-NoGap, respectively. The geometries of the Gap and NoGap BRBar models are shown in Figures 5-23b and 5-23c, respectively. The yielding, and non-yielding bars were modelled using the same inelastic material properties of steel reinforcing with yielding at 68-ksi, followed by a small stress plateau and strain hardening to failure at 90-ksi. The transition couplers were modeled simply as cylinders with equal diameters of those provided

by the manufacturer. The top, non-yielding bar was also modeled with two steel washers, that clamped to the flange to simulate the connection of the BRBar repair pedestal as shown in Figure 23b and 23c. The steel tube and grout of the BRM were simulated as simple thin-walled, concentric tubes. The steel tube had the same inelastic property definitions as the steel tube of the CFST column while the grout had the same properties as the grout of the CFST, embedded connection. A small, 1/2-inch gap was provided between the couplers and grout to allow for deformation of the yielding bar, without the coupler contacting the BRM. Half-symmetry models were used for the BRBars along the symmetry line of the original column; all other BRBars were modeled using the full geometry. All components of the BRBar were modeled using C3D8R elements with reduced integration, meshed with approximately a 0.20-inch mesh density.

A surface-surface interaction was defined between the two, washers of the BRBar to the flange of the repair steel tube, to simulate a clamped, bolted connection. A surface-surface interaction was also used between the steel tube and top coupler interface; this property definition did not include tangential properties to allow for undisturbed, sliding as the yielding core deforms. The BRM's grout utilized a surface-surface interaction to capture the interaction between the grout and yielding bar. The BRBar-NoGap model excluded tangential properties as well to simulate a decoupling mechanism, and allow for relative deformation between the two parts without developing friction forces. The base of BRBar, which included the bottom of the steel tube and coupler, also included a surface-surface interaction to the top of the foundation/cap-beam.

The yielding and non-yielding bars were spatially assembled, and tied together using a tie constraint. The interior face of the steel restraining tube was tied to the bottom coupler to model the set screw connection. The steel tube and infill grout of the BRM were also connected using the tie constraint assuming perfect bond between the grout and restraining tube. The bottom, non-

yielding bar that projected into the foundation/cap-beam was assumed to be perfectly embedded using a fully embedded constraint.

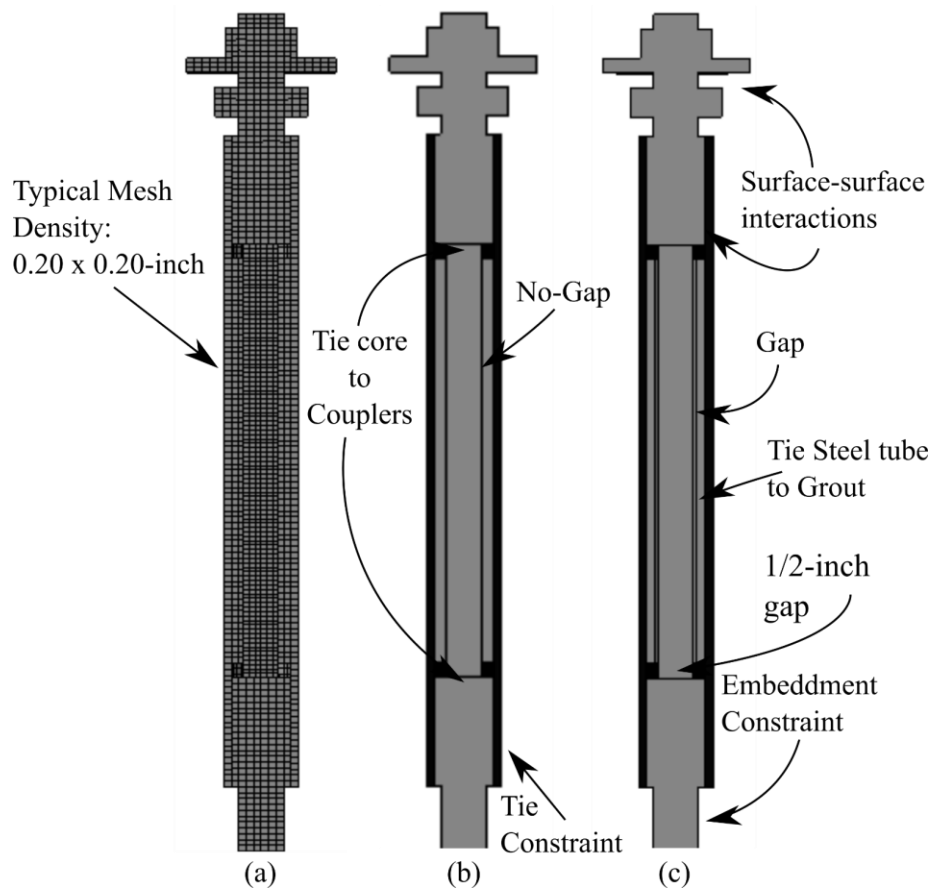


**Figure 5-23: Depiction of (a) the typical mesh density of (b) the NoGap and (c) Gap model cases**

## 5.6 Results and Discussion of the Global Repair Response

The performance of the performance-based repair was evaluated for both monotonic and cyclic loading. The monotonic case was run to a maximum target rotation of 8%. Two cyclic protocols were used; one with a single cycle to a maximum target rotation of 5.5% (herein referred to as single-cycle loading), and one using the reduced ATC protocol discussed in Section 4.4. A summary of the numerical results is shown in Table 10 below, where gap and no gap refer to the

BRBar. The response of the performance-based repair was compared to the response of the undamaged CFST column to assess the strength and ductility recovery of the repair. In addition, a rotation contribution analysis, was also performed using the results from the monotonic loading response to analyze the relative CFST and pedestal rotation contributions. This was done to assess the ability of the repair to successfully induce column-rocking, where the objective is to minimize rotation in the CFST column above the pedestal. The following sections provide a detailed discussion of the hysteretic response of the performance-based repair using the gap and no gap BRBars.

**Table 10: Summary of peak responses from numerical analysis of the performance-based repair.**

Model	Loading Regime	Strength ( $M_r/M_p$ )		Max Drift (%)		Ped. Rotation (%) *	CFST Rotation (%) *
		(+)	(-)	(+)	(-)		
Gap	Monotonic	1.05	N/A	10.5	N/A	3.40	3.15
	Single-Cycle	0.99	1.05	5.50	5.50	N/A	N/A
	Hysteretic	1.00	1.10	4.85	4.00	N/A	N/A
NoGap	Monotonic	1.01	N/A	10.5	N/A	96.6	96.85
	Single-Cycle	0.98	1.06	5.50	5.50	N/A	N/A
	Hysteretic	1.02	1.02	4.83	3.65	N/A	N/A

\* Values given at maximum drift of monotonic loading protocol

## 1. BRBar-Gap

The moment-drift responses for the monotonic, single-cycle, and hysteretic loading cases are shown in Figure 5-24, along with the hysteretic response of the undamaged column. The rigid body rotation analysis is shown in Figure 25. In addition, the peak moment capacities and rotation contributions at failure of the monotonic response are provided in Table 10. Results show that the performance-based repair configuration with the BRBar-Gap model is able to restore the original moment capacity, with peak moment resistance ratios ( $M_r/M_p$ ) of 1.05, 0.99, and 1.00 for the monotonic, single-cycle, and hysteretic load regimes, respectively. Two points to note regarding the load responses shown in Figure 5-24: (1) a numerical anomaly was removed from the monotonic curve (as indicated in the Figure) and (2) the full hysteretic model failed to converge at the location shown on the plot. The stress distributions in the concrete and steel are also shown in Figures 5-26a and 5-26b, respectively, and a plot of the plastic strain (PEEQ) distribution is shown in Figure 5-26c. Results are shown for the hysteretic loading protocol at a drift demand of 5%.

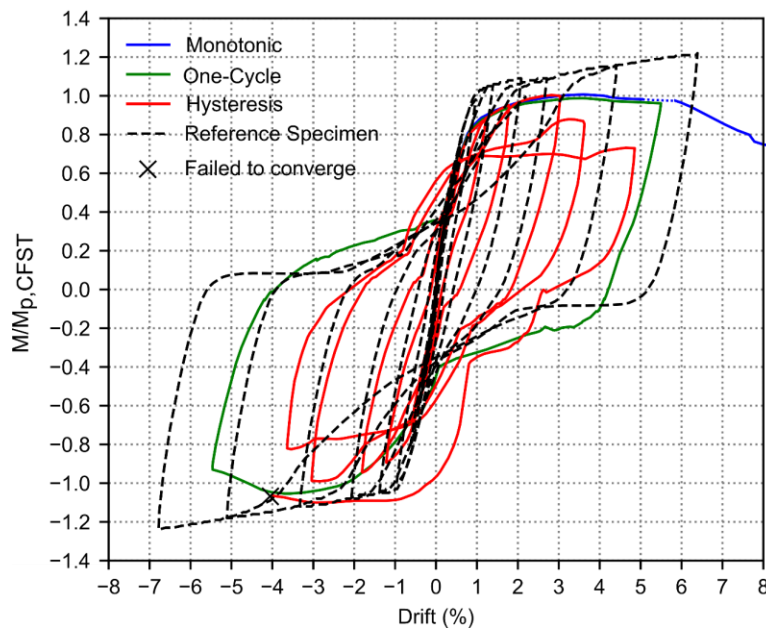


Figure 5-24: Monotonic, single-cycle, and hysteretic load responses compared to the reference specimen.

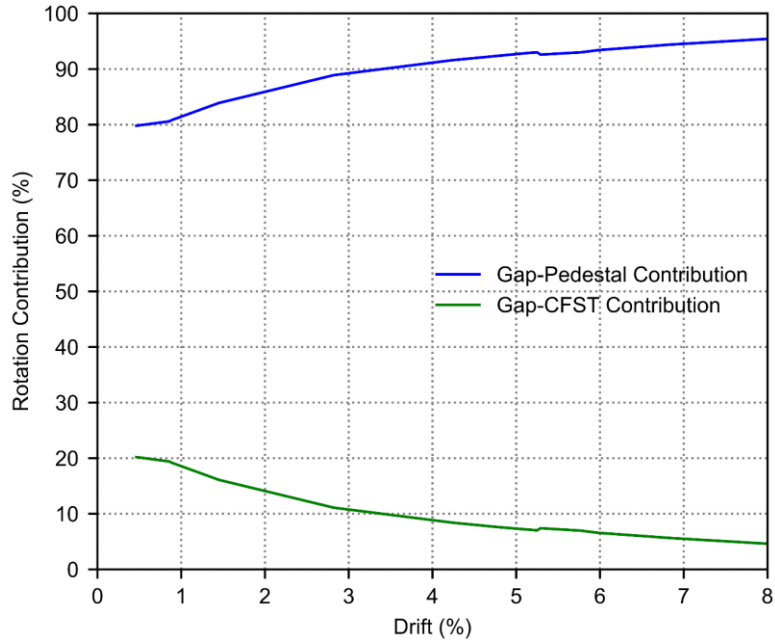


Figure 5-25: Pedestal and CFST rotation contribution versus total drift of column.

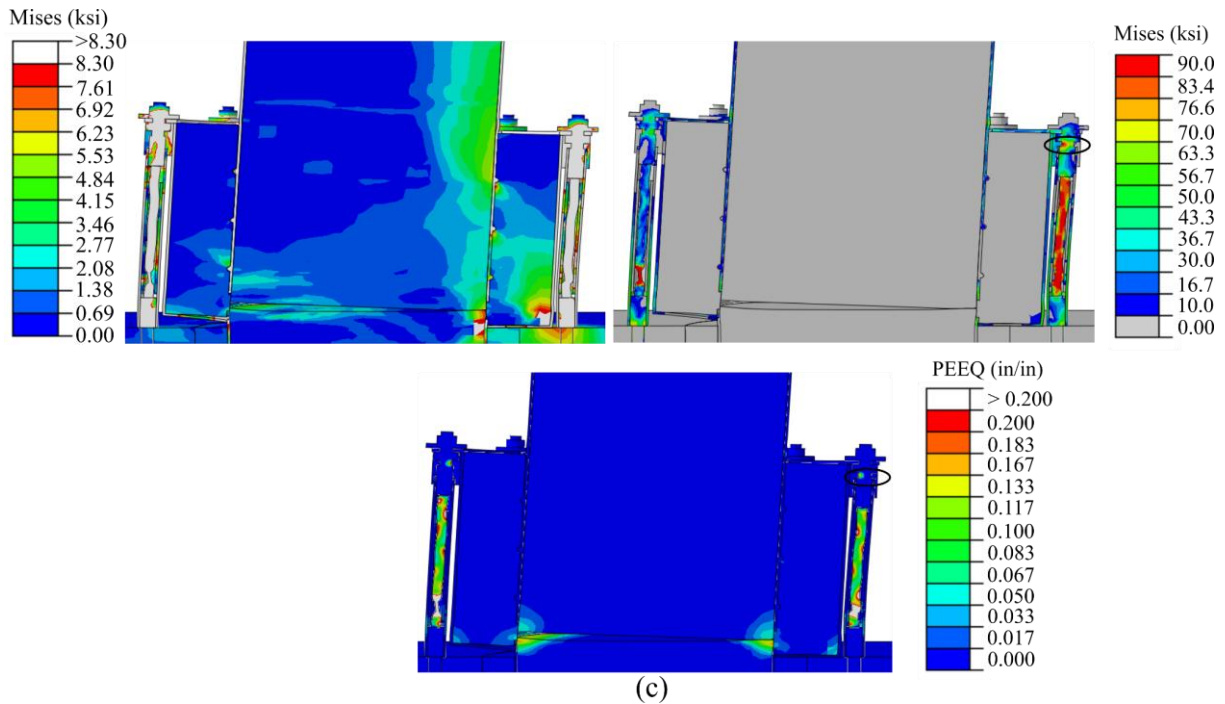


Figure 5-26: Depiction of the (a) concrete and (b) steel Von-Mises stress plots, and (c) the PEEQ strain.

The BRBar repair method which incorporates the BRBar Gap energy dissipaters performs well in terms of achieving strength and stiffness objectives, however, strength degradation is observed around 3.5% drift which is well below the drift capacity of the original column. The latter is most likely contributed to by the high tensile stress concentrations and local buckling of the yielding core, as shown in Figures 5-26a to 5-26c. This suggests that the BRBar is not experiencing purely, axial load demands, but rather a combination of axial and bending that results in a high stress concentration at the base of the yielding core. Ultimately, this causes severe necking of yielding bar and instability in the numerical model that results in premature failure of the model. The presence of a gap between the yielding core and BRM also causes severe local buckling along the length of the yielding bar, which places high stress demands at the bearing surface of the core to the restraining tube. The flange of the repair steel tube performs well in resisting extreme deformations during loading, but there is high stresses and inelastic strains between the bottom washer, and coupler, as shown in Figures 5-26b and 5-26c by the circled region, respectively. It is therefore recommended to limit the length between the top coupler and bottom washer, and provide section of bar that is at least two-times the diameter of the yielding core. The maximum concrete stress shown in Figure 5-26a is the maximum crushing capacity (8.3-ksi) of the concrete in the pedestal and CFST. As shown in Figure 5-26a and 5-26c, there is no inelastic behavior developed at the CFST-pedestal interface. However, high stresses are observed within the pedestal as it bears to the adjoined concrete element.

The PEEQ strain plot shown in Figure 5-26c, effectively demonstrates the ability of the BRBars' yielding cores to act as a structural fuse, isolating extreme inelastic strain demands to the external dissipaters. Very minimal yielding is observed in several steel components outside of the fuse, such as the steel tube and top, non-yielding bar due local buckling of the yielding core. Slight

tube buckling was also observed at the base of the repair steel tube, and original steel tube of the CFST located directly above the pedestal. Outward buckling of the repair steel tube is likely due to the high compressive stresses of the pedestal bearing on the foundation/cap-beam, while the buckling of the steel tube of the CFST column is contributed to failure to fully initiate column-rocking at the base. The rotation behavior captured during the monotonic loading protocol is shown in Figure 5-25 and demonstrates that under initial drift demands, column-rocking is not fully achieved as the CFST contributes to at least 10% of the total drift, until 3% column drift is completed. After this point, there is a steady increase in pedestal contribution until a peak contribution of roughly 97% is recorded at the end of the analysis.

## **2. BRBar-NoGap**

The moment drift responses for the monotonic, single-cycle, and hysteretic loading cases are shown in Figure 5-27 and the rigid-body rotation analysis is shown in Figure 5-28. Table 10 summarizes these peak response values. The results show that the BRBar-NoGap model also successfully returned the damaged CFST to its original strength and stiffness, with peak moment resistance ratios ( $M_r/M_p$ ) of 1.01, 0.98, and 1.02 for the monotonic, single-cycle, and hysteretic load regimes. The hysteretic model also failed to converge due to excessive tensile deformations in the yielding bar. This is shown in the stress plots for concrete and steel, shown in Figures 5-29a and 5-29b, respectively, and the PEEQ strain plots, shown in Figure 5-29c. Results are presented from the 5% drift demand of the hysteretic load.

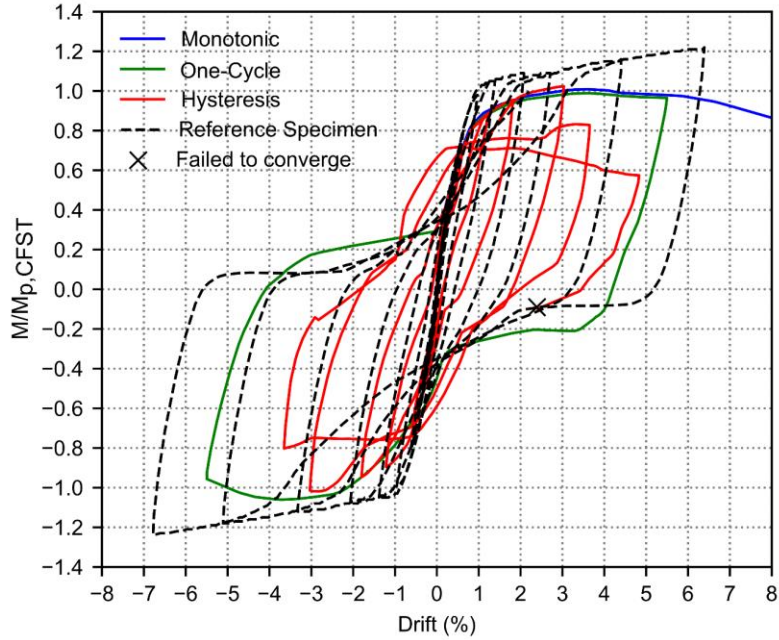


Figure 5-27: Monotonic, single-cycle, and hysteretic load responses compared to the reference specimen.

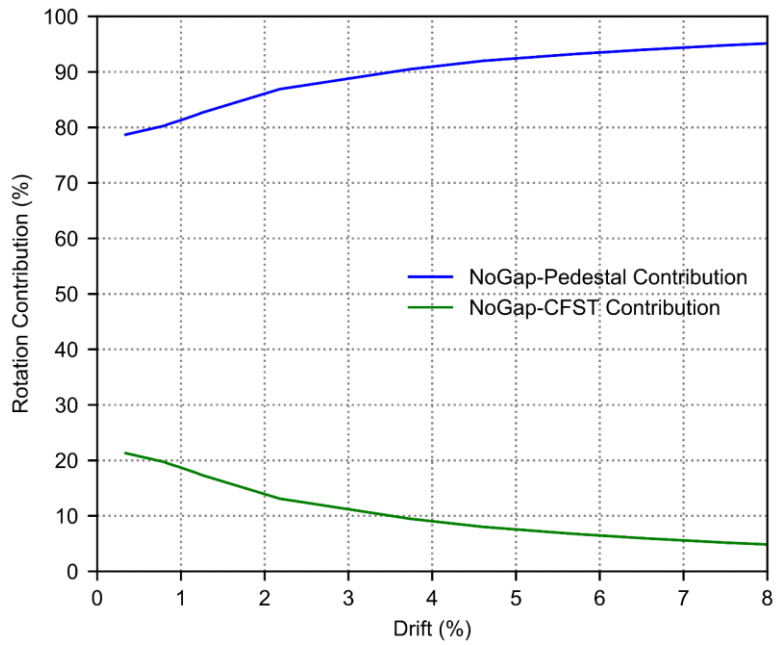
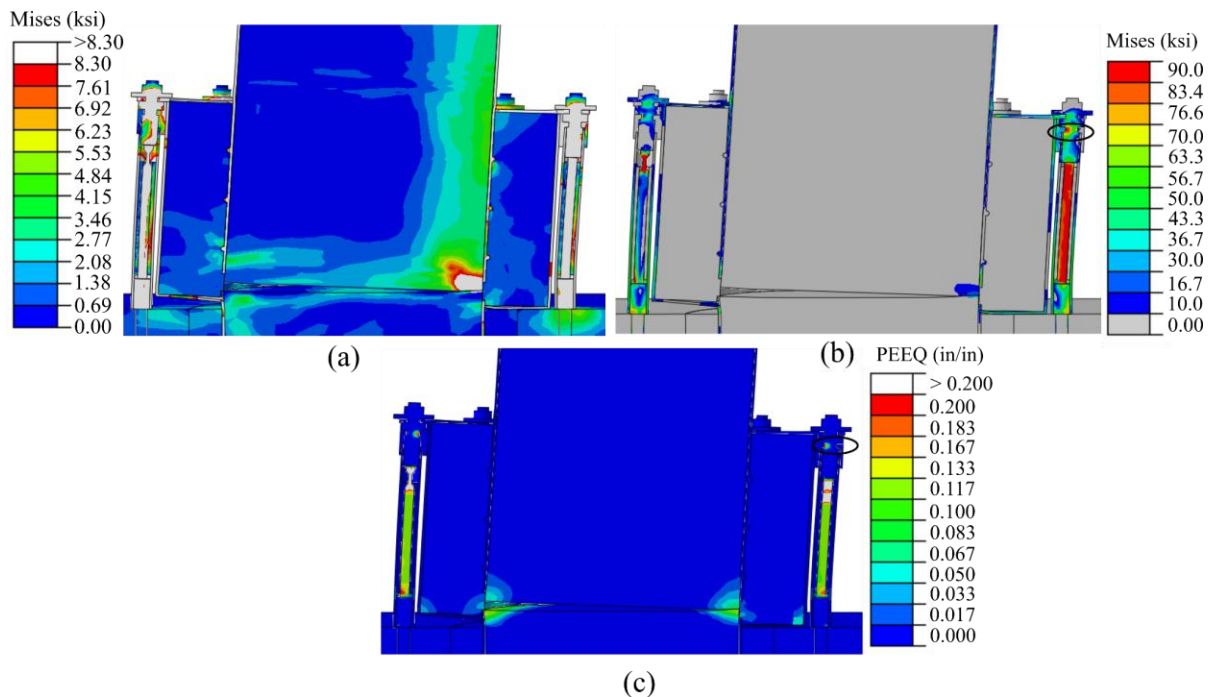


Figure 5-28: Pedestal and CFST contribution total drift of column



**Figure 5-29: Depiction of the (a) concrete and (b) steel Von-Mises stress plots, and (c) the PEEQ strain.**

The hysteretic performance of BRBar-NoGap shows that the repair method can effectively achieve strength and stiffness objectives, however the modeled performance is largely dependent on the loading protocol. For the monotonic and single-cycle protocols, the repair restored the stiffness and strength of the original column with minimal degradation through 5% drift. However, the strength of the original column was not achieved for the reversed cyclic protocol, and significant degradation was observed at ~3.5% drift. The combined axial and bending loading demands (discussed for the BRBar gap case) likely contributed to greater strain demands of the yielding bar, which resulted in premature tensile failure. However, by reducing the gap between the core and BRM, there was a noticeable improvement in the buckling behavior of the yielding core during compressive loadings. The deformed shapes shown in Figures 5-29a to 5-29c, show limited local buckling behavior, though severe necking of the yielding core occurs at the top of bar; the reasoning for this is expanded upon in following sections.

The flange and restraining tube performed well in limiting large out of plane deformations of the BRBar during compressive loads, and, according to Figure 5-29c, inelastic strain appears to be effectively isolated to the yielding core of the BRBars, with minimal inelastic strain of steel components, being recorded outside of the fuses besides the circled regions directly above the top coupler. High compressive stress concentrations were recorded within the concrete at the location of large bearing demands (e.g. between the pedestal and foundation/cap-beam and along the failure surface of the CFST column) as shown in Figure 5-29a and 5-29c. The BRBar-NoGap model also show some local buckling of the steel tube in the pedestal, and CFST above the pedestal. The rigid-body rotation results also provide evidence to this as similarly to the Gap model, column-rocking is not fully realized until after 3% of column drift is achieved.

### **3. Comparisons and Discussion**

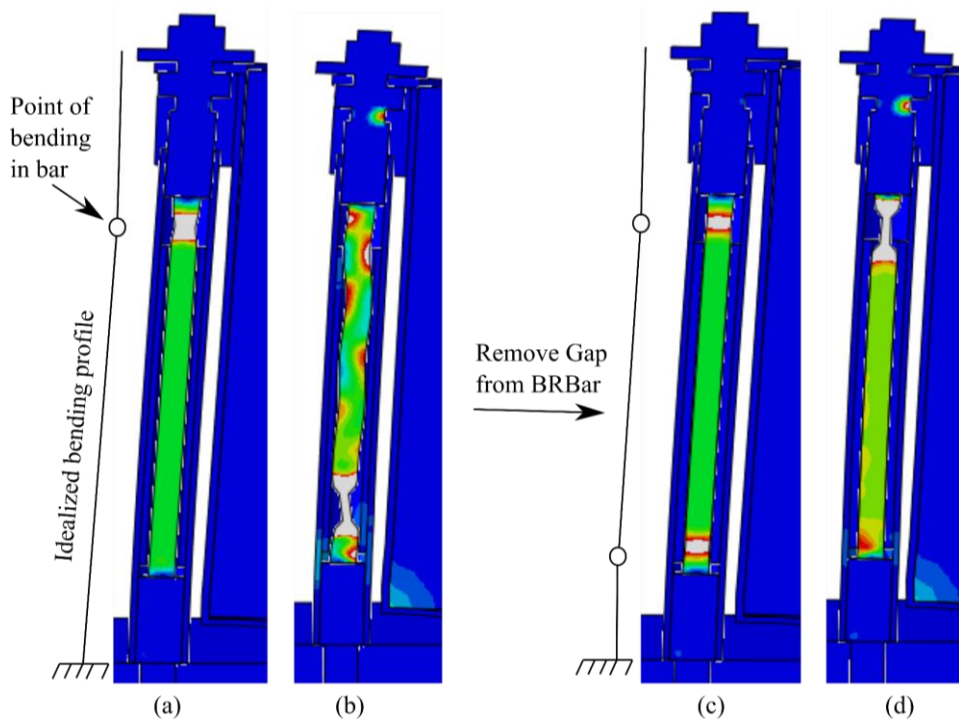
Including a gap between the yielding fuse and BRM had a significant impact on the local behavior of the yielding core. When comparing the hysteretic and monotonic load responses of the two models, some light can be shed on the location of extreme necking and why the locations differ between the two models. The deformed failure shapes of the BRBar components of the monotonic and hysteretic response of the Gap case are shown in Figure 5-30a and 5-30b, while the NoGap case deformation responses are shown in 5-30c and 5-30d. For each case, these figures are accompanied with a deformed shape profile as observed from the numerical results.

The BRBars were observed to lose their load carrying capacities as a result of excessive deformations and necking of the yielding fuse. While the reasoning of the large inelastic deformations is not fully understood, the formation of hinges within the yielding bars may be a

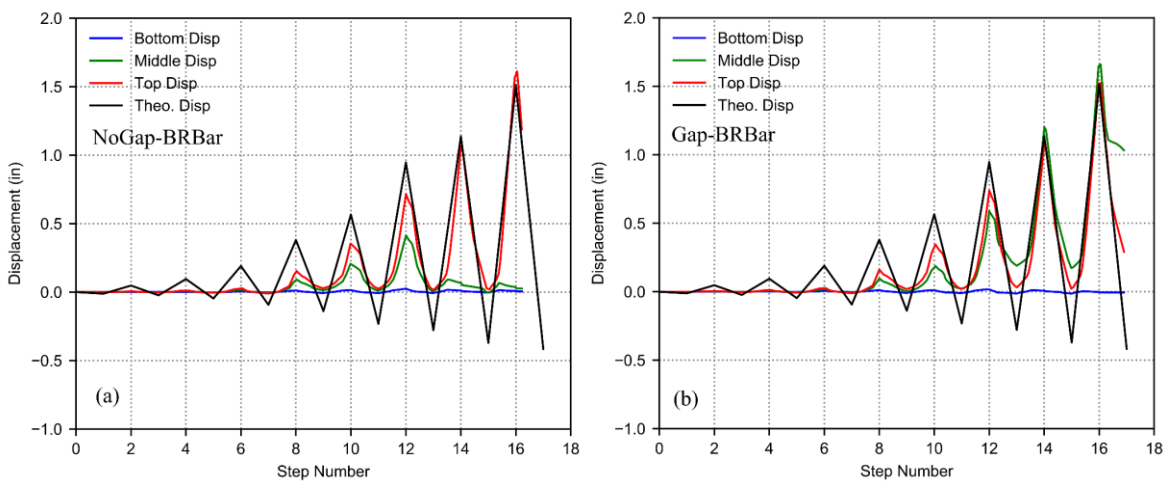
result of their geometry. As shown, the application of reverse-cyclic loadings, and inclusion/exclusion of the gap, alters the location of this necking. For example, when the Gap model case is subjected to a monotonic load, necking is observed at the top of the yielding core; this shifts to the bottom of the core, when reverse-cyclic loadings are included, suggesting that the inclusion of compressive loads and buckling plays a role in these strain concentration effects. Then, when the gap is removed, an equivalent strain demand is observed in the top and bottom of the yielding, rather than just the top as is the case of the Gap model. It appears that when restraining the yielding core along its whole length, two points of bending form at either end of the bar near the couplers, developing an S-shaped deformation pattern. This pattern is different in the Gap case, where extreme bending concentrates to only the top of the bar, and the rest of the bar below can deform more gradually to shape since it is unrestrained by the BRM, ultimately helping to disperse high strain demands. Under cyclic loadings, necking of the NoGap-model is isolated into only the top of the bar, again suggesting that this loading regime alters the location of extreme strain.

Figure 5-31a and 5-31b plots a comparison of the theoretical displacement history (from (5-1)) versus the recorded displacement of various points along the BRBar's yielding core length, obtained from the ABAQUS models. These points are: (1) the top of the bar or the point in line with where the grout of the BRM ends, (2) the mid-point of the bar, and (3) the bottom of the bar or the point in line with where the grout of the BRM ends. It is expected that the displacement of points along the bar's length would be the same, however, this is not the case. The analysis shows that displacement varies along the height of the yielding core, where very minimal displacement occurs at the bottom of the bar and increases along the height. At larger displacement demands, the top of the bar matches well to the theoretical displacement calculated using, (5-1). This is not

the case under lower displacement demands and may be contributed to a lack of column-rocking (i.e. rotation being isolated in the CFST) that limits the rotation demand on the BRBars.



**Figure 5-30: Deformed shape of the Gap model under (a) monotonic and (b) hysteretic loads, and the NoGap model under (c) monotonic and (d) hysteretic loads .**



**Figure 5-31: Displacement comparisons of the (a) NoGap and (b) Gap models along the BRBar height.**

In general, the two model cases show similar displacement demands at the three points being analyzed, however, the mid-point displacement drops off for the NoGap model which otherwise continues for the Gap-case. A comparison of this behavior is highlighted by Figure 5-32 and its variation is likely due to the difference in necking location between the two models. For the NoGap case, necking failure occurs at the top of the bar around Step 12.5, essentially isolating displacement to this region and leaving the bottom half of the yielding bar stationary. Then, for the Gap case, necking occurs at the bottom of the bar, so the midpoint and top of the bar continue to displace until failure. It should also be noted that compressive displacement is not captured along the height of the bar. This is likely due to the large inelastic, tensile displacement that occurs, so, as the BRBar is unloaded, only elastic displacement is regained, leaving the permanent tensile deformation that must be overcome as the yielding core is subjected to compression.

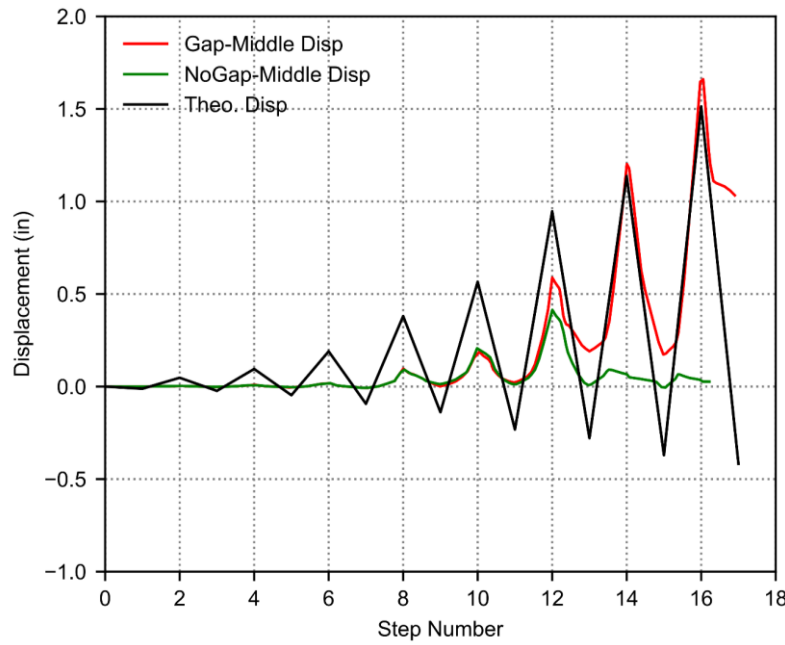


**Figure 5-32: Comparison of the displacement at mid-point of the BRBar for the Gap and NoGap models.**

When considering the estimated flexural capacity of the repair, the theoretical moment capacity of the performance-based repair can be accurately estimated using the moment-curvature analyses presented in Chapter 5.2. From these methods, the strain compatibility method estimated a strength of  $1.08 M_r/M_p$ , while the plastic stress distribution method estimated  $0.90 M_r/M_p$ . The strain compatibility method most accurately captures the maximum moment, with only an 8% overestimation compared to the plastic stress distribution which underestimates strength by roughly 10%. In terms of design, however, it is recommended to use the plastic stress distribution method since it is a more conservative design approach. Its underestimation is likely contributed due to the fact that the BRBars are converted to an equivalent area, thin-walled tube which shifts the centroid on this compressive region, closer to the center of the CFST, reducing the moment-arm and overall, moment contribution. The strain compatibility method, however, still analyzes the BRBars as individual components, therefore capturing a larger moment-arm in the BRBars which are further from the center of the CFST.

## 6.0 Summary, Conclusions and Future Work

Concrete filled steel tube (CFST) columns, in comparison to traditional reinforced concrete (RC) columns, are a unique alternative to improve structural efficiency and simplify construction of highway bridges. The steel tube, located at the optimal location flexural resistance, provides concrete confinement, while the infill concrete prevents inward buckling of the steel tube. Furthermore, the steel tube inherently serves as the formwork for construction and eliminates the need for longitudinal and transverse reinforcement in the column.

In recent years, research has generated a structurally robust, CFST column-to-foundation/cap-beam connections for the use in mid-to-high seismic regions. One of these connection types is the embedded ring (ER) connection, which consists of an annular steel ring, welded to the base of the steel tube of the CFST. Force transfer between the CFST and adjacent concrete element is relied solely on the annular ring and steel tube, therefore no load transferring dowels or reinforcement is required to pass from the CFST to the foundation/cap-beam. Through extensive numerical and experimental investigations, the ER connection has proven to provide adequate strength and ductility for seismic applications. When appropriately designed, the failure mode consists of outward buckling of the steel tube, followed by ductile tube tearing usually at the apex of the buckling for increasing reversed cyclic loading. This particular ductile failure mode of the ER CFST connection is advantageous for repair, due to the damage state being readily identifiable and accessible. In addition, the steel tube provides a convenient interface that can be used for bolted or welded connections. However, to date, no such repair strategies have been developed for the ER CFST connection.

The primary objective of this thesis was to develop a series of practical repair strategies for earthquake damaged ER CFST bridge columns. Two repair strategies were proposed including a plastic hinge relocation repair and a performance-based repair. The repair strategies were evaluated using a numerical parameter study to evaluate their effectiveness in restoring the stiffness and strength of the repaired CFST.

### **6.1 Plastic Hinge Relocation Repair Findings**

The plastic hinge relocation repair consists of a concrete filled steel tube pedestal that encases the damaged region of the CFST column to reestablish the moment capacity of the CFST by shifting inelastic deformation above the pedestal. To provide flexural resistance, the repair pedestal is reinforced with steel reinforcing which are epoxied into the adjacent concrete element. A series of force transfer mechanisms (FTMs), namely an annular steel ring, shear studs, or weld beads strips, are welded to the steel tube of the CFST to provide force transfer between the CFST and pedestal. A parametric study was conducted to determine the optimal FTM. The primary parameters investigated included the type of FTM (welded ring, shear stud, or weld bead), the size of the components (e.g. ring projection from original column), and location within the height of the pedestal. Based on the numerical results, the following observations and conclusions were drawn from this study.

- Increasing the rigidity of the force transfer mechanism by using components with a shorter length and/or greater thickness (e.g. a shorter thicker ring), was most effective in restoring strength and stiffness.

- Including force transfer mechanisms along the entire height of the repair pedestal also improved performance, by increasing the engagement of the CFST to the repair pedestal, thus improving the overall stiffness response.
- Increasing the rigidity of the force transfer mechanism shifted the location of extreme concrete stresses from the damaged region at the base of the pedestal, to the top of the pedestal along the CFST-repair concrete fill interface. This suggests that a more rigid force transfer mechanism resulted in a larger CFST rotation above the pedestal whereas a less rigid force transfer mechanism results in a larger rotation response within the height of the pedestal.
- Of the three FTM types tested, weld beads performed the best. It is recommended to include three weld strips distributed up the height of the pedestal at 1/4, 1/2, and 3/4 points. When subjected to reverse-cyclic loadings, the weld bead repair successfully reestablished the original strength and stiffness of the CFST column, and noticeable outward tube buckling was observed above the pedestal, suggesting that the plastic hinge also successfully shifted to above the repair pedestal.
- The plastic hinge repair, in general, may induce a larger moment into the foundation/cap-beam than originally designed for, which would cause serious damage if not considered.
- The theoretical plastic moment capacity of the pedestal was calculated using the strain compatibility method and plastic stress distribution method, and results showed that neither were effective at accurately predicting the strength of the pedestal.

## 6.2 Performance-Based Repair Findings

A performance-based repair strategy was proposed which consists of a CFST pedestal surrounding the damaged region of the original CFST with external energy dissipators bolt-connected to the steel tube on the exterior of the pedestal. An annular steel ring is welded to the base of the repair pedestal to create a rocking interface along the damaged region of the CFST. Weld beads within the height of the pedestal are welded to the original CFST to provide force transfer between the original column and pedestal. A steel flange is welded to the top of the repair steel tube to allow for a bolted connection to the energy dissipators, which are epoxied into the adjacent concrete element. No reinforcement passes from the repair pedestal to the foundation/cap-beam, therefore isolating resistance and damage to the dissipators which can easily be replaced post-earthquake to return the structure to service. A buckling restrained, reinforcing bar (BRBar) fuse was proposed as the energy dissipator and consists of a reduced section of rebar coupled at either end to larger, non-yielding sections of bars. A buckling restraining mechanism (BRM) encases the core and consists of a steel tube filled with grout. The BRBar was experimentally tested under cyclic-compressive loadings to confirm the validity of the individual subcomponent as an effective energy dissipator. It was found that when completely restrained from lateral deformations, the fuse of the BRBar can successfully yield in compression with a  $1.12F_y$  maximum axial load and  $9.0\epsilon_y$  axial strain being recorded. The performance-based repair configuration with BRBars as external energy dissipators was evaluated numerically under monotonic, single-cycle, and hysteretic loading regimes with the objective of evaluating the performance. Two design procedures were investigated by incorporating two different design procedures for the BRBar which consisted of: (1) BRBar-Gap - modeling a gap between the BRBar fuse and its BRM and

(2) BRBar-NoGap – removing the gap between the fuse and BRM. The following observations and principal conclusions were drawn from this study.

- The BRBar component tests demonstrated that the BRBar can achieve compressive yielding of the rebar fuse prior to the development of buckling.
- The numerical results of the performance-based repair demonstrated that the repair can successfully reestablished the original strength and stiffness of the repaired, CFST column.
- It is paramount to fabricate the BRBar with minimal unsupported lengths in the core, and along the coupler. Otherwise, this will create severe instability of the rebar-coupler system, resulting in lateral displacements and a reduction in the compressive capacity of the BRBar.
- It is recommended that the top and bottom, non-yielding bars are at least two times the diameter of the fuse, and their lengths are minimized in order to reduce the likelihood of their buckling during experimental testing, and in the field.
- Column-rocking was successfully initiated along the base of pedestal. At max drift demands, the pedestal contributed roughly 97% of the rotation while the CFST accounted for only 3%.
- The Gap model case shows significant local buckling within the fuse under reverse-cyclic loadings which is otherwise removed in the NoGap case. This was also demonstrated during experimental testing, where it was found that buckling occurred when the yielding core was not fully braced. Therefore, it is recommended to model the BRBar with a limited space between the fuse and BRM.
- When subjected to reverse-cyclic loadings, complex loadings are imposed on the BRBars which consist of a combination of axial and bending loadings. This results in a series of numerical instabilities and apparent loss in ductility capacity of the BRBars.

- However, when subjected to monotonic or one-cycle loading protocols, the loading complexities are not as apparent, and numerical instabilities and extreme deformation of the fuse are mitigated.
- The modified, ATC-24 loading protocol developed successfully predicts the displacement demand of the BRBar under large drift demands, but over predicts displacement under smaller column drift demands.
- Within the performance-based repair, the BRBar fuse appears to have varying displacement demand along its length, with larger demands at the top of the bar and very marginal at the bottom.

### **6.3 Future Work**

Several key research recommendations for future work studies are provided herein that should be pursued in order to further establish the validity of the two, proposed repair strategies as viable methods for repairing earthquake-damaged, ER CFST bridge columns. These include:

1. Conduct further reverse-cyclic loading, numerical investigations of the BRBar at the subcomponent level and as an energy dissipator in the proposed, global repair in order to fully comprehend its loading behavior and stress and strain demands.
2. Further refine the proposed, design methods presented here to better predict the strength, stiffness, and ductility capacities of the repair methods.
3. Provide experimental evidence to support the findings of the numerical models, by means of full-scale testing of the two proposed repair methods, and conduct further

experimental testing of the BRBar subcomponent using the recommendations provided.

## Appendix A : Design Calculations for Estimating Flexural Demand and Strength

### A1: Plastic Hinge Relocation Repair

The following presents a detailed design guide for the plastic hinge relocation repair used in this study, as presented in Section 4.2. Calculations for predicting the flexural demand on the repair section will be shown, as well as design calculations for sizing the CFST repair pedestal and reinforcement, using either (1) the strain compatibility method or (2) the plastic stress distribution method are provided. Table A-1 provides a summary of the damaged, CFST dimensions and the dimensions of the repair CFST pedestal where Figure 4-5 provides reference of the dimensions. Initial height and diameter of the repair pedestal were estimated to be 1.0D and 1.5D, respectively, where D is the diameter of the original CFST column.

**Table A- 1: Original CFST and repair pedestal dimensions.**

$L_{CFST}$ (in)	$D_{CFST}$	$t_{CFST}$	$P_{axial}$ (kips)	$D_r$ (in)	$H_r$ (in)	$L'$ (in)	$M_{CFST}$ (k-in)
72	24	0.25	250	36 (1.5D)	24 (1.0D)	48	11000

*Estimating Demand:* Flexural demand ( $M_r$ ) of the repair pedestal is estimated from (4-1).

$$M_r = \frac{M_{CFST}(L)}{L'} = \frac{11000(72)}{48} = 16500 \text{ k-in}$$

*Estimating Strength:* Strength is estimated from (1) the strain compatibility method and (2) the plastic stress distribution method. The material properties used for design are shown in Table A-2, and Table A-3 provides the location of the reinforcing bars with respect to the center of the

repair pedestal, where Figure 4-3 is provided for reference. Bars are numbered 1 to 13, with Bar1 and Bar13 referring to the extreme tensile and compressive bars, respectively. Note that symmetry can be applied to Bar2 to Bar 12.

**Table A- 2: Repair material properties.**

$D_{\text{bar}}$ (in)	$QTY_{\text{bar}}$	$F_y$ (ksi)	$F'_c$ (ksi)	$E_s$ (ksi)
1.125	24	68	8.3	29000

**Table A- 3: Location of reinforcing with respect to the center of the CFST pedestal.**

Bar #	Y (in)	Bar #	Y (in)
1	17.19	8	-4.45
2	16.60	9	-8.59
3	14.89	10	-12.15
4	12.15	11	-14.89
5	8.59	12	-16.60
6	4.45	13	-17.19
7	0		

### 1. Strain Compatibility Method

A variable, “c”, is used to represent the distance from the extreme concrete compressive fiber to the neutral axis and is used to calculate curvature and tensile and compressive forces of the cross-section based on their strain development.

*Reinforcement Contribution:* A linear strain distribution is assumed, and the strain in each reinforcing bar can be calculated as a function of “c”. First the distance ( $D_C$ ) to the neutral axis from each bar is calculated using (A-1):

$$D_C = Y + (R_{in} - c) \quad (A-1)$$

$$R_{in} = \frac{D_r}{2} - t = \frac{18}{2} - 0.25 = 17.75 \text{ inches}$$

Then, the force in each reinforcing bar is calculated (A-2), where the maximum allowable force in each bar is take as  $F_y A_b$ . Bars are in tension if  $D + R_{in}$  is greater than “c”, and the forces in Bar2 to Bar12 should be doubled due to symmetry.

$$F_{bar} = \left(\frac{0.003}{c}\right) D_c E_s A_b \quad (A-2)$$

The moment contribution is taken simply then as  $F_{bar} Y$ , where Y is the absolute value of those provided in Table A-3.

*Concrete Contribution:* The area of concrete in compression ( $A_c$ ) is calculated as a function of “c” using the methodology of calculating the area of a circular segment, with an angle  $\Phi$  used to simplify calculations, as shown in Figure 4-4. It should also be noted that the area of concrete should be reduced by the number of compressive bars (n) present within it, and the contributing force ( $F_c$ ) is calculated using equations (A-3 to A-5).

$$F_c = 0.95 F'_c A_c \quad (A-3)$$

$$A_c = \frac{1}{2} R_{in}^2 (\Phi - \sin \Phi) - n A_b \quad (A-4)$$

$$\Phi = 2 \cos^{-1} \left( \frac{R_{in} - c}{R_{in}} \right) \quad (A-5)$$

The centroid of the compressive area of concrete, with respect to the center of the pedestal, can then be calculated as follows (A-6) in order to determine the flexural resistance provided by the repair concrete infill.

$$Y_c = \frac{4R_{in} \sin^3 \left( \frac{1}{2}\Phi \right)}{3(\Phi - \sin \Phi)} \quad (A-6)$$

To determine “c”, the axial forces are then summed to equal the axial force ( $P_{axial}$ ) subjected to the CFST column. Table A-4 and A-5 summarize the results as they pertain to this study, for a value of  $c = 7.22$ -inches where the plastic moment capacity was determined to be 28,242 k-in.

**Table A- 4: Summary of reinforcing bar contributions.**

Bar	Dc	Fbar	Mbar	Bar	Dc	Fbar	Mbar
1	27.71	67.59	1161.76	8	6.08	135.19	601.38
2	27.13	135.19	2244.36	9	1.93	46.21	397.10
3	25.41	135.19	2012.23	10	1.63	-39.00	473.94
4	22.68	135.19	1642.98	11	4.36	-104.38	1553.62
5	19.12	135.19	1161.77	12	6.08	-135.19	2244.36
6	14.97	135.19	601.38	13	6.66	-67.59	1161.76
7	10.52	135.19	0.00				

**Table A- 5: Concrete Contribution**

$A_c$ (in <sup>2</sup> )	$Y_c$ (in)	$F_c$ (kip)	$M_c$ (kip-in)
136.6	13.47	-964	12986

*Check Pedestal Height:* The pedestal height needs to be verified to ensure that the height is sufficient to develop the repair reinforcement. For this application, headed bars are assumed to be utilized and (4-2) is used for calculation.

$$H_r = \frac{0.016f_y}{\sqrt{f'_c}}(d_b) = \frac{0.016(60000)}{\sqrt{8300}}(1.125) = 11.9 \text{ inches}$$

## 2. Plastic Stress Distribution Method

The plastic stress distribution method assumes that all steel components achieve their yield stress, and that concrete under compression achieves  $0.95f'_c$ . Under these assumptions, equilibrium is achieved by iterating on a variable “Y” that represents determine the distance of the centroid of the pedestal to the neutral axis, as shown in Figure 4-4.

*Reinforcement Contribution:* To simplify calculations, the repair reinforcement area ( $A_b$ ) is equated to an equivalent area ( $A_{be}$ ) of a thin-walled steel tube, as shown in Figure A-1. Using the radius ( $R_{bm}$ ) to the centroid of the repair reinforcement, the required tube thickness ( $t_{eq}$ ) can be iterated on until equivalency.  $R_{bm}$  is equal to 17.1875-inches in this repair method.

$$A_{be} = A_b$$

$$A_b = 24(0.25\pi) \left(\frac{9}{8}\right)^2 = 23.85 \text{ in}^2$$

$$A_{be} = \pi((r_{bm} + t_{eq})^2 - (r_{bm} - t_{eq})^2) \rightarrow t_{eq} = 0.22 \text{ inches}$$

An angle  $\Phi_{bm}$  is introduced that is used to define the area of reinforcement in compression with respect to the radius to its centroid ( $R_{bm}$ ), and can be calculated as a function of “Y” as follows. This is then used to calculate the area of bars in compression ( $A_{bc}$ ) and tension ( $A_{bt}$ ), using (A-7) and (A-8).

$$\Phi_{bm} = 2\cos^{-1}\left(\frac{Y}{R_{bm}}\right) \quad (\text{A-7})$$

$$A_{bc} = (R_{bm})(\Phi_{bm})(t_{eq}) \quad (\text{A-8})$$

$$A_{bt} = A_{be} - A_{bc}$$

The centroid is found by using the composite centroid area method, where two segmented circles with radii equal to the outside radius of the reinforcement ( $R_{b.out}$ ) or the inner radius ( $R_{b.in}$ ). An angle is found to define each radius ( $\Phi_{b.in}$  and  $\Phi_{b.out}$ ) as a function of “Y”, as depicted in Figure A-1, and is used to calculate the area and centroid for each case, using (A-9) and (A-10). The case for the outside radius is shown below.

$$A_{b.out} = \frac{1}{2}R_{b.out}^2(\Phi_{b.out} \sin \Phi_{b.out}) \quad (\text{A-9})$$

$$Y_{b.out} = R_{b.out} - \frac{4R_{b.out} \sin^3\left(\frac{1}{2}\Phi_{b.out}\right)}{3(\Phi_{b.out} - \sin \Phi_{b.out})} \quad (\text{A-10})$$

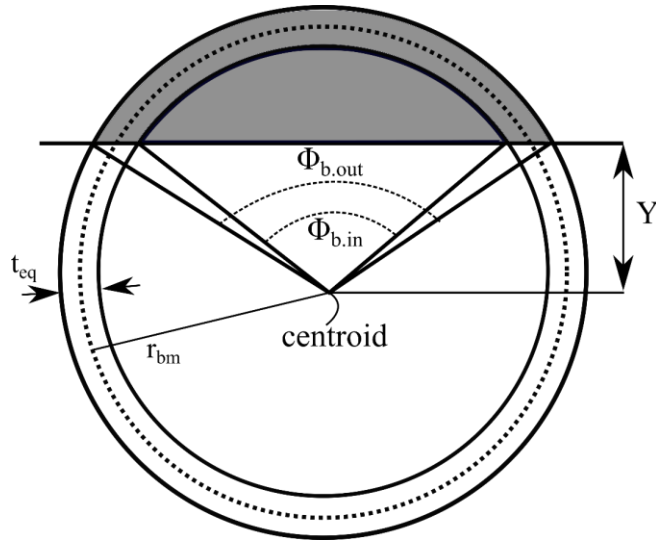


**Figure A-1: Depiction of composite area method to determine the centroid of repair reinforcing.**

This calculation is repeated for the inner radius, and the composite area method is applied (A-11) to determine the resulting centroid for the reinforcement in compression

$$Y_{bc} = \frac{A_{b.out}Y_{b.out} - A_{b.in}Y_{b.in}}{A_{b.out} + A_{b.in}} \quad (\text{A-11})$$

A similar method is repeated for the reinforcement in tension where the angles for the inner and outside cases, can be found by subtracting the respective compression reinforcing angles by  $2\pi$ .

*Concrete Contribution:* The area and centroid of the concrete in compression is found in a similar fashion as presented in the strain compatibility method, with a value of “Y” being iterated on, using (A-3) and (A-12 to A-14).

$$A_c = \frac{1}{2} R_{in}^2 (\Phi - \sin \Phi) - A_{bc} \quad (\text{A-12})$$

$$Y_c = \left( R_{in} - \frac{4R_{in} \sin^3\left(\frac{1}{2}\Phi\right)}{3(\Phi - \sin \Phi)} \right) \quad (\text{A-13})$$

$$\Phi = 2 \cos^{-1}\left(\frac{Y}{R_{in}}\right) \quad (\text{A-14})$$

“Y” is then determined by summing the axial loads to be equal to the axial load subjected to the column. The resulting moment capacity of the pedestal is found by multiplying the axial load of each component by its respective moment arm. The results are shown in Table A-6, with a plastic moment capacity of the pedestal being predicted to be equal to 26,975 kip-in, and “Y” equal to 11.04 inches.

**Table A- 6: Component contribution summary for the plastic stress distribution method.**

Component	Area (in <sup>2</sup> )	Force (kip)	Centroid (in)	Moment (k-in)
Compressive Bars	6.63	-451	15.1	6799
Tensile Bars	17.2	1172	5.81	6799
Concrete	123	-970	13.78	13,377

## **A2: Performance-Based Repair Strategy**

The design methodology for the performance-based repair strategy requires design of the global repair strategy, and a subcomponent design for an individual BRBar energy dissipator. The flexural capacity of the global repair is estimated using (1) the strain compatibility method, and (2) the plastic stress distribution method. Table A-7 provides a summary of the size of the pedestal, the desired performance objectives, and the size and quantity of BRBars. Table A-8 provides the locations of each BRBar with respect to the center of the pedestal. Note that BRBar1 and BRBar5

represent the extreme tensile and compressive resisting BRBars, respectively, and symmetry can be applied to BRBar2 to BRBar4.

**Table A- 7: Geometry of performance-based repair strategy.**

$D_r$ (in)	$H_r$ (in)	$P_{axial}$ (kips)	$L_{core}$ (in)	$t$ (in)	$M_r$ (k- in)	Target Drift (%)	$D_{fuse}$ (in)	Qty
36 (1.5D)	24 (1.0D)	250	15	0.25	11000	5.5	7/8	8

**Table A- 8: Location of BRBar energy dissipators.**

Bar #	Y (in)
1	19.375
2	13.70
3	0
4	-13.70
5	-19.375

*Estimating Flexural and Ductility Demand:* Due to the presence of column-rocking, there is no enlarged moment that is subjected at the base of the pedestal. Rather, the designer is able to choose the desired strength performance of the repair, given that the sole flexural resistance is provided by the external energy dissipators. For this study, the desired strength performance ( $M_r$ ) was selected to be the original plastic moment capacity of the CFST column ( $M_p$ ), with a desired ductility of 5.5% drift.

*BRBar Subcomponent Design:* The BRBar on a subcomponent level is designed for its expected ductility requirement, and to restrain against global buckling. The expected deformation of the fuse is estimated from (5-1) and its required length is calculated from (5-2). Figure 5-6 provides reference of this design methodology.

$$\Delta_{BRBar} = x \tan\left(\frac{\theta}{100}\right) = 31.125 \left(\tan \frac{5.5}{100}\right) = 1.72 \text{ inches}$$

$$L_{fuse} = \frac{\Delta_{d,BRBar}}{\varepsilon_d} = \frac{1.72}{0.15} = 11.5 \text{ inches}$$

For this study, a core length was chosen to be 15-inches. The buckling restraining mechanism is designed against a buckling force of  $2.0P_y$ , where the required moment inertia ( $I_{tube}$ ) of the steel tube can be calculated from (5-3). The length of the tube was estimated based on the length of the yielding core and the height of the LENTON transition couplers.

$$P_y = F_y A_b = 68 \left(0.25\pi \left(\frac{7}{8}\right)^2\right) = 40.8 \text{ kip}$$

$$I_{tube} = \frac{P_e L_{tube}^2}{E\pi^2} = \frac{2.0P_y L_{tube}^2}{E\pi^2} = \frac{2(40.8)22.5^2}{29000\pi^2} = 0.145 \text{ in}^4$$

Based on available steel tubes from local metal manufacturers, a steel tube with an external diameter of 1.90-inches and thickness of 0.154-inches was selected with a resulting moment inertia of  $0.325 \text{ in}^4$ .

*Estimating Strength:* Flexural capacity of the global, BRBar repair is estimated using either (1) the strain compatibility method or (2) the plastic stress distribution method. A similar design

methodology presented in Appendix A1 is also adopted here however, the repair reinforcement (BRBars) operates outside of the concrete, therefore its area does not need to be reduced from the area of the repair concrete fill. Also, it is assumed that that confining repair steel tube provides compressive resistance however, tension is neglected due to the column-rocking mechanism.

### 1. Strain Compatibility Method

Table A-9 provides a summary of the material properties of the BRBar, infill concrete, and steel tube used in this repair method.

**Table A- 9: Material properties of performance-based repair.**

$F_{y.bar}$ (ksi)	$F'_c$ (ksi)	$F_{y.tube}$ (ksi)	$E_s$ (ksi)
68	8.3	53	29000

*BRBar Contribution:* The same equations presented in Appendix A1 for determining the contribution of the steel reinforcement is implemented here, however, the compressive strain distribution extends upwards to the compressive BRBars as shown in Figure 5-3.

*Concrete Contribution:* Similarly, the concrete compressive area and centroid location are calculated in the same fashion as presented in Appendix A1, however, the area of the concrete is not reduced by the compressive BRBars, since they are located outside of the concrete.

*Steel Tube Contribution:* The confining steel tube compressive area and centroid is calculated using the angle  $\Phi_{tube}$  which represents the angle that defines the area of tube in compression. This angle is calculated using the centroid radius ( $R_{tm}$ ) shown similarly in Figure A-1 as  $R_{bm}$ . The

composite area method, also presented in Figure A-1, can then be implemented to determine the tube's centroid. This approach is presented similarly using (A-7) and (A-8)

$$R_{tm} = \frac{D_r}{2} - \frac{t}{2} = \frac{36}{2} - \frac{0.25}{2} = 17.875 \text{ inches}$$

$$\Phi_{tube} = 2 \cos^{-1}\left(\frac{R_{in} - c}{R_{tm}}\right)$$

$$A_{tube} = (R_{tm})(\Phi_{tube})(t)$$

$$P_{tube} = F_y A_{tube}$$

The axial forces determined from these methods are then iterated on and summed, until they equate to the axial force subjected to the column. Table A-10 and A-11 summarize the results of this analysis, where a plastic moment capacity of the global repair was estimated to be 11,770 kip-in and “c” was determined to be 2.41-inches.

**Table A- 10: BRBar moment contributions.**

Bar #	D <sub>c</sub> (in)	Force (kip)	Moment (k-in)
1	34.7	40.9	792
2	29.0	81.8	1120
3	15.3	81.8	0
4	1.64	71.3	976
5	4.03	-40.9	792

**Table A- 11: Steel tube and concrete moment contributions.**

Component	Area (in <sup>2</sup> )	Force (kip)	Centroid (in)	Moment (k-in)
Steel Tube	4.82	-255	17.0	4346
Concrete	29.1	-229	16.3	3742

## 2. Plastic Stress Distribution Method

*Reinforcement Contribution:* The area of the BRBars ( $A_b$ ) are redistributed into an equivalent area ( $A_{be}$ ) in a similar fashion presented previously for the plastic hinge relocation repair. This results in an equivalent, thin-walled tube as follows, where  $R_{bm}$  is equal to 19.375-inches. The resulting tensile and compressive areas and centroids can be calculated as shown previously.

$$A_{be} = A_b$$

$$A_b = 8(0.25\pi) \left(\frac{7}{8}\right)^2 = 4.81 \text{ in}^2$$

$$A_{be} = \pi((r_{bm} + t_{eq})^2 - (r_{bm} - t_{eq})^2) \rightarrow t_{eq} = 0.040 \text{ inches}$$

*Concrete and steel tube contributions:* Again, the concrete and steel tube contributions are calculated as shown in the plastic stress distribution method of Appendix A1, and the strain compatibility method of this section, respectively. Following these guidelines, the plastic stress distribution method determined a plastic moment capacity of 9866 k-in for the BRBar repair, where “Y” was determined to be 15.6-inches. Table A-12 summarizes the contributions of each component.

**Table A- 12: Component contribution summary for the plastic stress distribution method.**

Component	Area (in <sup>2</sup> )	Force (kip)	Centroid (in)	Moment (k-in)
Compressive Bars	0.978	-66.5	18.1	1203
Tensile Bars	3.83	261	4.62	1203
Concrete	25.4	-200	16.4	3288
Steel Tube	4.61	-244	17.1	4172

## Bibliography

ABAQUS, 2017. ABAQUS User Manual 6.14.

Abdulridha, A., Palermo, D., Foo, S., Vecchio, F.J., 2013. Behavior and modeling of superelastic shape memory alloy reinforced concrete beams. *Engineering Structures* 49, 893–904. <https://doi.org/10.1016/j.engstruct.2012.12.041>

Alexander, M., Beushausen, H.-D., Dehn, F., Moyo, P. (Eds.), 2008. *Concrete Repair, Rehabilitation and Retrofitting II: 2nd International Conference on Concrete Repair, Rehabilitation and Retrofitting, ICCRRR-2, 24-26 November 2008, Cape Town, South Africa*. CRC Press. <https://doi.org/10.1201/9781439828403>

American Concrete Institute, 2014. *Building Code Requirements for Structural Concrete (ACI 318-14)*. American Concrete Institute.

American Society of Civil Engineers, 2011. *Manual of Steel Construction, 14th Edition, 14th ed.* Chicago: AISC.

Azizinamini, A., Ghosh, S.K., 1997. Steel Reinforced Concrete Structures in 1995 Hyogoken-Nanbu Earthquake. *Journal of Structural Engineering* 123, 986–992. [https://doi.org/10.1061/\(ASCE\)0733-9445\(1997\)123:8\(986\)](https://doi.org/10.1061/(ASCE)0733-9445(1997)123:8(986))

Baird, A., Smith, T., Palermo, A., Pampanin, S., 2014. Experimental and numerical Study of U-shape Flexural Plate (UFP) dissipators 9.

Bruneau, M., Uang, C.-M., Whittaker, A., 2011. *Ductile design of steel structures, 2nd ed.* New York: McGraw-Hill.

Chou, C.-C., Chen, Y.-C., 2006. Cyclic tests of post-tensioned precast CFT segmental bridge columns with unbonded strands. *Earthquake Engng Struct. Dyn.* 35, 159–175. <https://doi.org/10.1002/eqe.512>

Dawood, H., ElGawady, M., Hewes, J., 2012. Behavior of Segmental Precast Posttensioned Bridge Piers under Lateral Loads. *J. Bridge Eng.* 17, 735–746. [https://doi.org/10.1061/\(ASCE\)BE.1943-5592.0000252](https://doi.org/10.1061/(ASCE)BE.1943-5592.0000252)

Demir, A., Ozturk, H., Edip, K., Stojmanovska, M., Bogdanovic, A., 2018. EFFECT OF VISCOSITY PARAMETER ON THE NUMERICAL SIMULATION OF REINFORCED CONCRETE DEEP BEAM BEHAVIOR 8, 7.

Ghobarah, A., 2001. Performance-based design in earthquake engineering: state of development. *Engineering Structures* 23, 878–884. [https://doi.org/10.1016/S0141-0296\(01\)00036-0](https://doi.org/10.1016/S0141-0296(01)00036-0)

- Goodnight, J., Kowalsky, Mervyn J., Nau, James M., 2012. Goodnight et al. 2009 - The Effect of Load History on Reinforced Concrete Bridge Column Behavior.pdf.
- He, R., Sneed, L.H., Belarbi, A., 2013. Rapid Repair of Severely Damaged RC Columns with Different Damage Conditions: An Experimental Study. *Int J Concr Struct Mater* 7, 35–50. <https://doi.org/10.1007/s40069-013-0030-7>
- He, R., Yang, Y., Sneed, L.H., 2015. Seismic Repair of Reinforced Concrete Bridge Columns: Review of Research Findings. *J. Bridge Eng.* 20, 04015015. [https://doi.org/10.1061/\(ASCE\)BE.1943-5592.0000760](https://doi.org/10.1061/(ASCE)BE.1943-5592.0000760)
- Hitaka, T., Suita, K., Kato, M., 2003. CFT COLUMN BASE DESIGN AND PRACTICE IN JAPAN 11.
- Hsu, H.-L., Lin, H.-W., 2006. Improving seismic performance of concrete-filled tube to base connections. *Journal of Constructional Steel Research* 62, 1333–1340. <https://doi.org/10.1016/j.jcsr.2006.02.002>
- Hsu, T.T.C., Mo, Y.L., 2010. UNIFIED THEORY OF CONCRETE STRUCTURES. John Wiley and Sons, Ltd.
- Jothimani, B., Umarani, C., 2019. EXPERIMENTAL INVESTIGATION ON CONCRETE FILLED STEEL TUBULAR COLUMN TO FOUNDATION CONNECTIONS SUBJECTED TO COMBINED AXIAL AND LATERAL CYCLIC LOADING. *Lat. Am. j. solids struct.* 16, e202. <https://doi.org/10.1590/1679-78255629>
- Kadoya, H., Kawaguchi, J., Morino, S., 2004. Experimental Study on Strength and Stiffness of Bare Type CFT Column Base with Central Reinforcing Bars, in: *Composite Construction in Steel and Concrete V*. Presented at the Fifth International Conference on Composite Construction in Steel and Concrete, American Society of Civil Engineers, Kruger National Park, Berg-en-Dal, Mpumalanga, South Africa, pp. 127–136. [https://doi.org/10.1061/40826\(186\)13](https://doi.org/10.1061/40826(186)13)
- Kappes, L., Berry, M., Murray, F., Stephens, J., Barnes, K., 2016. Seismic Performance of Concrete-Filled Steel Tube to Concrete Pile-Cap Connections. *J. Bridge Eng.* 21, 04016042. [https://doi.org/10.1061/\(ASCE\)BE.1943-5592.0000901](https://doi.org/10.1061/(ASCE)BE.1943-5592.0000901)
- Krawinkler, H., 1992. Guidelines for cyclic seismic testing of components of steel structures.
- Krish, Z.F., Kowalsky, M.J., Seracino, R., Nau, J.M., 2018a. Repair of Reinforced Concrete Bridge Columns via Plastic Hinge Relocation. Volume 1: Repair using Conventional Materials (Final Report No. 4000(142)). State of Alaska, Alaska Dept. of Transportation and Public Facilities Research and Technology Transfer.

- Krish, Z.F., Kowalsky, M.J., Seracino, R., Nau, J.M., 2018b. Repair of Reinforced Concrete Bridge Columns via Plastic Hinge Relocation. Volume 3: Design Guide (Final Report No. 4000(142)). State of Alaska, Alaska Dept. of Transportation and Public Facilities Research and Technology Transfer.
- Lehman, D.E., Gookin, S.E., Nacamuli, A.M., Moehle, J.P., 2001. Repair of Earthquake-Damaged Bridge Columns. *ACI Structural Journal* 10.
- Lehman, D.E., Roeder, C.W., 2012. Foundation connections for circular concrete-filled tubes. *Journal of Constructional Steel Research* 78, 212–225. <https://doi.org/10.1016/j.jcsr.2012.07.001>
- Marriott, D., Pampanin, S., Palermo, A., 2011. Biaxial testing of unbonded post-tensioned rocking bridge piers with external replacable dissipaters. *Earthquake Engng. Struct. Dyn.* 40, 1723–1741. <https://doi.org/10.1002/eqe.1112>
- Marson, J., Bruneau, M., 2004. Cyclic Testing of Concrete-Filled Circular Steel Bridge Piers having Encased Fixed-Based Detail. *Journal of Bridge Engineering*.
- Roeder, C.W., Lehman, D.E., Stephens, M., 2014. Concrete-Filled Steel Tubes for Accelerated Bridge Construction. *Transportation Research Record* 2406, 49–58. <https://doi.org/10.3141/2406-06>
- Rutledge, S.T., Kowalsky, M.J., Seracino, R., Nau, J.M., 2014. Repair of Reinforced Concrete Bridge Columns Containing Buckled and Fractured Reinforcement by Plastic Hinge Relocation. *J. Bridge Eng.* 19, A4013001. [https://doi.org/10.1061/\(ASCE\)BE.1943-5592.0000492](https://doi.org/10.1061/(ASCE)BE.1943-5592.0000492)
- Shoeibi, S., Kafi, M.A., Gholhaki, M., 2017. New performance-based seismic design method for structures with structural fuse system. *Engineering Structures* 132, 745–760. <https://doi.org/10.1016/j.engstruct.2016.12.002>
- Staton, J., Eberhard, M., Sanders, D., Thonstad, T., Schaefer, J., Kennedy, B., Olafur Haraldsson, Mantawy, I., 2014. A PRE-TENSIONED, ROCKING BRIDGE BENT FOR ABC IN SEISMIC REGIONS. <https://doi.org/10.4231/d36688k3g>
- Stephens, M.T., 2016. Design Expressions and Dynamic Evaluation of CFST Bridges Subjected to Seismic Hazards.
- Stephens, M.T., Berg, L.M., Lehman, D.E., Roeder, C.W., 2016a. Seismic CFST Column-to-Precast Cap Beam Connections for Accelerated Bridge Construction. *J. Struct. Eng.* 142, 04016049. [https://doi.org/10.1061/\(ASCE\)ST.1943-541X.0001505](https://doi.org/10.1061/(ASCE)ST.1943-541X.0001505)
- Stephens, M.T., Lehman, D.E., Roeder, C.W., 2016b. Design of CFST column-to-foundation/cap beam connections for moderate and high seismic regions. *Engineering Structures* 122, 323–337. <https://doi.org/10.1016/j.engstruct.2016.05.023>

- Tao, Z., Han, L.-H., Wang, L.-L., 2007. Compressive and flexural behaviour of CFRP-repaired concrete-filled steel tubes after exposure to fire. *Journal of Constructional Steel Research* 63, 1116–1126. <https://doi.org/10.1016/j.jcsr.2006.09.007>
- Tao, Z., Han, L.-H., Zhuang, J.-P., 2008. Cyclic performance of fire-damaged concrete-filled steel tubular beam–columns repaired with CFRP wraps. *Journal of Constructional Steel Research* 64, 37–50. <https://doi.org/10.1016/j.jcsr.2007.02.004>
- Truong, G.T., Kim, J.-C., Choi, K.-K., 2017. Seismic performance of reinforced concrete columns retrofitted by various methods. *Engineering Structures* 134, 217–235. <https://doi.org/10.1016/j.engstruct.2016.12.046>
- Varela, S., ‘Saiid’ Saiidi, M., 2016. A bridge column with superelastic NiTi SMA and replaceable rubber hinge for earthquake damage mitigation. *Smart Mater. Struct.* 25, 075012. <https://doi.org/10.1088/0964-1726/25/7/075012>
- V.Chaudhari, S., A. Chakrabarti, M., 2012. Modeling of Concrete for Nonlinear Analysis using Finite Element Code ABAQUS. *IJCA* 44, 14–18. <https://doi.org/10.5120/6274-8437>
- White, S., 2014. *Controlled Damage Rocking Systems for Accelerated Bridge Construction*.
- White, S., Palermo, A., 2016. Quasi-Static Testing of Posttensioned Nonemulative Column-Footing Connections for Bridge Piers. *J. Bridge Eng.* 21, 04016025. [https://doi.org/10.1061/\(ASCE\)BE.1943-5592.0000872](https://doi.org/10.1061/(ASCE)BE.1943-5592.0000872)
- Wu, R.-Y., Pantelides, C.P., 2017. Rapid repair and replacement of earthquake-damaged concrete columns using plastic hinge relocation. *Composite Structures* 180, 467–483. <https://doi.org/10.1016/j.compstruct.2017.08.051>
- Zhu, H., Stephens, M.T., Roeder, C.W., Lehman, D.E., 2017. Inelastic response prediction of CFST columns and connections subjected to lateral loading. *Journal of Constructional Steel Research* 132, 130–140. <https://doi.org/10.1016/j.jcsr.2017.01.016>